5 Experiments in Hypersonic Flows

The stagnation point heat flux measurements at M=12 carried out in the AT-303 facility of ITAM presented in the first section of this chapter extend the operational envelope of the ALTP for quantitative heat-flux measurements to heat loads up to ~ 200 W/cm^2.
All following sections are dedicated to hypersonic transition experiments on a 7-degree, half-angle circular cone and on a flat plate at zero angle of attack. The experimental stability investigations profit strongly from the high temporal resolutions of the ALTP and fluctuations of wall heat flux are registered in frequency unavailable up to now. The transition scenarios on the circular cone is investigated in two different hypersonic facilities at Mach number M=6. BL transition scenarios under noisy flow are compared in the Hypersonic Ludwieg Tube Braunschweig (HLB) and Mach-6-Quiet Tube (M6QT) of Purdue University. Furthermore, the influence of acoustic noise on the transition process is investigated under quiet flow conditions in the M6QT. Stagnation conditions with higher enthalpy were realized at M=12 in the AT-303 providing evidence for the detection of a third-mode instability. Finally, transition on a flat plate is studied and the growth of laser-induced flow perturbations in its boundary layer could be documented.

5.1 Stagnation-Point Heat-Flux Measurements at M=12

Quantitative heat transfer rates in the stagnation point of blunt body probes covering magnitudes of convective heat loads up to ~ 1 W/cm^2 are already presented in section 4.1. Now, the operational regime of the ALTP shall be extended into the regime of high heat loads of ~ 200 W/cm^2 for hypersonic flow conditions. Simultaneous heat-flux measurements with other well established gauges of different working principle like thin films, coaxial and calorimetric thermocouples are presented for comparison. The special probe body design and theoretical relations for such stagnation-point measurements is already discussed in section 4.1. More detailed information can also be found in [121].

5.1.1 Experimental Setup

AT-303 of ITAM. The stagnation-point measurements are carried out in the hypersonic wind tunnel AT-303 at ITAM. The facility is based on an adiabatic cycle of test-gas compression with the help of pressure multipliers. It provides very high values of Reynolds numbers in the Mach number range M= 8 - 20 due to the high pressure of the test gas in the settling chamber. The long achievable running time of 40 - 500 ms is sufficient for obtaining a steady flow in the test chamber with maximum stagnation conditions of approximately $p_{0,max} = 3000\,\text{bar}$ and $T_{0,max} = 2500\,\text{K}$. A special asset of this tunnel is the high purity of the working gas in comparison with other facilities like shock tunnel and shock tubes with diaphragms. This feature allows the simulation of high stagnation point enthalpies without the contamination of the flow by large particles. A more detailed description and discussion of the flow condition of the AT-303 is given by Kharitonov et al. [67].

Instrumentation. Figure 5.1 shows an assembly of stagnation point probes in the test section of the AT-303. The large nozzle diameter of 400 mm allows the installation of two large stagnation-point probes of 40 mm and up to 6 small probes of 20 mm in diameter. For comparison of the stagnation-point heat loads, all probe bodies were equipped with different temperature or heat-flux gauges in their front surfaces. Table 5.1 shows the gauge configuration of the probes for the two measurement campaigns. The linearity of the sensitivity of each single ALTP for an intensity range up to 200 W/cm^2 was verified by static calibration using a pulsed high power CO_2 laser (see section 2.7). The ALTP heat flux is compared with simultaneously derived heat-flux rates found by the commercial thin

Probe	Diameter[mm]	Gauge Campaign I	Gauge Campaign II
1	40	ALTP (890)	ALTP (890)
2	40	TC (18-06)	TC (18-06)
3	20	ALTP (731 I)	ALTS (731 I)
4	20	TC (18-18)	TC(18-18)
5	20	CG	CG
6	20	TF (P-682)	TF (P-682)
7	20	ALTP (786 II)	ALTS (893)
8	20	TC (22-06)	TC (22-06)

Table 5.1: Probe body configuration in AT-303 for the Measurement Campaigns I and II.

Figure 5.1: Schlieren picture at M = 12.

film (TF) gauge and coaxial thermocouples (TC) described in detail in the Appendix A.1 and by SWL [102] as well as a calorimetric probe (CG) developed at ITAM [67]. For the second measurement campaign, the ALTP in probe 7 had to be replaced due to corrosion inside the probe body. The interference of the neighboring flow field around the probes was avoided by their sufficient axial distance. Schlieren pictures e.g. Fig. 5.1 visualize the flow field in the relevant probe head area and the formation of bow shocks. Please note that the bow shocks of the large bodies only apparently intersect with the flow field of the small bodies due to the 2D projection of the image. In general, the Schlieren pictures demonstrate the blockage- and interference-free flow condition inside the test chamber during the runs.

Experimental conditions. All experiments are carried out at a nominal free stream Mach number M = 12. During the first measurement campaign, maximum stagnation condition of T_0=1000 K and p_0=1000 bar are achieved (Fig. 5.2). In campaign II the conditions are extended to a maximum range up to T_0=1550 K and p_0=1400 bar. The unit Reynolds number regime covered an interval between $20 \times 10^6/\mathrm{m} \leq \mathrm{Re}_{unit} \leq 55 \times 10^6/\mathrm{m}$ in the first and second measurement campaign.

Estimations of the expected stagnation point heat-flux densities are carried out by means of the theoretical relations described in section 4.1. Figure 5.2 displays the resulting heat-flux densities of the small and the large probe body in dependence of the stagnation temperature T_0 and pressure p_0 as parabolic curve groups q=f(p_0 , T_0=const.) Besides the

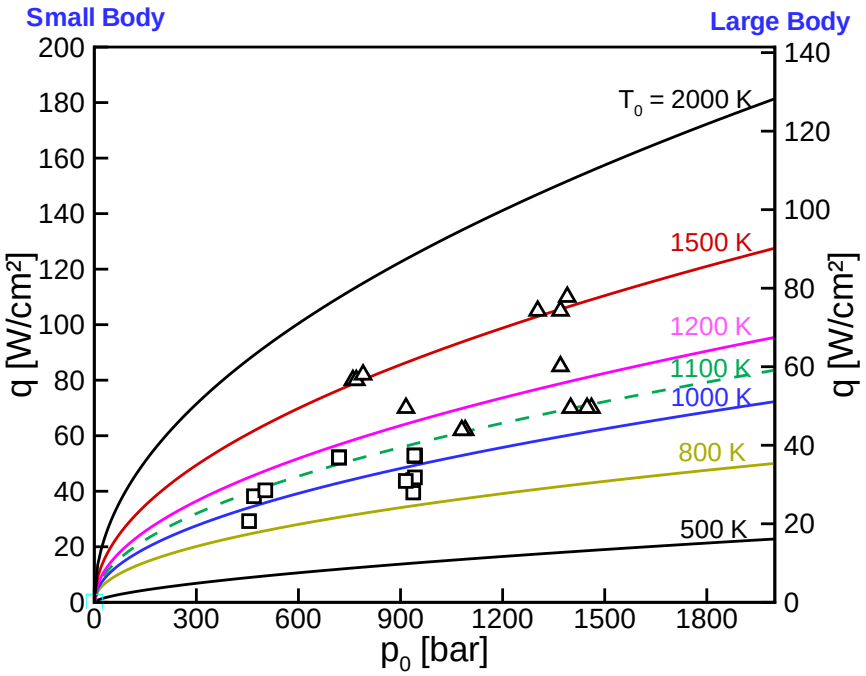

Figure 5.2: Overview of test conditions at AT-303 in reference to theoretical estimations (lines) of heat flux densities for the Measurement Campaign I (squares) and Campaign II (triangles).

experimental simulation of high heat loads, one goal is the experimental verification of the heat-flux measurements for a wide range of free stream conditions, i.e. large stagnation pressure and temperature ranges. Figure 5.2 shows the achieved experimental conditions along lines of constant stagnation temperatures $T_0 = \text{const.}$ and pressures $p_0 = \text{const.}$ In addition, free-stream conditions of constant stagnation point heat flux densities for low stagnation temperature and high pressures and vice versa could be realized. The diagram displays the wide tested operational envelope of the ALTP.

5.1.2 Experimental Results

Figure 5.3 shows a typical time history of measurement campaign I (Run 1714, T_0=1000 K, p_0=503 bar) for two ALTPs, a thermocouple and a thin-film gauge. The peak heat flux occurs within the first few milliseconds in the very beginning of the measuring time i.e. flow establishing phase. It corresponds to the passing of the shock wave initiating the nozzle flow, which leads to the formation of a boundary layer around the probe head. After the shock wave passing, the stagnation-point heat flux remains approximately constant during the whole measurement time of $\sim$80 ms. The ALTP signals resolve the establishing period of the flow better than all other gauges. The integration of the TF temperature signal by means of the Cook-Felderman algorithm [20] leads to a fairly noisy heat-flux

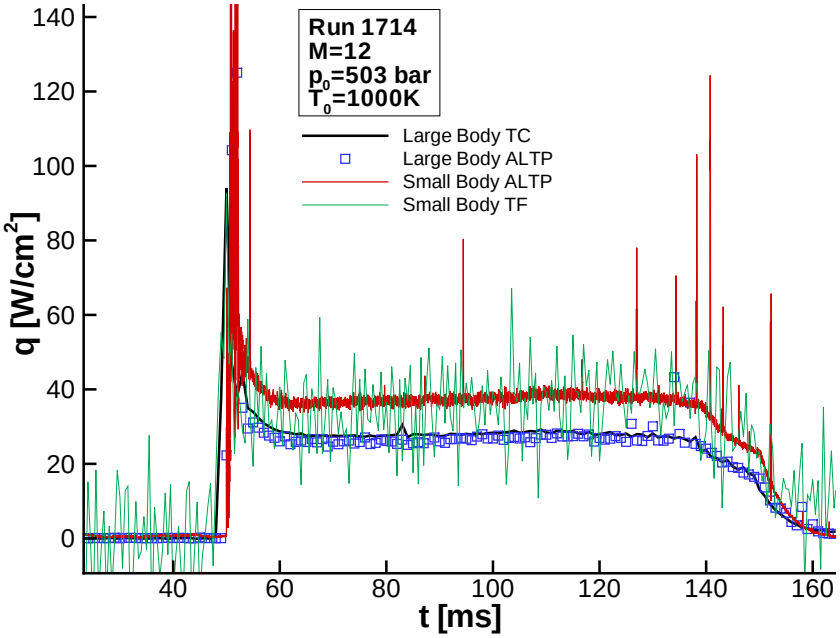

Figure 5.3: Time History of Run 1714, Comparison of time signals of ALTP, a thermocouples (TC) and a thin-film gauge (TF) (p_0=503 bar; T_0=1000 K).

signal. Nevertheless, the qualitative signal and its average are in good agreement to the ALTP time history. The third measurement technique used for comparison is a coaxial TC, which shows an excellent agreement in its heat-flux rate to the ALTP installed in the large probe body. Another independent confirmation of the stagnation-point heat-flux accuracy can be obtained from the simple geometric relationships between the diameter of the small and the large body (D_{Large} / D_{Small}=2). According relation 4.3, the expected heat-flux density of the large body should be $1/\sqrt{2}$ smaller in comparison with that of the smaller one. The specific run exhibits a heat-flux density ratio of $(q_{Small} / q_{Large}) = 1.39$. This value is only 1 % below the expected theoretical value. The ALTP signals of all three probes show irregular disturbances during the runs. The noise is very likely originated by electric interferences or by the impact of very small particles in the flow.

The time histories of all runs show similar characteristics with a nearly constant heat flux during a measuring time of approximately 60 - 80 ms. Figure 5.4(a) gives an overview of the measured mean stagnation-point heat-flux densities of all runs during the first measurement campaign. It displays the scattering of the averaged heat-flux densities measured by the three ALTP gauges. The results of the large sensor are converted by the factor to small probe conditions (equation 4.3). Furthermore, the mean heat flux densities measured by the TFs, TCs and CG are plotted in comparison to the theoretical estimations. The summary in Figure 5.4 shows that the heat flux densities measured by the CG is systematically higher than the ALTP values. On the other hand, the values measured

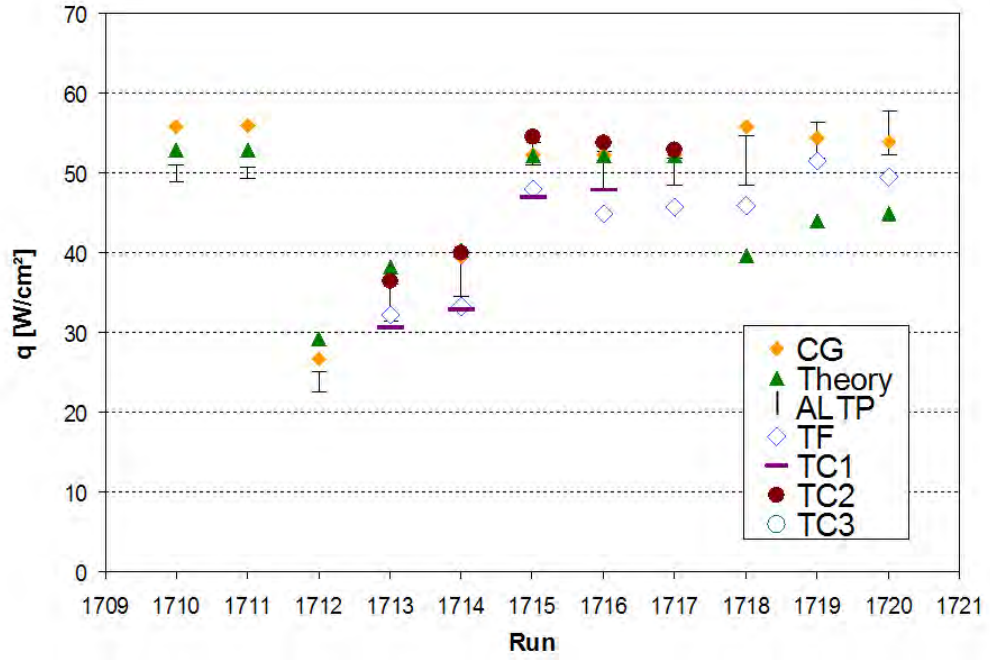

(a)

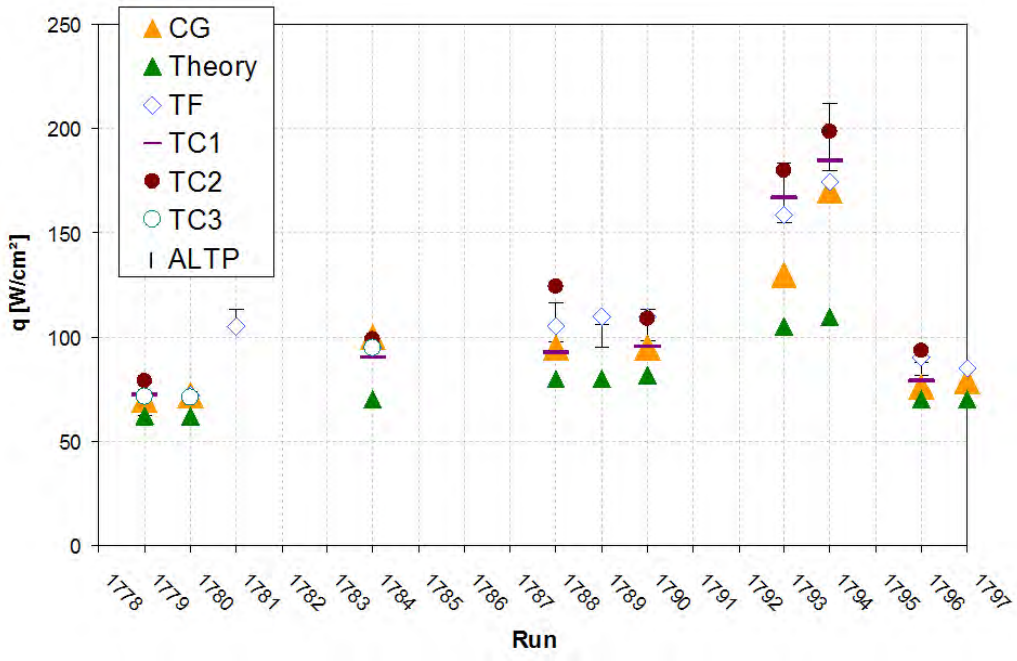

(b)

Figure 5.4: Overview and comparison of stagnation-point heat-flux densities of measurement (a) campaign I, (b) campaign II.

by the TF gauge are systematically below the averaged ALTP heat-flux densities. The data of the TCs act as third reference. They scatter in the range of the measured ALTP heat-flux densities. There is also a good agreement in comparison with the theoretical estimation. Only the last three runs (1718 - 1720) show a fairly large discrepancy between the measured values of all three probes and the theoretical estimations. The discrepancy can be explained by the onset of melting inside the pre-chamber, which led to an inaccurate measurement and or not well defined initial reservoir conditions. Overall the results of Campaign I show a good agreement of the measured stagnation point heat-flux densities of the four measurement techniques in comparison with theoretical estimations in a range of heat loads up to 60 W/cm^2. The discrepancy for most of the runs is between 5 - 10% which lies well in the uncertainty bounds of the individual measurement techniques.
The goal of the second measurement campaign was the extension of the stagnation point heat loads in the range of 1 to 2 MW/m^2. To achieve the necessary stagnation conditions, the setup of the pre-chamber had to be modified by means of a different insert in order to sustain the high strains and thermal loads. The overview in Figure 5.4(b) shows that this goal was achieved at maximal test condition of $T_0 = 1550\,K$ and $p_0 = 1400\,bar$. The summary displays a good agreement of the measured heat fluxes up to 100 - 120 W/cm^2. The discrepancies between the theoretically and experimentally obtained values increases however with rising stagnation-point conditions. The theoretical values are systematically lower in comparison with all experimental data. A solid explanation for the divergence of experimental and theoretical values cannot be given up to now. Two observations are made that might offer an indication for a possible source of explanation of the disagreement. The surface of the ALTP sensor shows small impacts caused by fine particles after the run (see Fig. 5.5). These fine particles are created by melting of the insert surfaces in the pre-chamber as well as abrasion effects in the throat region of the nozzle. The amount of particles in the flow clearly increases with rising stagnation conditions due to the higher loads in the chamber. This has been found in preceding wind-tunnel tests under corresponding increasing stagnation conditions. The particles possess high thermal energy and could lead to increased stagnation-point heat-flux densities throughout their impacts. On the other hand, the highly time-resolved ALTP signals indicated an increasing magnitude of heat flux fluctuation during the second measurement campaign.
Figure 5.6 (Run 1794) compares the time history of an ALTP, TC, TF and CG with the time traces of the measured total pressure inside the pre-chamber and the calculated total temperature for a fairly high stagnation-point heat-load of approximately 160 - 200 W/cm^2. The time signals of the TC, TF and CG show a fairly good agreement at the end of the measuring time (Fig. 5.6(a)). The mean value of the ALTP signal is slightly above the one of the other probes (Fig. 5.6(b)). However, all time histories show that the

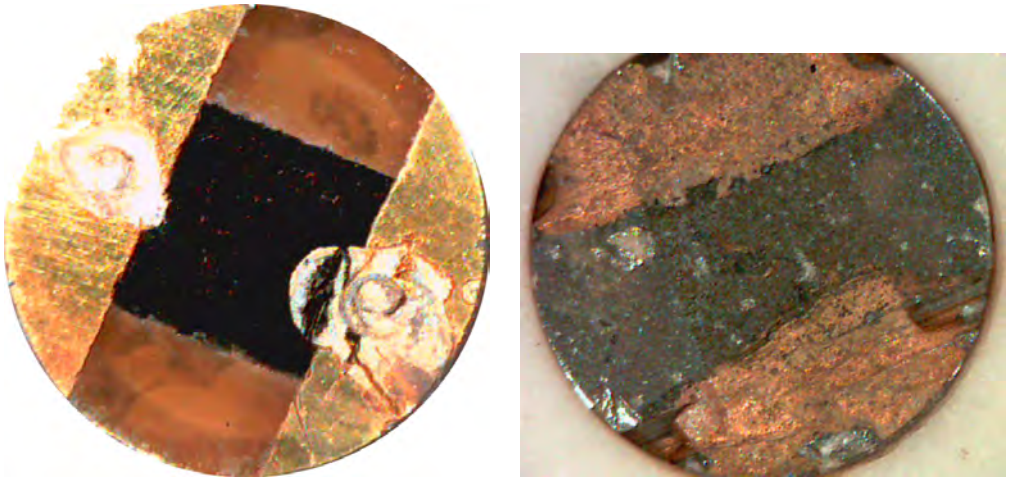

(a) (b)

Figure 5.5: (a) clean sensor surface, (b) sensor surface with particle impacts (after 35 runs).

flow uniformity inside the test section is clearly decreased in comparison to Campaign I causing a broader scattering of the mean values. At the same time the noise level drastically increased during the runs. In order to study the increased noise level systematically, the total pressure was kept on a constant level ($p_0 = 1300$ - 1400 bar) and the total temperature was increased stepwise from $T_0 = 1130$ K in Run 1797 over $T_0 = 1301$ K in Run 1798 to finally $T_0 = 1503$ K in Run 1799. Figure 5.7 clearly indicates the dependency of the noise level on the stagnation point temperature. The time history of the same

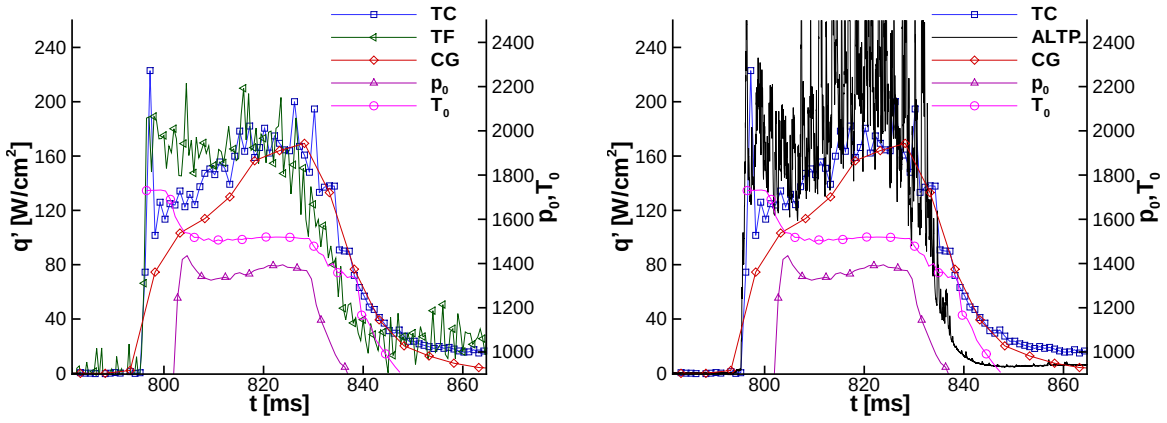

(a) (b)

Figure 5.6: Time history of run 1794 (p_0=1390 bar; T_0=1519 K); (a) gauges: thermocouple (TC), thin-film (TF), calorimetric gauge (CG); (b) gauges: thermocouple (TC), ALTP, calorimetric gauge (CG) and respective p_0 and T_0 time histories.

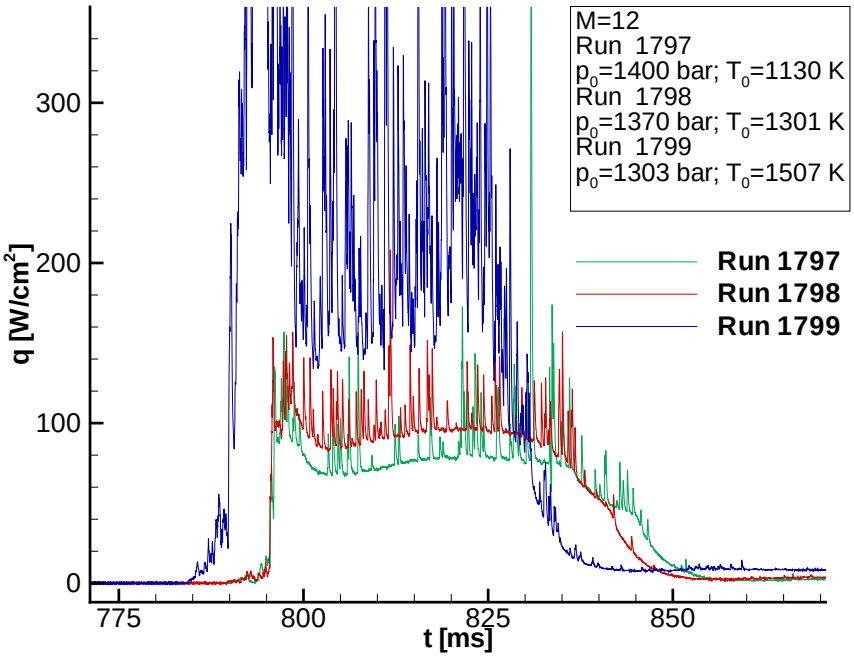

Figure 5.7: Time history of the same ALTP (k5) for the runs 1797 - 1799 = Demonstration of increasing heat-flux fluctuation amplitudes with increasing total temperature (1797: p_0=1400 bar, T_0=1130 K; 1798: p_0=1370 bar, T_0=1301 K; 1799: p_0=1303 bar, T_0=1507 K).

ALTP resolves the heat-flux fluctuations and shows their continuous rise with increasing stagnation temperature and heat flux.
These measurements allow a characterization of the flow condition in a hypersonic short-duration test facility by means of stagnation-point heat-flux fluctuations and their correlating total temperature fluctuations (see sec. 5.1.3) at high unit Reynolds numbers and stagnation enthalpies. The two observations, the impact of particles with high thermal energy and the increasing noise level with total temperature levels, might give an indication for the discrepancy between theoretical and experimental stagnation point heat loads. However, a systematic error of one single measuring principle can be excluded because all gauges work on different measuring principles. The scattering of their mean values can be explained by non-uniformities of the flow. Such non-uniformities are captured in more detail by the ALTP due to its smaller time constant. Altogether, the ability of the ALTP for measurements of high heat loads up to 2 MW/m^2 in short duration facilities could be demonstrated. Higher stagnation enthalpies have not been simulated because of the increasing pollution level of the test section flow by destructive melting particles originating from the reservoir chamber. Thus, the upper limit of the ALTP test series was reached due to an uncontrolled mechanical destruction of the sensor but not due to

a thermal load that would lead to an overheating of the sensor. One can assume that the ALTP is capable to endure even higher heat loads in a clean flow during such short duration measurements.

5.1.3 Total-Temperature Determination

Free-stream conditions in super- and hypersonic short duration facilities are usually determined by computing the wind tunnel nozzle flow. However, uncertainties in the initial reservoir conditions often lead to unreliable results. Therefore, a method proposed by Olivier et al. [101] is adopted for the stagnation-point heat-flux measurements with the ALTP. By use of the procedure described in the following, time-resolved total temperature information in a test section flow can be determined with high accuracy.
This method yields the desired free-stream conditions (dynamic pressure, mass flux density and the total enthalpy) by the measurement of the pitot pressure and the stagnation-point heat flux of a blunt body within the test section flow. The procedure is based on the correlation derived by Fay and Riddell [33] for the heat-transfer rate in the stagnation point already given by equation 4.3. Appropriate replacement of all temperature dependent quantities in equation 4.3 yields

$$q_w = 0.763\sqrt{K(T_e)}\left[Pr\left(\frac{T_e+T_w}{2}\right)\right]^{-0.6}\left[\frac{p_{02}}{RT_e}\mu(T_e)\right]^{0.4}\left[\frac{p_{02}}{RT_w}\mu(T_w)\right]^{0.1}\int_{T_w}^{T_e} c_p(T)\,dT \tag{5.1}$$

where p_{02} represents the pitot pressure and the body shape specific parameter B=0.763 for the blunt bodies currently used (Fig. 4.1(a)). A detailed derivation of Equation 5.1 can be found in [63]. Assuming isentropic flow and negleting real gas effects in a first step, the stagnation-point temperature represents the total temperature $T_0 = T_e$. Hence, the total temperature can be determined by iteratively solving Equation 5.1 for given q_w, T_w and p_{02}.
The heat flux in the stagnation point q_w is measured by a blunt body equipped with an ALTP and the pitot pressure p_{02} by a pitot probe placed in the vicinity of the blunt body in the test section. The wall temperature of the sensor rises from the initial ambient temperature in the test section to a value that is dependent on the thermal properties of the ALTP and magnitude and duration of the imposed heat load. The time-dependent surface temperature rise of the ALTP is investigated by theoretical modeling of its thermal properties in section 2.3. Hence, error estimations and corrections can be made according to these results.
For the comparison of the current results, the pitot pressure is calculated from the measured total pressure in the settling chamber of the AT-303. Therefore, the same pitot pressure is assumed for comparison of the total temperature obtained from computed

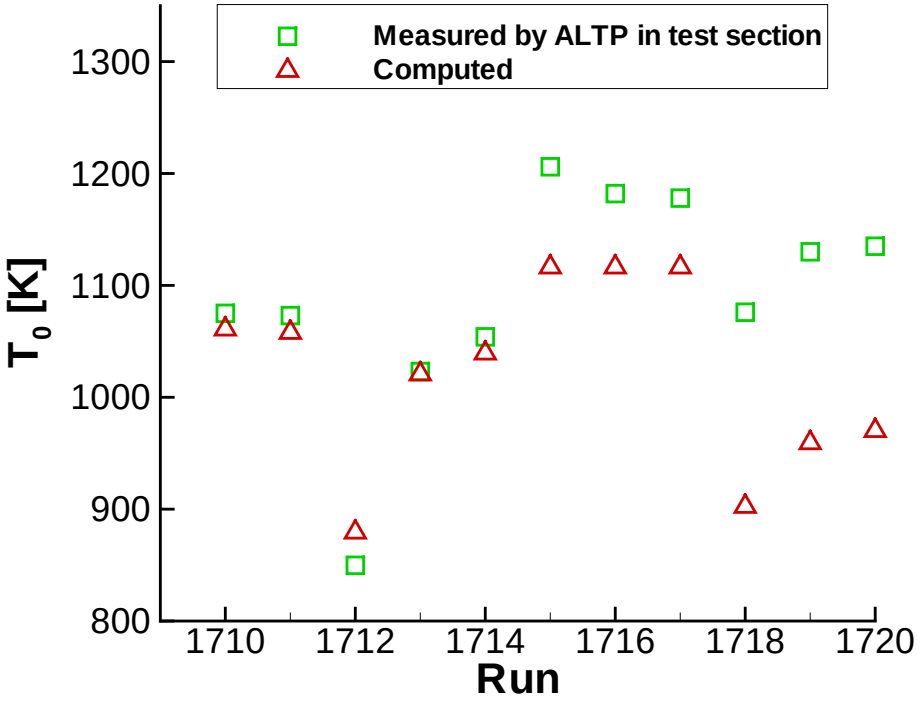

Figure 5.8: Comparison of total temperature determined by stagnation point probe and from computed data of campaign I.

values of the nozzle flow and directly measured by the blunt body probe in Figure 5.8. The results show a good agreement between the computed and directly measured values at least for the first runs. Hence, the experimental technique for the direct measurement of the total temperature by a stagnation probe is confirmed. The increasing discrepancy between the computed and measured values with rising run number might be explained by the onset of melting in the pre-chamber and a rising concentration of particles within the flow (see Fig. 5.5).

The results presented in Figure 5.8 assume constant surface temperature during the entire run. In order to estimate the error that is made by such an assumption, the surface temperature rise is estimated by use of the theoretical results shown in Figure 2.2. A heat load of $1\,\mathrm{kW/cm^2}$ is assumed in the computations, hence a value approximately 20 times larger than the heat loads of $\sim 50\ \mathrm{W/cm^2}$ experienced in campaign I. For measuring or exposure time of 0.1 s a surface temperature rise of $\sim 700\,\mathrm{K}$ can be read from Figure 2.2. Thus, a heat load of $\sim 50\ \mathrm{W/cm^2}$ results into a temperature rise of $\sim 35\,\mathrm{K}$ (linear dependency assumed) on the surface of an ALTP during a typical run of campaign I. Therefore, an error of $\sim 3\%$ is made by the assumption of constant surface temperature during a run of campaign I. Yet, it can be seen that the influence of particle concentration has a much larger effect than the assumption of constant surface temperature.

Conclusions. The stagnation-point heat-flux measurements in the hypersonic short duration test facility AT-303 demonstrate the capability of the ALTP heat-flux sensor for measuring high heat loads. The sensor could be successfully qualified and compared to established measurement techniques (thermocouples, thin-film gauges and calorimetric gauges) in a heat-flux range up to 2 MW/m^2. The experimental results show a very good quantitative agreement. The discrepancies between the theoretical calculations and experimental results need a more detailed investigation, but two possible sources of explanations could already be identified.
Furthermore, a method for the determination of the total temperature in a test section flow was adopted to the stagnation-point heat-flux measurements with the ALTP. By the application of this procedure to highly time-resolved signals of the ALTP, total temperature fluctuations can be measured in hypersonic short duration test facilities. Hence, the qualification of the flow conditions in terms of entropy spottiness at high unit Reynolds numbers and stagnation enthalpies can be accomplished.

5.2 Hypersonic Transition on a Circular Sharp Cone at M=6 : Experiments at Mach-6-Quiet-Tube

Conical boundary layers are prevalent on many hypersonic vehicles and stability measurements on sharp cones have been conducted since the 1970's. Schneider [127] gives a review of experimental and numerical studies on the subject and provides an overview of instability mechanisms on circular cones including a comprehensive list of references. The fundamental theoretical framework for investigations of compressible BL transition constitutes the linear stability theory (LST) as described by Mack [82]. It is demonstrated that hypersonic BLs contain besides vorticity disturbances (first mode), multiple acoustical instability modes (Mack modes). The first of these Mack modes, the second mode, is the most dominant and most unstable disturbance mode in flows of conical nature and in symmetric flows. The instability is influenced by several effects like bluntness, wall cooling, local curvature, surface roughness and acoustic noise. The latter effect is the subject of the current investigation. Acoustic noise is radiated from turbulent BLs on the nozzle and test section walls of hypersonic ground testing facilities. Several investigations have been carried out in quiet and noisy flow at various hypersonic Mach numbers in different wind tunnels. Most of the measurements were conducted using hot-wire anemometry. There are several drawbacks to this technique: Besides the limited frequency response and mechanical strength of hot-wires, their downstream influence excludes multiple simultaneous streamwise amplitude measurements. A non-intrusive technique for simultaneous mea-

surements of instabilities using streamwise arrays would permit determination of growth rates. Currently, the laser-differential interferometer (LDI) is the only optical technique able to measure high-frequency instability waves, and an array of LDI's would be difficult to implement [124]. Therefore, surface mounted measurement techniques with high spatial and temporal resolution are very attractive for this purpose. The ALTP represents such a technique with its unique characteristics. The excellent temporal and spatial resolution allow the capturing of fluctuations in heat flux at the wall as well as the mean heat flux at the same time. The present section focusses on the detection of instability waves, determination of their spatial growth rates and comparison of the experimental results with linear stability theory computations (see also Roediger et al. [118]).

5.2.1 Experimental Setup

Mach-6-Quiet-Flow Ludwieg Tube. The present experiments were conducted in the Mach-6 Quiet-Flow Ludwieg Tube of Purdue University. A detailed description of the facility can be found in [64], [128]. The Ludwieg Tube operates with laminar nozzle BL resulting in quiet hypersonic flow conditions up to stagnation pressures of approximately 10 bar (145 psia). Noisy flow is achieved for a pressure range up to $\sim$18.6 bar (270 psia). In order to determine the free-stream conditions, the driver tube pressure is measured at the entrance of the contraction to the test section and the temperature is determined at the end of the driver tube before every run. The temperature measurement is subject to uncertainty due to stratification and axial temperature differences in the tube. Therefore, a more accurate procedure based on the method of characteristics [31] is used to determine the temperature during the whole run. By means of this method, the uncertainty of the air temperature at the model is estimated to $\pm\,0.8\%$ and the uncertainty of the pressure is about $\pm\,0.2\,\%$. The Mach number is determined by pitot pressure measurements as $\mathrm{M}=5.8$ in noisy flow and M=6 in quiet flow conditions. The uncertainty of the test section Mach number is approximated by $\pm\,2\,\%$. This leads to an uncertainty in the calculation of the Reynolds number in the test section of approximately $\pm\,4\,\%$.
The free-stream noise level is $\sim 0.05\%$ in quiet flow when the nozzle BL remains laminar. In conventional (noisy) operation, the turbulent nozzle BL increases the noise level to $\sim 3\%$.

Cone model. A 7-deg. half-angle cone with a sharp nose tip was installed in the test section. The 500 mm long cone is made from aluminum. It allows the installation of up to 14 gauges along a generator starting at $x = 100$ mm from the nose tip with an axial spacing of 25 mm in the downstream direction (see Fig. 5.9). Contoured blind stoppers

replace unused gauge positions. For better installation, the cone consists of two pieces and an exchangeable nose tip (made of steel). The diameter of the tip was estimated to be about 6 micrometers by means of a microscope.
The rear sting mount of the cone is made from steel in order to permit firm and accurate installation of the model. Yet the angle of attack of the cone model could not be verified e.g. by optical methods due to limited accessibility. Therefore the model was rotated on its rear mount at angles of 90, 180 and 270 degrees. A slight shift in the maximum frequency of the second mode was visible for repeated runs at same nominal conditions. The results document a small angle of attack with the sensor array being slightly windward (perhaps 0.1 deg. or less).

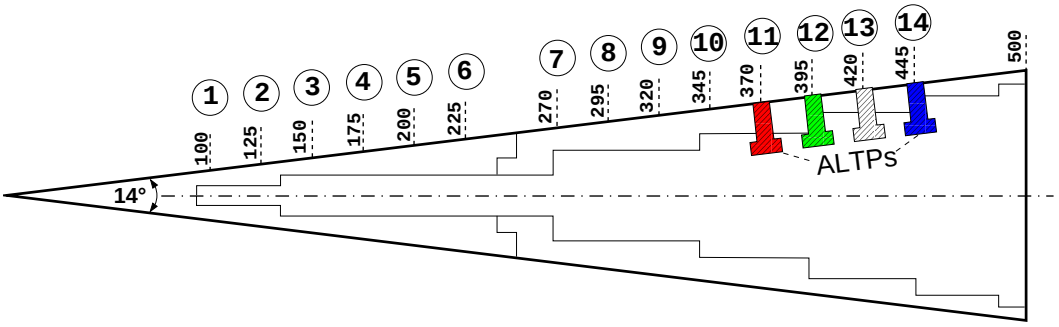

Figure 5.9: Schematic of circular cone model with installed ALTP gauges.

Position (Number)	arc length x [mm]	ALTP (Serial number)	Sensitivity s [μV/(W/cm^2)]	max. roughn. height k [mm]
11	370	941	87.4	0.174
12	395	942	126.7	0.163
13	420	944	83.5	0.154
14	445	943	77.6	0.145

Table 5.2: Specification of installed ALTPs.

Instrumentation. An array of four single-point ALTP modules is installed at positions x=370, 395, 420 and 445 mm (see table 5.2). The gauge at position x=420 mm was damaged during the experiments and is not considered in the following. The active area of the ALTP gauges used in the present experiments is $2 \times 0.4\,\mathrm{mm}^2$ limiting the spatial resolution in the streamwise direction to 0.4 mm. The gauges have a sensitivity between

83 - 127 μV/(W/cm^2) (see table 5.2). The module has a flat surface with a diameter of 8 mm. Therefore, it could not be perfectly flush mounted in the circular cone and only its streamwise diameter was aligned with the cone surface. The maximum roughness height created by the modules varies between $0.145 \leq k \leq 0.174$ mm depending on the position of the sensor (see table 5.2). The influence of the roughness created by the sensor module was found to be marginal. A detailed investigation of the influence of the roughness created by the sensor module can be found in section 5.3.
Low-noise amplifiers with nominal gain of 5000 and signal conditioning are used for the amplification of the ALTP sensor signals. The miniature amplifiers were installed inside the cone model in order to minimize electronic interference.

Data acquisition and processing. A four-channel digital oscilloscope (Tektronix DPO 7054) is used for data acquisition. The signals are captured at a sampling rate of 4 MS/s in "High-Res" mode. According to the manufacturer, the mode results in an effective resolution of 11 bits and the data are saved in a 16 bit format.
A time trace of 5 seconds is recorded for each run consisting of a 0.5 second reference trace before the start of the tunnel and 4.5 seconds of usable measuring time history. A time interval of 0.2 second length (8×10^5 samples) is extracted at the same measuring time of 2 s (1.5 s after the start of the tunnel) for the runs in noisy flow conditions. Under quiet flow, a larger time interval of 0.4 second length (1.6×10^6 samples) is used. The beginning of the extracted sample is slightly adjusted within a window 1.5 s $\pm$ 0.1 s after the start

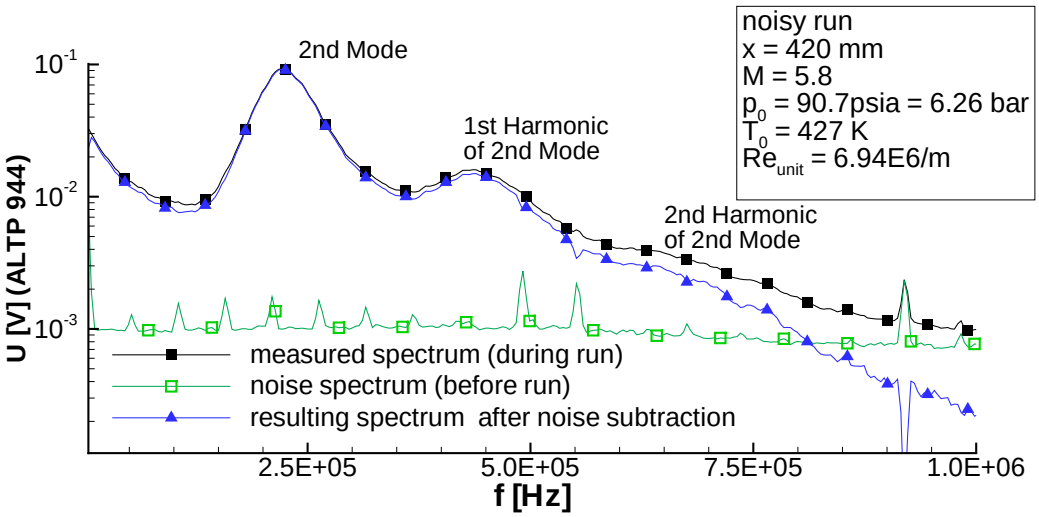

Figure 5.10: Data processing and noise subtraction for a sample ALTP spectrum showing the measured and noise spectrum and the resulting spectrum after noise subtraction.

of the tunnel in order to exclude windows of occasionally noisy flow that are believed to be due to turbulent spots passing on the nozzle wall [64]. The heat-flux values are calculated from voltage fluctuations using the specific calibration factors of the sensors. The resulting heat-flux signals are divided into overlapping windows with an constant size of 1000 samples each and an overlap of 400 samples. The windows are multiplied with a normalized Exact Blackman window and Fourier transformed. Afterwards, the amplitude spectra are averaged over all windows. In addition, the background noise spectrum is calculated from a sample of the same size taken from the data measured before the start of the tunnel. It is processed in the same way as described above and subtracted from the spectrum during the run. Hence, the uncorrelated electronic noise and disturbances are eliminated from the resulting amplitude spectra. Figure 5.10 depicts the data processing, showing the noise spectrum before the run, the measured spectrum during the run and the resulting spectrum after the power spectral subtraction of the noise. At some frequencies, the spectral subtraction of the background noise yields negative amplitude values. These values are set to zero. It remains to be verified whether such a correction is the most appropriate method.

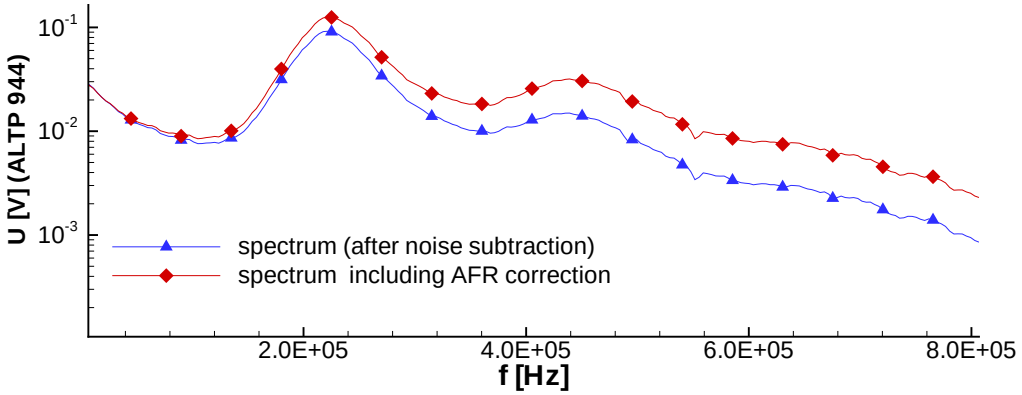

Figure 5.11: Demonstration of amplitude frequency response(AFR) correction of ALTP 941 .

Amplitude-frequency response correction. The correction of amplitude spectra by a known amplitude-frequency response (AFR) characteristic of the ALTP is demonstrated in Figure 5.11. For the correction of the spectral data, the individual AFRs of the ALTPs obtained from dynamic laser calibration (see sec. 2.8) are used. Figure 5.11 demonstrates the effect of the AFR correction on the spectrum (after noise subtraction) shown in Figure 5.10. The AFR corrected amplitude spectra allow the accurate calculation of wave amplitudes and amplification rates.

Spatial amplification rates. The definition for the spatial amplification rate along x is given by Mack [82] as

$$-\alpha_i = \left(\frac{1}{A}\right)\left(\frac{dA}{dx}\right) \tag{5.2}$$

with negative values of α_i denoting amplification. For the case of two streamwise single-point sensors at positions 1 and 2, the amplitude ratio yields

$$\frac{A_2}{A_1} = e^{-\int_1^2 \alpha_i dx} \tag{5.3}$$

with A_1 and A_2 being the wave amplitudes after noise subtraction at two consecutive sensors and (x_2 - x_1) being the surface distance between those sensors.
If α_i is constant, exponential amplitude growth can be assumed and the integral in the exponent can be simplified to

$$\frac{A_2}{A_1} = e^{-\alpha_i(x_2-x_1)} \tag{5.4}$$

Finally, the spatial amplification rate can be calculated from

$$-\alpha_i = \frac{\ln(A_2/A_1)}{x_2 - x_1} \tag{5.5}$$

Equation 5.5 is used for the calculation of the amplification rates between adjacent single-point sensors in the following experiments. It must be noted, however, that this assumption is only of limited validity because the distance between the sensors is fairly large and several times the wavelength of the investigated instability waves. Especially in regions of large changes of the amplification rate (compare stability diagrams in Figures 5.17 and 5.18), this assumption results in an averaged amplitude ratio and might deviate from predictions of linear stability theory.

5.2.2 Experimental Results

Noisy flow condition. Figure 5.12 shows the amplitude spectra at the fixed location $x = 395$ mm (ALTP 941) for a variation of unit Reynolds number. The diagram describes the shift of the transitional regime across a fixed position on the cone surface. It visualizes the successive stages of BL transition detected by fluctuation of heat-flux density at the wall under noisy flow.
Figures 5.13(a), 5.13(b) and 5.13(c) show the obtained amplitude spectra for a fixed unit Reynolds number at the three consecutive sensor positions. All diagrams clearly reveal the frequency shift of the second-mode instability to lower frequencies in downstream direction due to the increasing BL thickness along the cone. The wavelength of the second mode is proportional to the BL thickness and is roughly approximated by $\lambda \approx 2\delta$. The

first peak in the amplitude revealing the second mode is situated in a frequency range of 180 - 220 kHz. In addition, a first harmonic of the second-mode instability is captured in a frequency range between 300 - 400 kHz for certain stages of BL transition. A weak residual of a second harmonic of the second-mode instability is possibly visible in some amplitude spectra (ALTP 944 in Figure 5.11) captured by an ALTP with very good AFR characteristic.

At the lowest realized unit Reynolds number $Re_{unit} = 4.29 \times 10^6$/m (Fig. 5.13(a)), the amplitudes of the second-mode instability rise in downstream direction. The amplitude spectra seems to show that the BL is already transitional at this Reynolds number, since the amplitudes increase in a wide frequency range above and below the second mode. At a slightly higher unit Reynolds numbers (Fig. 5.13(b)), the amplitude of the second mode at the rear gauge position starts to decrease and the first higher harmonic disappears. It shows that the BL is close to the turbulent state. At the highest unit Reynolds number Re_{unit}=6.43 $\times 10^6$/m (Fig. 5.13(c)), the second mode finally disappears completely at x=445 mm and the spectrum is characteristic of a turbulent BL state.

Figure 5.14 demonstrates the calculation of the amplification rates for the case of the lowest realized unit Reynolds number Re_{unit}=4.29 $\times 10^6$/m and therefore the earliest stage of BL transition. The ratios are calculated from the amplitude spectra (note logarithmic scale) without any analytical approximation of the spectrum. The results show not only the amplification rates of the second mode but also the rates in the extended frequency range of its first harmonic. The maximum rate of the second mode is about 25/m at 125 kHz. The amplification rate of the first harmonic is even a bit higher and reaches

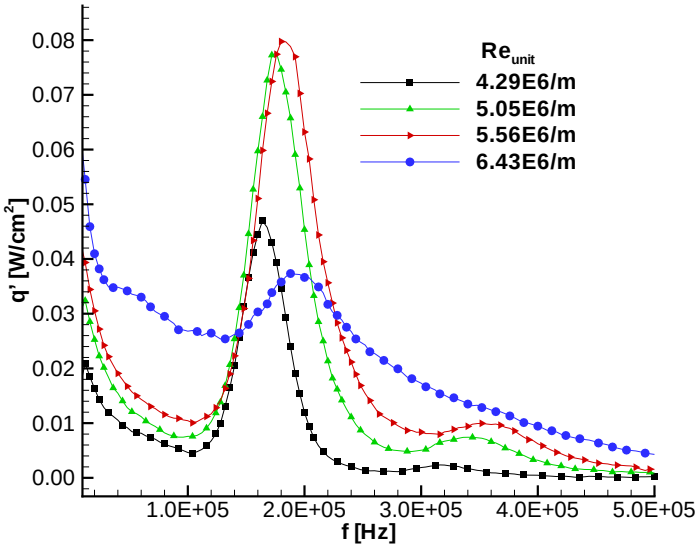

Figure 5.12: Amplitude spectra (AFR corrected) for unit Reynolds number variation at fixed sensor location x=395 mm.

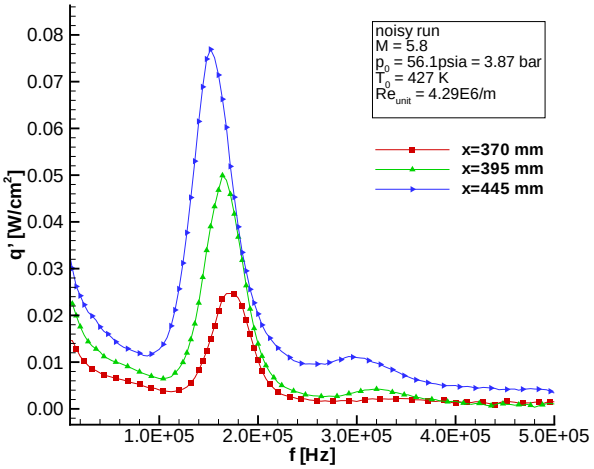

(a)

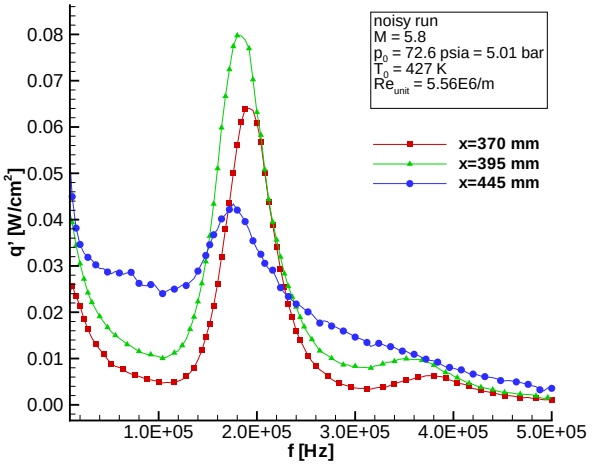

(b)

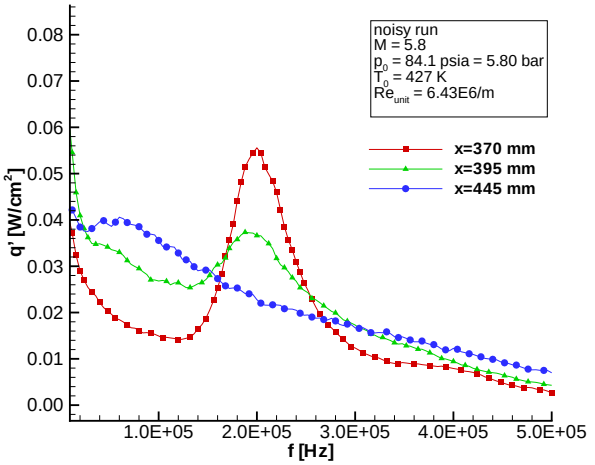

(c)

Figure 5.13: Amplitude spectra (AFR corrected) for (a) $\mathrm{Re}_{unit} = 4.29 \times 10^6/\mathrm{m}$, (b) $\mathrm{Re}_{unit} = 5.56 \times 10^6/\mathrm{m}$ and (c) $\mathrm{Re}_{unit} = 6.43 \times 10^6/\mathrm{m}$.

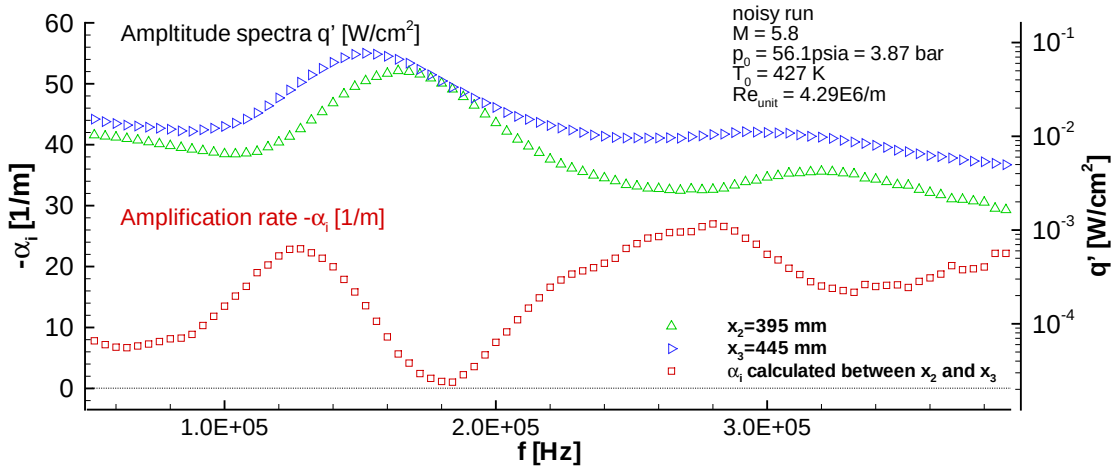

Figure 5.14: Amplification rate calculated between positions x=395 and 445 mm for noisy flow.

values of ∼27/m at 280 kHz. In addition, the spectrum in the frequency range below the second mode is slightly amplified. These observations indicate the transitional character of the BL and the non-linear effects already present in the BL.

Quiet flow condition. Figure 5.15 shows the second-mode instability detected at a driver-tube pressure of ∼8.58 bar (124.4 psia). The initial pressure of the run is close to

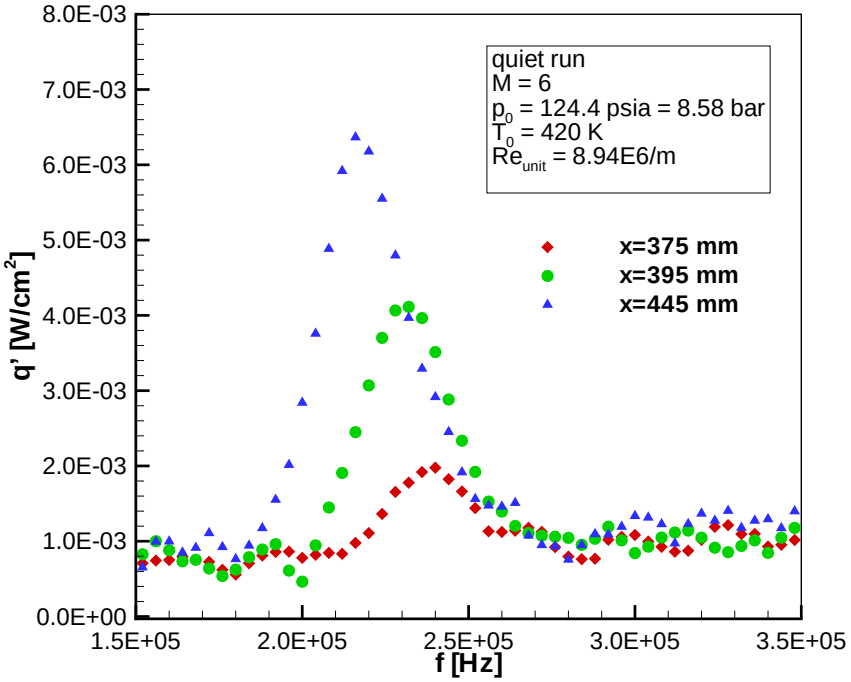

Figure 5.15: Amplitude spectra (AFR corrected) for Re_{unit}=8.94E6/m (RUN 39).

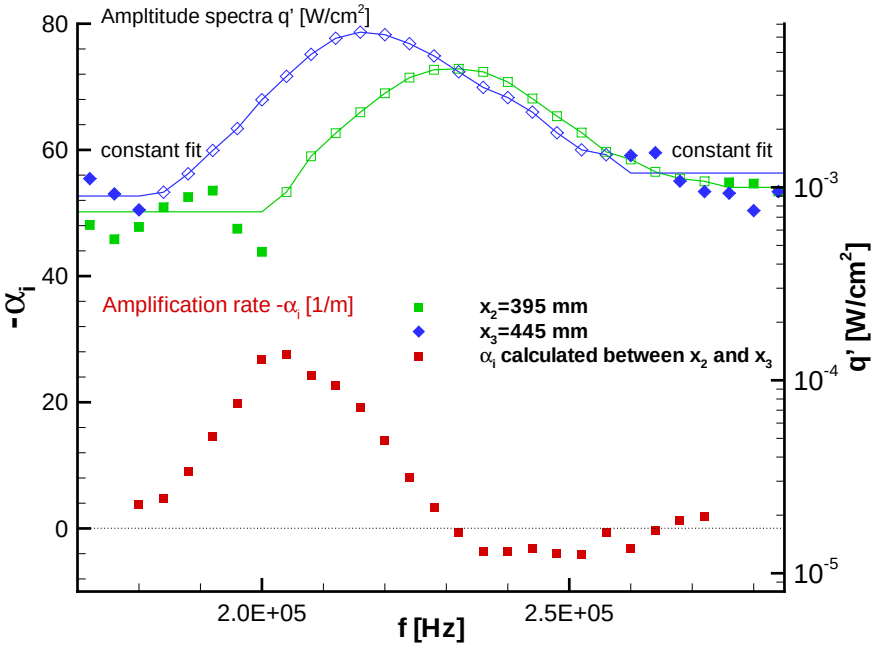

Figure 5.16: Amplification rates between positions x=395 and 445 mm for quiet flow (RUN 39).

the upper limit where quiet flow can currently be achieved in the Ludwieg tube. The second mode could not be detected at lower unit Reynolds numbers, because the fluctuations are more than an order of magnitude smaller under quiet flow, and the limited signal-to-noise ratio of the ALTP sensors cannot detect them. Since the second-mode instability could only be detected at higher stagnation pressures, it is not possible to compare the wave amplitudes at the same Reynolds number in quiet and noisy hypersonic flow at natural disturbance level. However the comparison of second-mode wave amplitudes in quiet flow conditions at Re_{unit}=8.94 $\times 10^6$/m and in noisy flow at Re_{unit}=4.29 $\times 10^6$/m shows that their amplitudes in quiet flow are ∼12 times smaller than in noisy flow conditions at the same x-location. A direct comparison of the amplitudes would only be possible by using linear stability theory to compute the amplification between the two states.

The fluctuations of heat-flux density at the wall are in the mW/cm^2 range and mark the lower limit of detectable heat-flux density by means of the ALTP. Experiments with a higher ratio of total temperature to wall temperature are clearly desirable in order to improve the signal to noise ratio.

Figure 5.16 demonstrates the calculation of growth rates from amplitude spectra at locations x=395 mm and x=445 mm (note logarithmic scale). Amplification rates are subject to high uncertainty especially on the left edge of the second-mode peaks - the region of highest amplification rates. Due to the low amplitudes of the fluctuations, the second-

mode peak of the upstream sensor (right bell) drops faster below the background noise level than the peak of the downstream sensor (left bell). Thus, the calculation of ratios in this region is very sensitive. Low signal to noise ratios or analytical fitting in this region can produce arbitrarily high maximum amplification rates. Therefore the spectrum to the left and right of the second-mode bells is approximated by a constant fit as shown in Figure 5.16. The constant value to the left of each bell corresponds to the mean value of the background noise (filled symbols) in a frequency range between 150 kHz and the beginning of the second-mode peak (hollow symbols). On the right hand side, the constant results from the mean value in the frequency range extending from the right edge of the peak up to 340 kHz. The second-mode bell itself is not approximated by any analytical function.

The maximum amplification rate of the sample run 39 is about 28/m. This value is the maximum rate observed in three repeated runs at the same nominal conditions. The other runs only reached values of 16/m and 18/m. However the background noise level of these runs was slightly higher. This indicates the uncertainty of the determined maximum amplification rates in quiet flow. The averaged amplification rates of these three repeated runs will be discussed later in Figure 5.19(b).

Comparison with linear stability theory. Linear stability theory (LST) calculations were carried out in cooperation with B.V. Smorodsky of ITAM for comparison with the experimentally obtained amplification rates at corresponding unit Reynolds numbers under quiet and noisy flow. The axisymmetric conical BL of a sharp cone at zero angle of

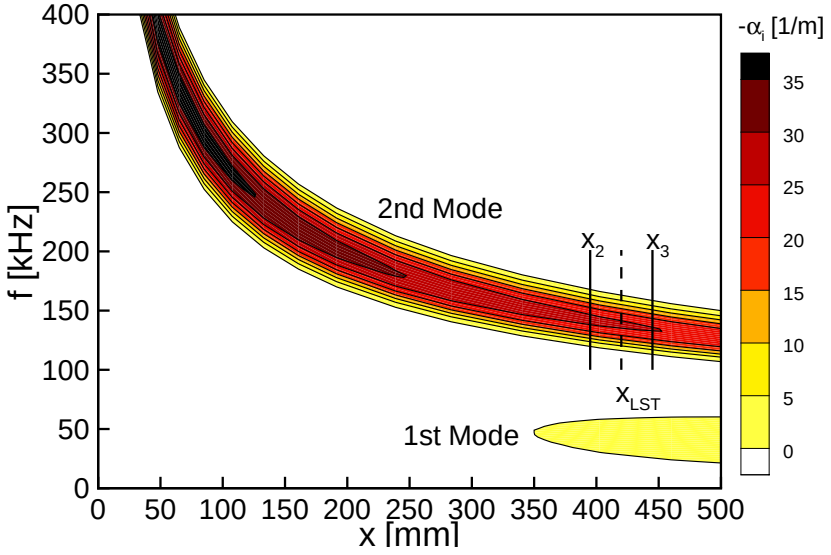

Figure 5.17: Stability diagram (2-D) for noisy run (flow conditions: M = 5.8, p_0 = 56.1 psia = 3.87 bar, T_0 = 427 K, T_w = 310 K, $Re_{unit} = 4.29 \times 10^6$/m).

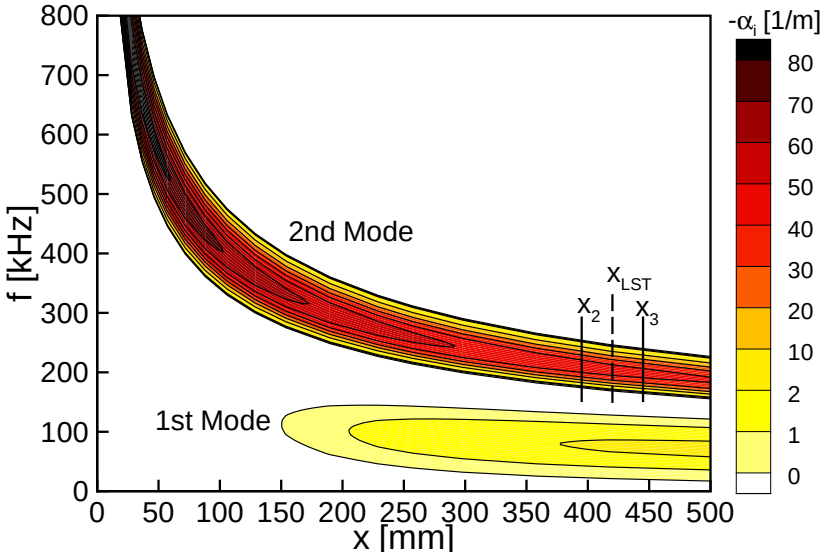

Figure 5.18: Stability diagram (2-D) for quiet run (flow condition: M = 6, p_0 = 124.4 psia = 8.58 bar, T_0 = 420 K, T_w=310K, $Re_{unit} = 8.94 \times 10^6$/m.

attack is computed by means of self-similar flat-plate compressible boundary layer equations using the Lees-Illingworth transformation [149]. Wall temperature, Prandtl number and specific heat ratio are assumed to be constant. The Sutherland law is used to express the temperature dependency of the viscosity. In addition, the flow is assumed uniform in the streamwise flow close to the cone surface downstream of the attached shock. The outer inviscid flow properties on the cone surface are determined by means of the numerical integration of Taylor-Maccoll equation [1]. Local linear stability analysis of the BL is performed in the framework of the eigenvalue problem for Lees-Lin equations [155], which have been integrated numerically by means of the method of orthonormalizations [35]. Spatial growth rates of the instability waves are determined by eigenvalues as function of the flow stagnation parameters and wave frequency.

Figure 5.17 and 5.18 show the stability diagrams of the cone BL for the noisy and quiet runs, respectively. The diagrams display the spatial amplification rate contours in the plane of dimensional frequency versus distance x from the cone tip. Shaded areas correspond to unstable domains with respect to 2-D first and second-mode instability waves (lower and upper regions respectively). It can be noted that regions of instability of first and second modes are separated from each other in both diagrams. The region of the second-mode instability is represented by a relatively narrow frequency band which trends downward quite fast with increasing x. The location of the ALTP sensors used for the calculation of the experimental rates are displayed by vertical lines. Looking at these cross sections, the sensors at the two x-locations should register peaks in the fluctuations of wall heat-flux density at different frequencies. Probes positioned further downstream will

detect a spectral peak at lower frequencies. Please note that the first mode possesses one order of magnitude lower growth rates in comparison with the second-mode instability. Theoretical estimations presented by Knauss et al. [71] show also that the fluctuations of the heat flux at the wall are about one order of magnitude smaller in the range of the first mode in comparison with the one of the second mode.
Figure 5.19(a) and 5.19(b) display the experimentally obtained and the calculated 2-D spatial amplification rates in noisy and quiet flow, respectively. The LST rates are evaluated at a location in the middle of the two probe positions (x=420 mm) as a first approach (integrated amplifications should be used for more accurate comparison). The magnitudes of the measured and predicted maximum growth rates in noisy flow are in good agreement. The slightly lower experimental values may be due to the small angle of attack as described in section 5.2.1 or might result from an increase in wall temperature during the run. A rise in wall temperature stabilizes the second-mode instability and could decrease the maximum amplification rates. The magnitude of this effect is estimated for the quiet run in Figure 5.19(b). The results show that a wall temperature rise of 33 K leads only to a decrease of maximum growth rate by $\sim 9\%$. In addition, superposition of 3-dimensional modes leads to lower amplification rates in comparison to LST while only the existence of 2-D modes is considered here. Investigations with a three dimensional sensor array on the surface of a cone seem to be necessary to confirm the absence of 3-D modes. Furthermore, lower experimental growth rates were also previously reported (see review by Stetson and Kimmel [140] and references therein). The disagreement was suspected to originate from the large non-linear nature of the waves measured under noisy flow. Yet Figure 5.14 shows that the growth rate of the first harmonic is only marginally higher than the one of its fundamental.

In quiet flow, the averaged experimentally determined maximum growth rates are significantly lower. As stated previously, scatter in the three measurements was large, and the maximum rates could not be reliably determined due to the low amplitude of the fluctuations and the high uncertainty in the determination of amplification rates on the left edge of the second-mode bells. Hence, the maximum value is situated in the frequency range that could not be properly resolved by the measurements.
Both diagrams show that the frequency of the second mode predicted by the calculations is slightly higher. The experimentally determined maximum growth rate in noisy flow is ~ 10 kHz below the calculated one, or about 8 %. This effect is very likely caused by the small angle of attack of the cone, since the wavelength of the second mode scales approximately with the boundary-layer thickness. In quiet flow, the frequency of the maximum growth rate in measurement and calculation seems to coincide well. However, the maximum is suspect to a high uncertainty as stated previously and the more credible right

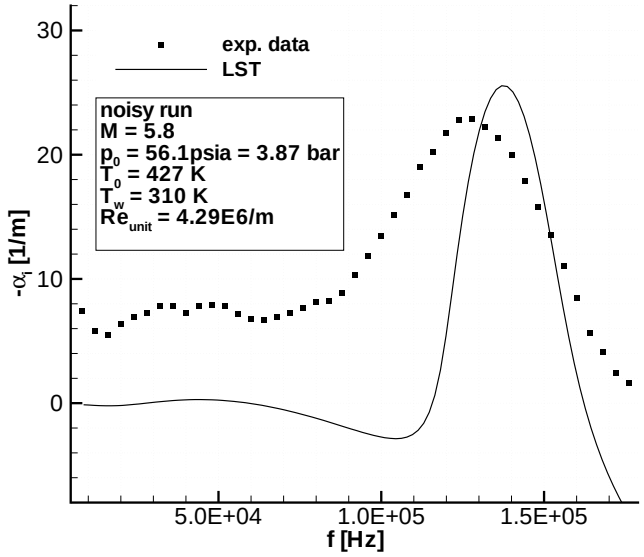

(a)

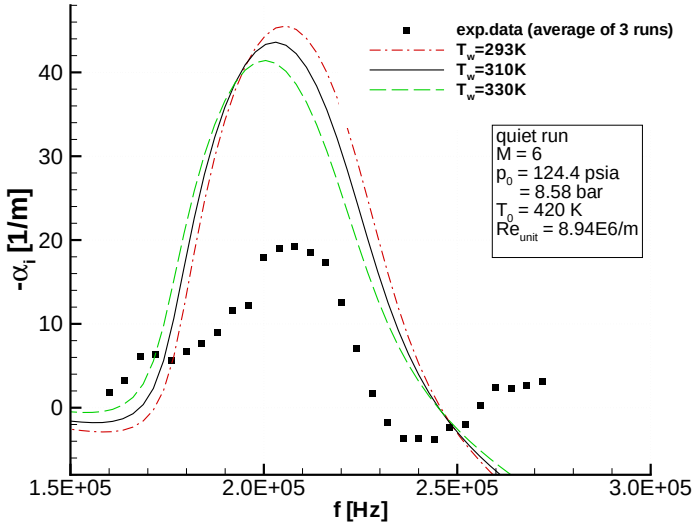

(b)

Figure 5.19: Comparison of experiments and computations under (a) noisy flow; (b) quiet flow. Lines denote results from LST; in (b) three different wall temperatures are considered.

branch of the curve shows a similar 10 kHz shift in frequency. Extrapolating by assuming a behavior similar to the theoretical growth rate would place the measured maximum at lower frequency than the theoretical curve, as in noisy flow.

The bandwidth of amplified frequencies in noisy flow varies significantly from the predicted one. The frequencies below and above the second mode are already amplified. As stated in section 5.2.2, these observations might indicate the presence of non-linear effects

and point out the transitional character of the BL.

Conclusions. Hypersonic transition is studied on a 7-deg. half-angle sharp cone under noisy and quiet flow. A streamwise array of ALTP heat-flux gauges is used to determine spatial amplification rates of instability waves. In noisy flow, the consecutive stages of boundary layer transition could be documented by quantitative amplitude spectra of heat-flux density at the wall. The amplitude-frequency response characteristics of the measurement system is taken into account in order to determine absolute values of wave amplitudes. The dominant second mode and its first harmonic show similar growth rates during the early stages of boundary layer transition. Measured maximum growth rates for the second mode are in very good agreement with those calculated using linear stability theory. The difference in the amplified range of second-mode frequencies is possibly due to a small angle of attack. The measured spectral range of amplified frequencies is more broad than the one predicted by linear stability theory, which might indicate the presence of non-linear effects.
Under quiet flow, the calculation of growth rates in the region of maximum amplification rates is subject to high uncertainty due to the low amplitude of second-mode waves. Therefore, the measured maximum growth rates do not match the computations. The bandwidth of the amplified frequencies is however in good agreement. The measured amplitude of the fluctuations in quiet flow is in the mW/cm^2 range, which clearly marks the lower limit of detectable heat flux per unit area by means of the ALTP. Experiments with a higher ratio of total temperature to wall temperature are desirable in order to improve the signal to noise ratio and to simulate more realistic flight conditions. The ALTP is of special interest for transition research in hypersonic facilities with high stagnation enthalpy where conventional measurement techniques like hot-wires cannot be used.

5.3 Hypersonic Transition on Circular Sharp Cone at M=6 : Experiments at HL Braunschweig

As shown in the previous section, the disturbance level of the hypersonic ground testing facility is of great importance for transition studies. In order to make statements about the comparability of BL transition experiments in two different hypersonic facilities, experiments with the same pointed cone model used in the M6QT are carried out in the Hypersonic Ludwieg Tube Braunschweig (HLB).
For the measurements of instability waves, the free-stream disturbance spectra of the facility are of fundamental importance. In the experiments carried out in the HLB, the

disturbance level is documented by pitot pressure fluctuations and additionally measured by means of fluctuations of heat flux in the stagnation point of a blunt body. Furthermore, investigations concerning the influence of the roughness created by the ALTP sensor module on hypersonic BL transition are made. The use of a staggered array composed of fast-response ALTPs and surface pressure gauges allow the comparison of simultaneously measured instability waves and their growth rates. All experiments were carried out in close cooperation with D. Heitmann and M. Estorfof from the Institute for Fluid Mechanics (ISM).

5.3.1 Experimental Setup

Hypersonic Ludwieg Tube Braunschweig (HLB). The HLB operates at a nominal Mach number of M = 6 in a unit Reynolds number regime of 3 - 20 $\times$ 10^6/m at conventional noise level. A schematic of the HLB is shown in Figure 5.20. It consists of a storage tube which is separated from the low pressure section by a fast-acting valve. The driver tube is heated along the first 3 m upstream of the valve. The heated section accommodates the amount of gas that is released during one run. The valve consists of a streamlined center body on the tube axis. The pneumatically driven valve opens within 20 ms and closes after the expansion wave has passed back and forth within the storage tube. The resulting test time with constant pressure and temperature is 60 - 80 ms depending on the initial storage tube pressure. The low pressure part consists of nozzle, test section, diffuser and a dump tank (6 m^3). A more detailed description of the facility can be found in [32].

The nozzle maintains an opening half angle of 3° which results into a slightly expanding

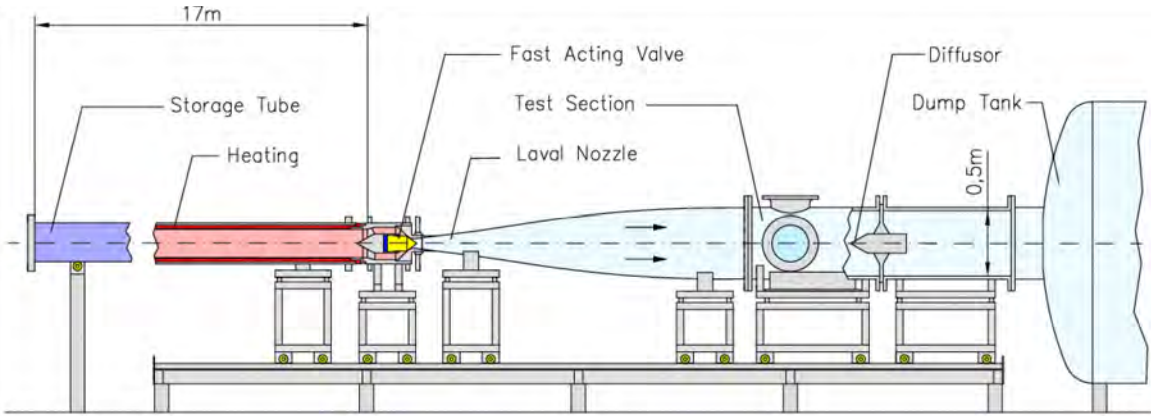

Figure 5.20: Schematic of the Hypersonic Ludwieg tube Braunschweig [32].

flow in the test section with Mach numbers between 5.8 and 5.95 depending on the axial position and on the unit Reynolds number. The driver tube pressure is recorded with

an accuracy of ±1%. The driver-tube temperature is measured during the run by two fast thermocouples. It must be noted that the measured temperature difference between the upper and lower measurement position can be as high as 30 K due to temperature stratification. The mean value, however, is not proven to be the total temperature at the height of the model in the test section. An uncertainty of ±1% is estimated in the determination of the total temperature. The overall uncertainty in the determination of the Reynolds number is ± 2% in the relevant unit Reynolds number range. The disturbance level in the facility increases towards the centerline, which is typical for axisymmetric nozzles (Heitmann et al. [52]). Therefore, the cone was positioned slightly off tunnel axis in a region with lower noise level.

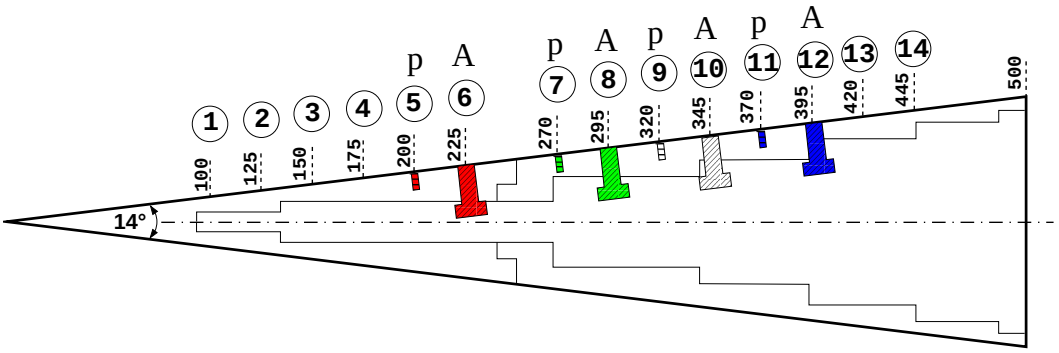

Figure 5.21: Schematic of circular cone model with installed ALTP and pressure gauges.

Position (Number)	arc length x [mm]	Sensor (Serial number)	Sensitivity s [μV/(W/cm^2)]	Sensitivity s [μV/Pa]
5	200	PCB 1 (4437)		20.3
6	225	ALTP 941	80.5	
7	270	PCB 2 (4342)		22.0
8	295	ALTP 942	110.7	
9	320	PCB 3 (4343)		24.5
10	345	ALTP 1010	148.4	
11	370	PCB 4(4436)		20.6
12	395	ALTP 943	101.5	

Table 5.3: Specification of installed ALTPs and PCB pressure gauges.

Cone-model instrumentation. The 7-deg. half-angle, sharp cone used in the experiments is already described in section 5.2.1. Special care is taken in order to align the cone model. An identical plexiglass cone model is used for the alignment of the sting mount by measuring the line of transition with an infrared camera on the surface. Proper alignment is attained iteratively in subsequent tunnel runs until the transition line is found to be straight. Afterwards, the plexiglass model is replaced by the aluminum cone model and the alignment is verified by comparison of the maximum frequency of the second mode by rotating the model on its rear mount at angles of 90 and 180 degrees. A frequency shift of less than 10 kHz is observed, which is within the repeatability of the runs at same nominal flow condition.

The cone model is instrumented with a staggered array of ALTPs and fast-response pressure sensors. Figure 5.21 shows the installation location of all sensors ("p" stands for pressure sensor, "A" represents an ALTP heat-flux gauge) and Table 5.3 lists their specific sensitivities. The active area of the ALTP gauges used in the present experiments is $2 \times 0.4\,\mathrm{mm}^2$ and low-noise amplifiers with signal conditioning are mounted inside the model for the amplification of the mean value (low-pass filtered DC-branch, nominal GAIN 8000) and the fluctuations (high-pass filtered AC-branch, GAIN 5000). The commercial pressure sensors of type M131A32 are manufactured by PCB Piezotronics. The diameter of their sensing area is 3.18 mm. Power is supplied to the pressure sensors using an instrument provided by the manufacturer (PCB 482A22), which at the same time also performs signal conditioning. According to the manufacturer's specification, the resonance frequency of the pressure sensors is larger than 1 MHz and the output signal is high-pass filtered at 10 kHz. The sensors are calibrated in a shock tube by the manufacturer and have sensitivities between 20.3 and 24.5 μV/Pa (see Table 5.3). For details on the measurement technology the reader is referred to the manufacturer's website [107].

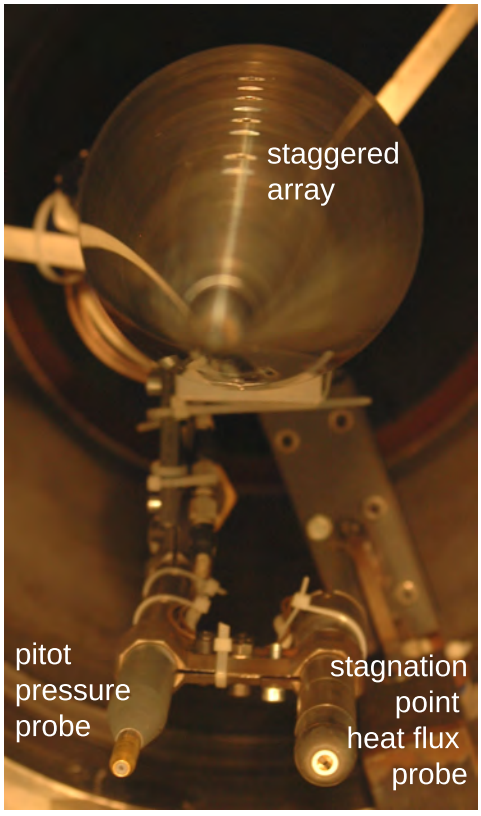

Figure 5.22: Installation of circular cone, pitot-pressure and stagnation-point heat-flux probe.

Stagnation-point probes. The disturbance level of the facility is simultaneously determined by a pitot-pressure probe and by use of a blunt body probe with an ALTP installed in the stagnation point (Fig. 5.22). The blunt body probe with a base diameter of 20 mm (see section 4.1 for more details) is installed in the middle of the test section upstream of the shock waves created by the cone model at a vertical position z=-129 mm.
The pitot probe consists of a 7.5 mm diameter reference tube with a 15° conical head and a planar surface with a diameter of 5 mm. An Entran EPIH-113-1B/Z1 pressure transducer is used in the pitot probe. It has a measuring range of 345 kPa (50 psi), a natural frequency of 400 kHz and a flush-mounted membrane (1.5 mm in diameter). The manufacturer specifies the useful range as 20 % of the resonant frequency. The pressure gauge is flush mounted in the planar front surface and ground insulated in the head of the pitot probe.

Data acquisition and processing. An 8 channel, 16 bit transient recorder PCI-express card (Spectrum M2i.4652) is used for data acquisition. The card allows a maximum sampling rate of 3 MS/s. A time period of 40 to 70 ms is evaluated depending on the available measuring time of each single run. The heat flux and pressure values are calculated from voltage fluctuations using the specific calibration factors of the sensors. The resulting signals are divided into overlapping windows with an constant size of 800 samples each and an overlap of 500 samples. Averaging, noise subtraction and AFR correction and the calculation of the spatial amplification rates is carried out as described in section 5.2.1.

5.3.2 Experimental Results

Disturbance-level measurements. The disturbance level of a hypersonic test section flow commonly refers to the so-called "acoustic mode", i.e. sound waves which are detectable as pressure fluctuations. The sound waves mainly emanate from the turbulent BL of the nozzle and test section walls. Hence, they correlate in intensity and spectral distribution with the BL characteristics [106]. Therefore, the acoustic mode is Reynolds number dependent and can cause unit Reynolds number effects in wind tunnel transition experiments. Pitot pressure fluctuations are only of limited value to quantify the acoustic disturbance level (see [70], [96], [105], [138]) and in addition the entropy and vorticity disturbance mode are also present in the test section flow. A differentiation of these disturbance modes is only possible by means of modal analysis using the hot-wire technique (see e.g. Weiss et al. [147]). Such an analysis was currently not possible in the facility and in order to obtain some information on the "entropy mode", a stagnation point probe equipped with an ALTP is used for the detection of heat-flux density fluctuations in the

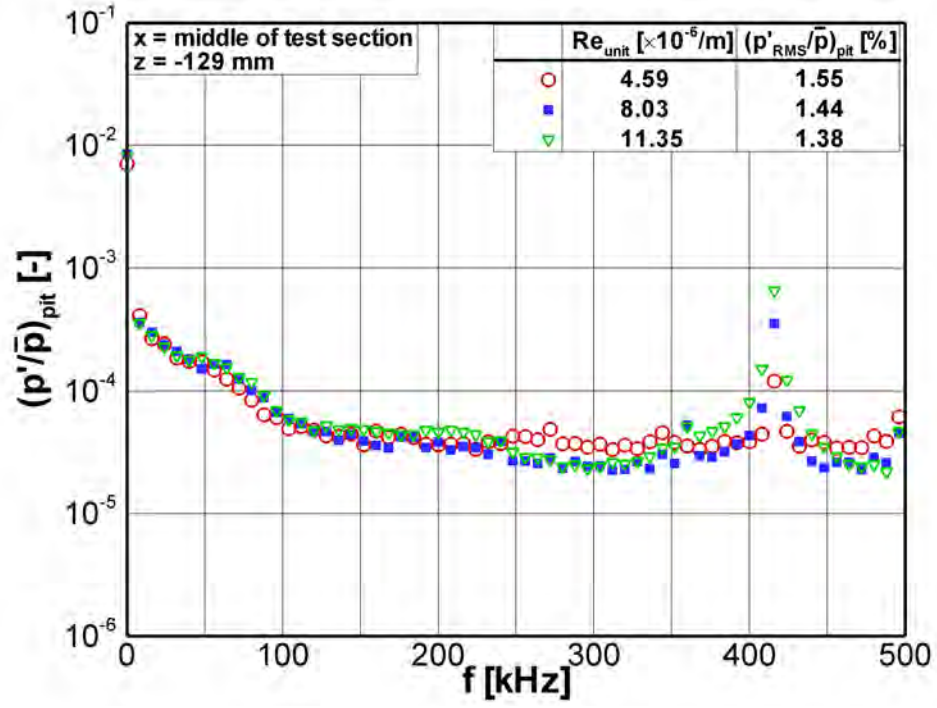

(a)

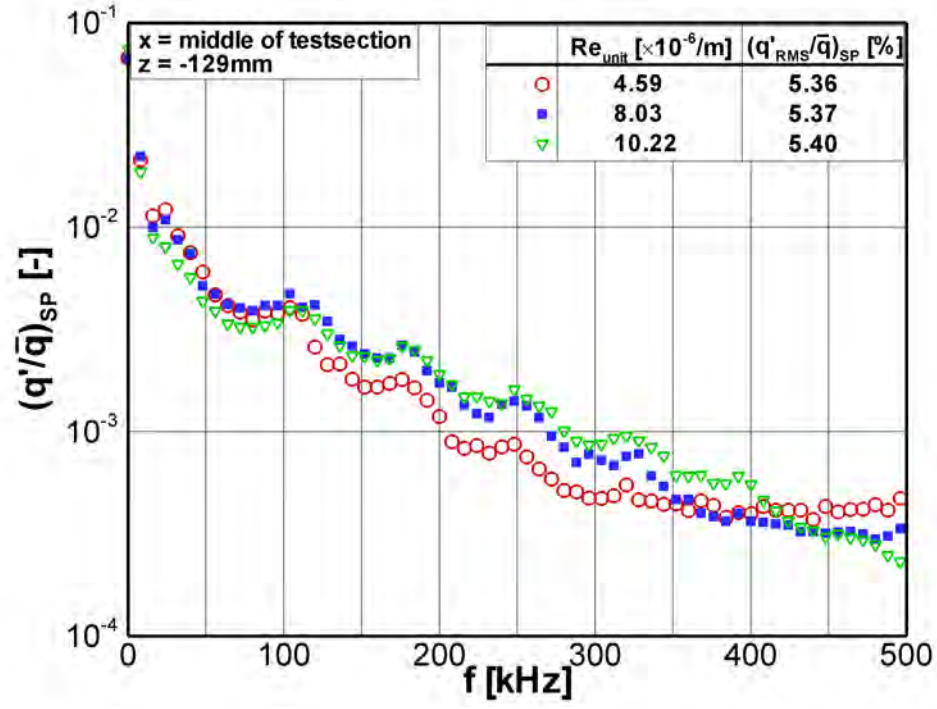

(b)

Figure 5.23: (a) pitot-pressure fluctuations, (b) fluctuations of stagnation-point heat flux for a variation of unit Reynolds number (simultaneously measured with surface fluctuations on the cone). [52]

stagnation flow which correlate with the total temperature fluctuation in the oncoming free stream. Total temperature fluctuations are only sparsely determined for the qualification of test section flows in other facilities. The fast frequency response of the ALTP sensor offers a possibility to detect temperature disturbances in a frequency range that has not been accessible up to now and under harsh conditions, where hot wires can not be used due to their limited durability .

The disturbance level is determined for the operational unit Reynolds number regime of the HLB at several locations in the test section. A detailed description of the results can be found in Heitmann et al. [52]. The RMS values of the normalized pitot pressure fluctuations defined as $(p'_{RMS}/\overline{p})_{pit}$ are between 1 - 1.6% and the normalized fluctuations $(q'_{RMS}/\overline{q})_{SP}$ vary between 5.3 - 7.3 %. An increase towards the centerline is found and therefore the cone model is placed slightly off tunnel axis in a region with lower disturbance level.

The spectra shown in Figure 5.23 are measured simultaneously with fluctuations in the boundary layer of the cone which are presented in the following. Figure 5.23 (a) displays the amplitude spectra of normalized pitot pressure fluctuations at a unit Reynolds number between 4.6 $\times$ $10^6/m$ and 11.35 $\times$ 10^6/m. All three pressure curves show a noticeable peak at about 410 kHz, representing the natural frequency of the pressure gauge. A typical decay of the fluctuation level versus frequency without considerable dominant peaks is visible. The RMS values of the normalized pitot pressure fluctuations decrease with rising unit Reynolds number. Such a dependency on the unit Reynolds number is an indicator that the sound waves originate in the turbulent BL of the wind tunnel walls.

Figure 5.23 (b) shows the amplitude spectrum of the heat-flux fluctuation in the stagnation point of the blunt body normalized by the corresponding mean heat-flux density obtained simultaneously. The normalized RMS value of the heat-flux density fluctuations is in the range of about 5.4 % and no dependency on the unit Reynolds number is found. The curves show peaks at the frequencies 110, 190, 250 and 330 kHz. The spectral peaks originate either from an unstable detached shock wave in front of the probe or from the temperature stratification inside the storage tube (see Heitmann et al. [52] for more detailed investigations).

The results confirm the existence of two different disturbance modes. The entropy mode shown in Figure 5.23 (b) has a higher intensity level and originates in the prehistory of the flow generation (storage tube). Temperature stratification in the storage tube causes convective vorticity and temperature fluctuations in the initial state. Hence, these temperature fluctuations are independent of unit Reynolds number and do not correlate with the measured pitot pressure fluctuations as seen in the RMS values.

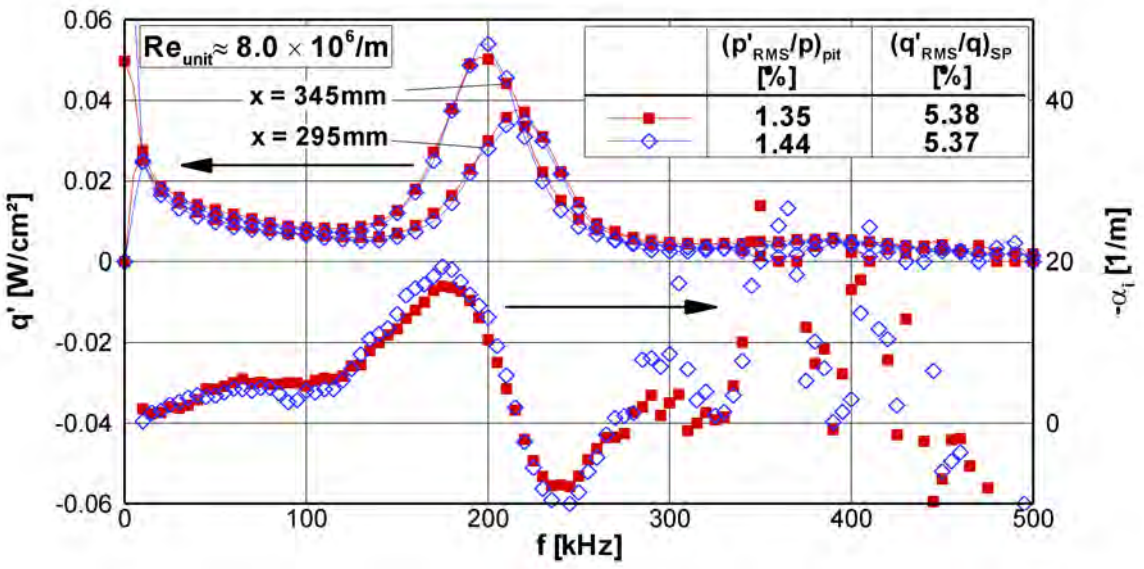

Figure 5.24: Demonstration of repeatability, amplitude spectra and amplification rates (ALTPs at x = 295 mm and x = 345 mm) obtained for runs at the same nominal conditions.

Spectral data and spatial amplification rates. The experimental data presented in the following constitute a fairly detailed and thorough basis of the BL transition process on a sharp cone. In order to document the uncertainty in the experiments, the repeatability of the experimental conditions is investigated. Figure 5.24 displays typical amplitude spectra for two tunnel runs at the same nominal unit Reynolds number $\mathrm{Re}_{unit} = 8.0 \times 10^6/\mathrm{m}$. The spectra clearly reveal the dominant second mode as peak in the frequency range between 150 - 300 kHz at both position x=295 and x=345 mm. Despite of a slightly lower maximum amplitude of the second mode at both positions in the first run, the agreement of calculated amplification rates (lower curves) is very good. Such a discrepancy in amplitude can be explained by a slight variation of the initial disturbance level in the driver tube and test section. The simultaneous stagnation-point measurements indicate such an effect - at least, the pitot-pressure fluctuations $(p'_{RMS}/\overline{p})_{pit}$ are lower for the first run (while $(q'_{RMS}/\overline{q})_{SP}$ remains approximately the same). In general, the repeatability of the runs at same nominal conditions is found to be very good and allow detailed study of growth rates for a variation of unit Reynolds number.

For the variation of unit Reynolds number, the transitional regime shifts successively across the gauges (compare Fig. 5.12 in the M6QT experiments). The amount of data obtained from a gradual shift of unit Reynolds number allows the compilation of amplitude spectra to characteristic contours showing the different stages of transition and second-mode growth and decay. Figure 5.25 displays such “footprints” for the fixed sensor

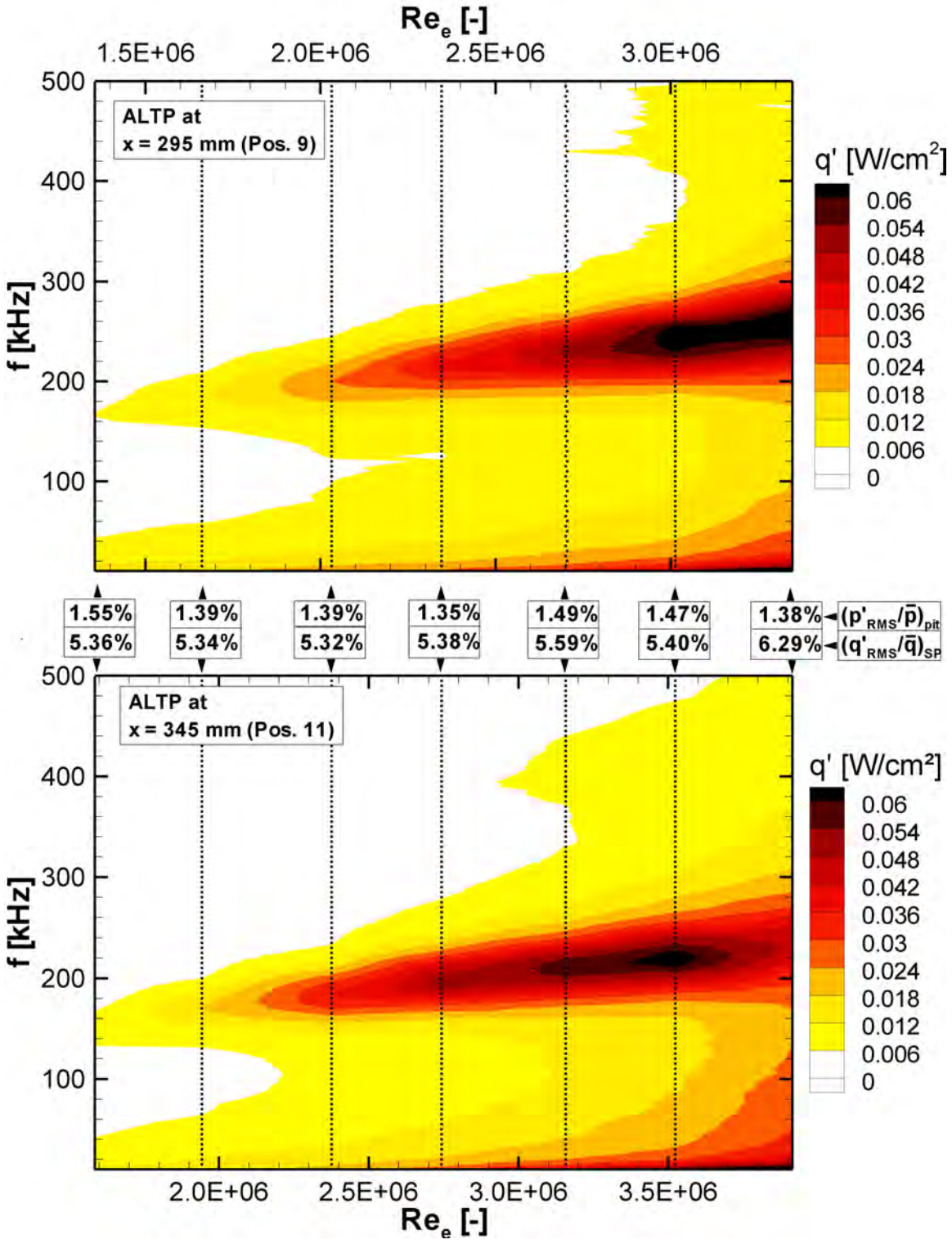

Figure 5.25: Amplitude spectra obtained from fluctuations of heat flux of ALTPs placed at (top) x = 295 mm and (bottom) x = 345 mm on the cone surface for a variation of Reynolds number.

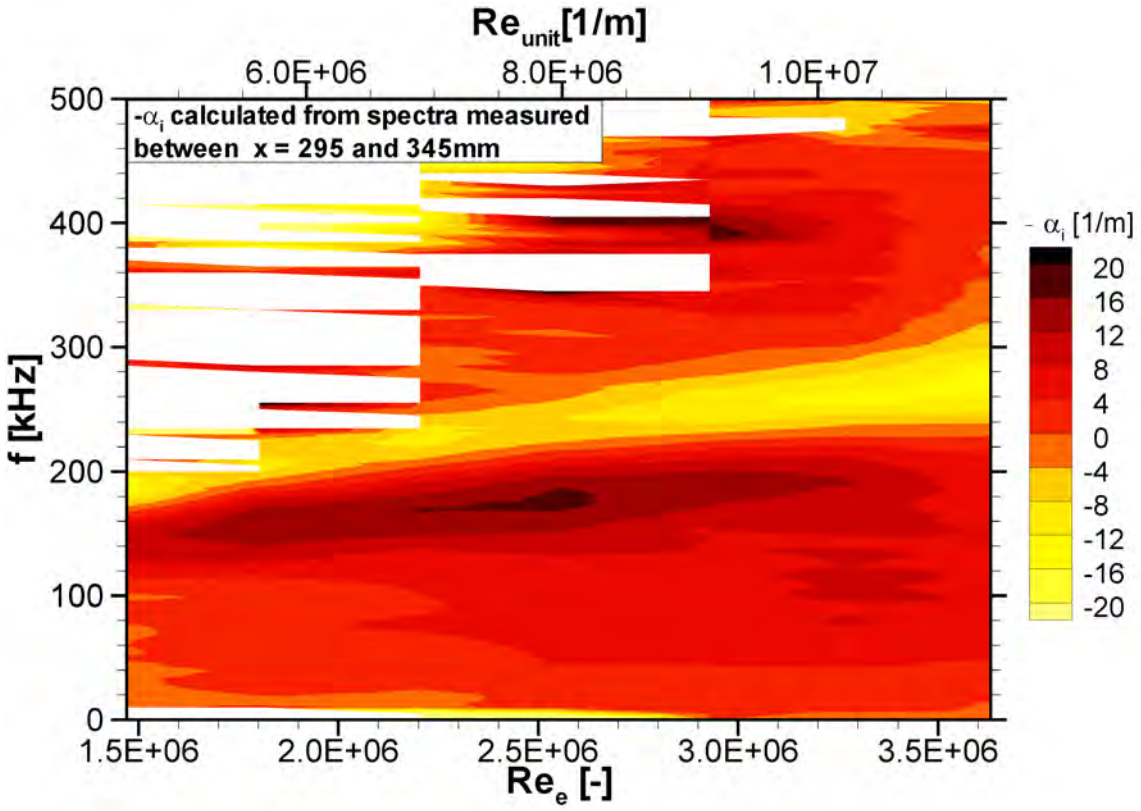

Figure 5.26: Amplification rates calculated from amplitude spectra calculated between x = 295 mm and x = 345 mm for a variation of Reynolds number.

position x = 295 mm and x = 345 mm. The figure presents only two examples of contours of ALTP amplitude spectra. All other spectra obtained from ALTP and pressure gauges are qualitatively similar. In-between the figures, the simultaneously measured disturbance level is given for each single spectrum (vertical lines). The top values are the normalized pitot-pressure fluctuations and the lower values represent the fluctuations of stagnation-point heat flux. The second mode is clearly visible between 200 and 280 kHz for the contour at x = 295 mm and between 150 and 200 kHz for x = 345 mm with increasing frequency for rising Reynolds number, respectively. The mode can be detected at a Reynolds number as low as $\sim 1.3 \times 10^6$ with a frequency of ∼150 kHz. At a Reynolds number $\sim 2.9 \times 10^6$, the first harmonic is detected at ∼420 kHz and both the lower and higher frequency portion of the spectrum starts to fill in. At $\mathrm{Re}_e \approx 3.5 \times 10^6$, the amplitude of the second-mode peak saturates (Fig. 5.25 (bottom)). The fluctuations of stagnation-point heat flux remain as expected fairly constant within certain limits $(q'_{\mathrm{RMS}}/q)_{SP} = 5.3 - 5.4\,\%$ for all runs. The same characteristic is observed for the pitot-pressure fluctuations $(p'_{\mathrm{RMS}}/p)_{pit} = 1.35 - 1.55\,\%$. They are expected to slightly decrease with growing unit Reynolds number (as shown in the previous paragraph). However, the unit Reynolds number range covered was fairly small to clearly reveal this trend.

Figure 5.26 displays amplification rates calculated from the ALTP amplitude spectra between positions x=295 mm and x=345 mm shown in Figure 5.25 for a variation of unit Reynolds number. Two regions can be identified, the lower one shows the growth rates of the second-mode instability with maximum rates of $-\alpha_i \approx 20/\mathrm{m}$ reached for Reynolds number between $2.3 \times 10^6 \leq \mathrm{Re}_e \leq 2.7 \times 10^6$. The upper region displays the growth rates of the first harmonic of the second mode. For low Reynolds numbers, the amplitudes of the harmonic are very close to the background noise level of the ALTPs and artificially high growth rates can be obtained. Therefore, such values ($-\alpha_i > 25/\mathrm{m}$) are blanked out. The growth rates of the harmonic are in the same order as the one of the second mode.

Comparison of growth rates obtained from pressure and heat-flux fluctuation measurements. In order to compare the growth rates at successive positions, the rates are normalized by the appropriate parameters at the edge of the conical boundary layer. All amplification rates based on spectral data of pressure and heat-flux gauges are determined

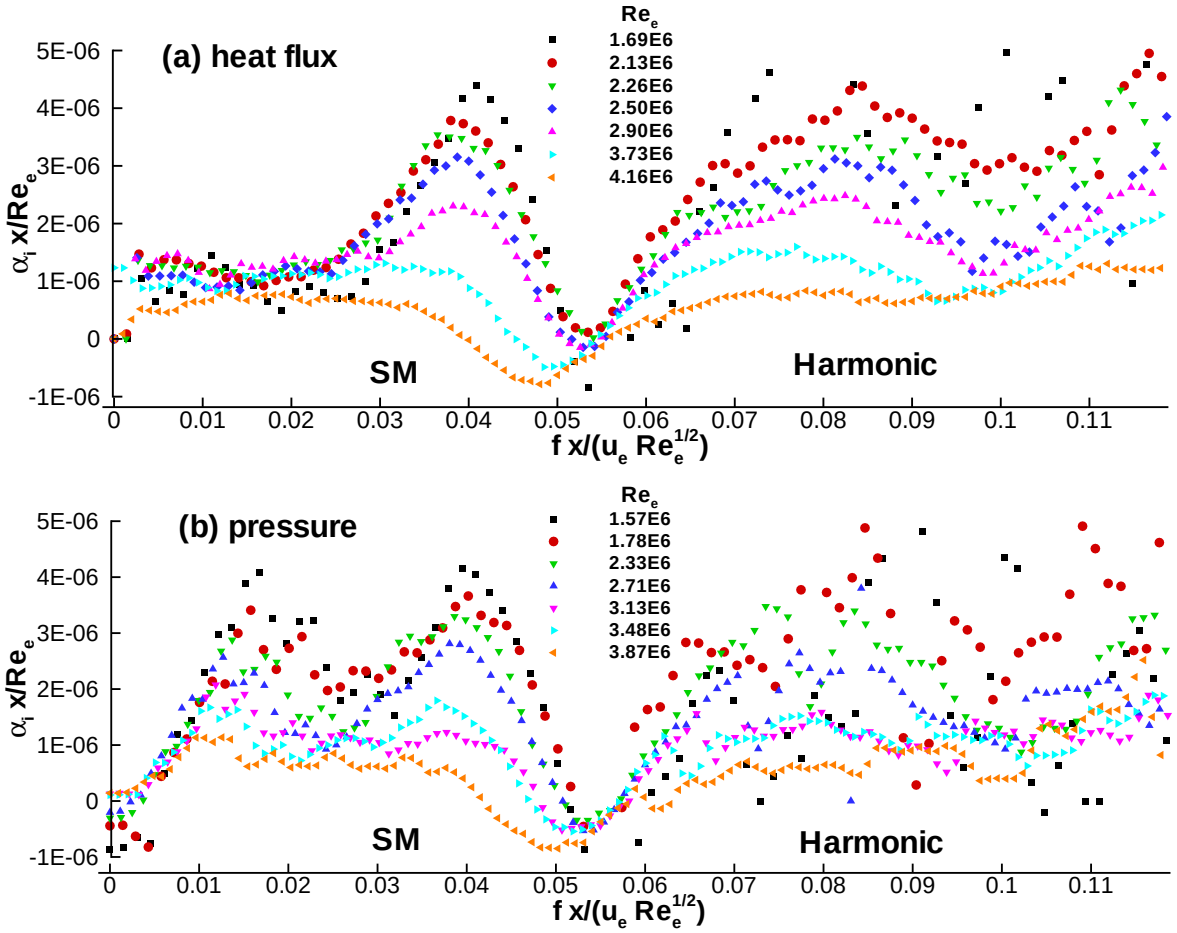

Figure 5.27: Spatial amplification rates calculated from (a) fluctuations of heat flux, (b) pressure fluctuations measured on the surface of the cone.

in the same fashion as laid out in the previous paragraph. Figure 5.27 shows the growth rates determined from (a) heat flux and (b) pressure spectra on the surface. For the chosen normalization the maximum growth rates of the second mode (SM) collapse to a reduced frequency $f x/u_e \, Re_e^{1/2} \approx 0.04$ and the maximum rates of its higher harmonic can be found at $f x/u_e \, Re_e^{1/2} \approx 0.08$. Both diagrams exhibit similar amplification rates in the frequency range of the second-mode instability within the investigated Reynolds number regime $1.57 \times 10^6 \leq Re_e \leq 4.16 \times 10^6$. Figure 5.27 displays a discrepancy between the growth rates detected by the pressure and ALTP gauges in a range between $0.005 \leq f x/u_e \, Re_e^{1/2} \leq 0.025$. The amplification rates resulting from the pressure signals show an additional peak in this frequency range. The peak is found in a bandwidth that is typical for the first-mode instability. However, the signal quality is fairly poor here and other disturbance sources like e.g. tunnel noise can not be excluded (see sec. 5.5). Further investigations studying the disturbances in this frequency range e.g. by controlled excitation are certainly of interest.

Figure 5.28 shows a direct comparison of the growth rates detected by the pressure and

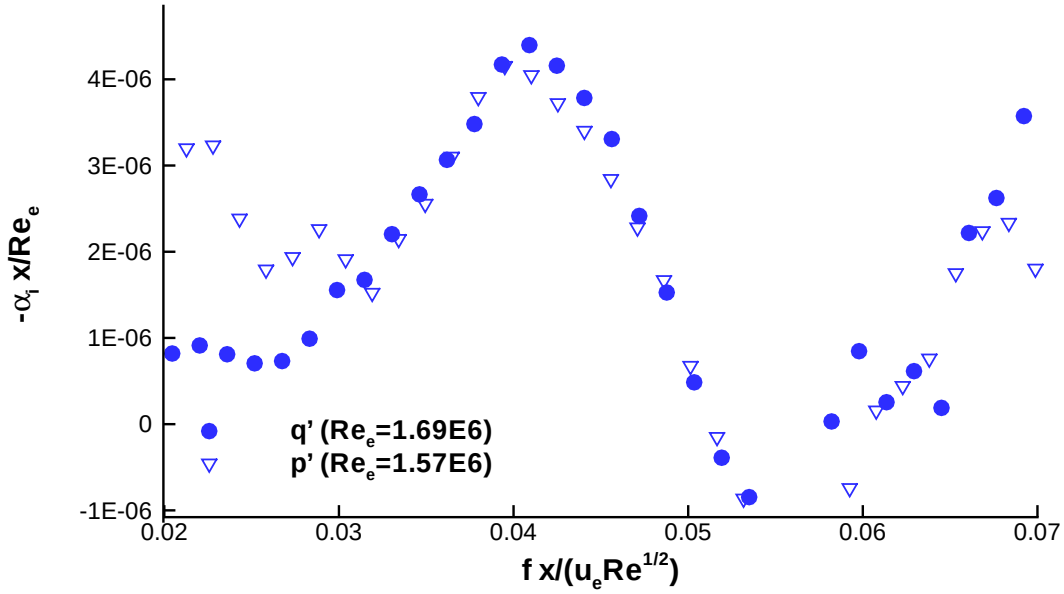

Figure 5.28: Comparison of amplification rates calculated from pressure and heat-flux spectra.

ALTP gauges in the reduced frequency range of the second mode. The agreement is very good for low edge Reynolds numbers, i.e. an early stage of BL transition. The maximum amplification rates calculated from the fluctuations of the heat flux at the wall are only slightly higher in comparison to the ones measured by the pressure gauges. It must be noted that the pressure spectra are not AFR corrected. However, this might only play a

minor role in this frequency range and remains to be verified. For higher Reynolds numbers, the amplification rates measured by the two different physical parameters deviate with increasing non-linear character of the transition process.

Comparison with M6QT results. Figure 5.29 shows a comparison of growth rates measured in the linear stage of transition in the two hypersonic facilities HLB and M6QT under noisy flow (see sec. 5.2.2). The results exhibit a good agreement of amplification rates of the second mode and also in the range of the first harmonic. This indicates a similar linear transition scenario and a general comparability of transition studies in these two facilities. A good agreement of growth rates in the later stage of BL transition is also found by Estorf et al. [31] based on pressure fluctuation measurements.

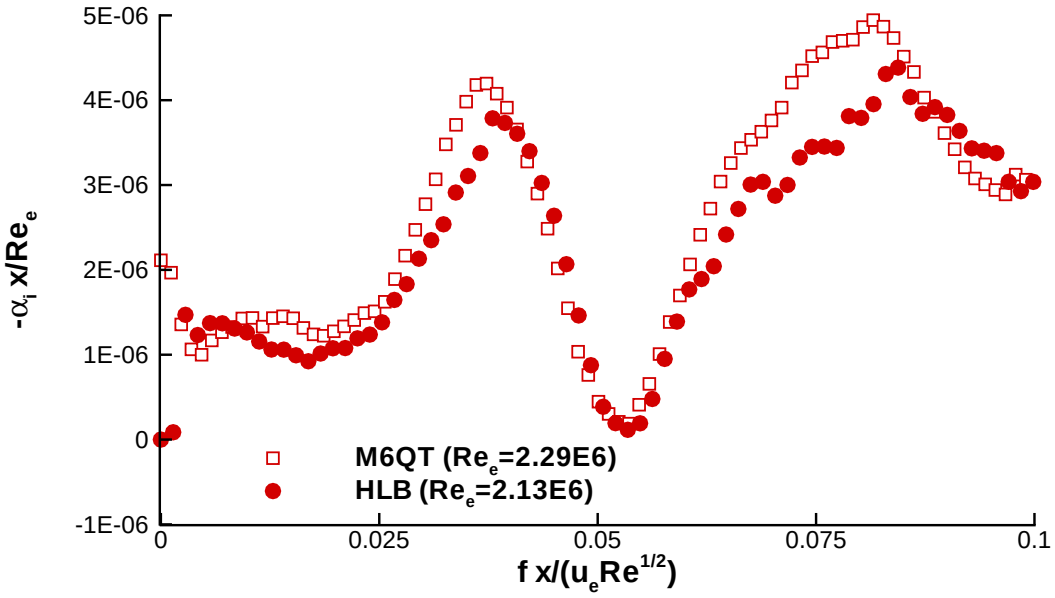

Figure 5.29: Comparison of amplification rates obtained in HLB and M6QT.

Comparison with linear stability theory. LST computations are carried out by B.V. Smorodsky of ITAM as described in section 5.2.2 for the specific conditions and Reynolds number range of the experiments in the HLB. Figure 5.30 displays the experimentally obtained and the calculated 2-D spatial amplification rates. The maximum growth rates in the experiments are systematically lower than the growth rates predicted by LST. The maximum amplification rates for the lowest edge Reynolds number $\mathrm{Re}_e = 1.69 \times 10^6$ are already ∼30 % below the maximum theoretically predicted ones. The discrepancy increases with rising edge Reynolds number, hence rising non-linear character of transition. A similar trend was observed by Stetson and Kimmel [140] and the disagreement was

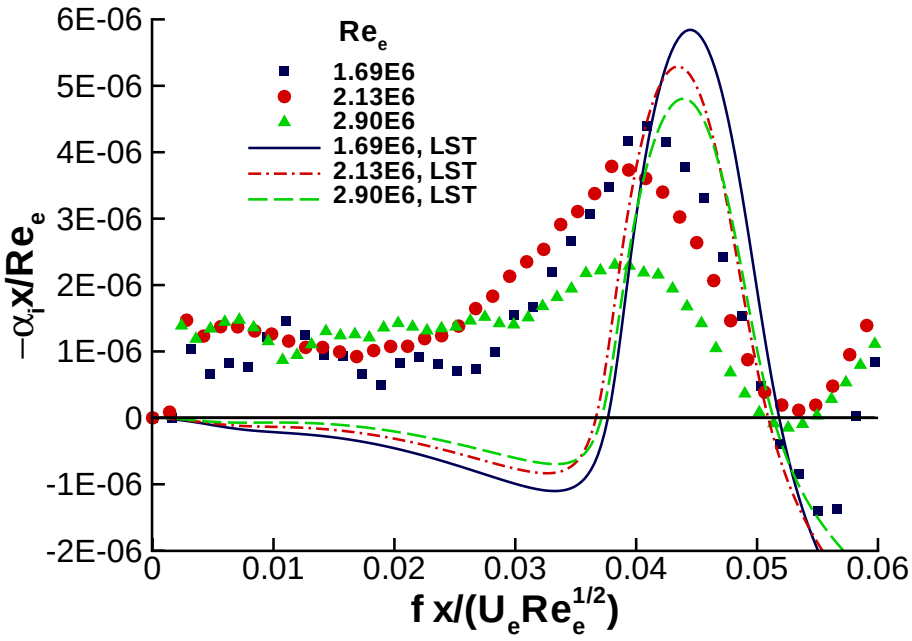

Figure 5.30: Comparison of experimental amplification rates with LST computations.

suspected to originate from the large non-linear nature of the waves. Lower experimental growth rates are also observed in the transition studies on the same cone model in the M6QT in section 5.2.2. The reader is referred to this section for a discussion of further possible influences like e.g. superposition of 3-D modes and wall temperature rise.
In addition, the reduced frequency range of the second mode predicted by LST is slightly higher - the frequency corresponding to the maximum computed growth rate is about 8 % larger for $\mathrm{Re}_e = 1.69 \times 10^6$. This effect is very likely caused by a small angle of attack of the cone.

Comparison of disturbance spectra with spectra on the cone surface. So far, the RMS values of pitot-pressure and stagnation-point heat flux are used to indicate the disturbance level within the test section. More important, however, is the spectral distribution of disturbances that allow the comparison of amplitudes in the relevant spectral ranges on the cone surface and in the stagnation point. Figure 5.31 shows such normalized amplitude spectra on the cone surface at two different Reynolds numbers in reference to normalized fluctuations of heat flux in the stagnation point. At low frequencies, the normalized fluctuations on the surface are already higher by a factor of 10 than the ones measured in the stagnation point. In the frequency range of the second mode, factors of

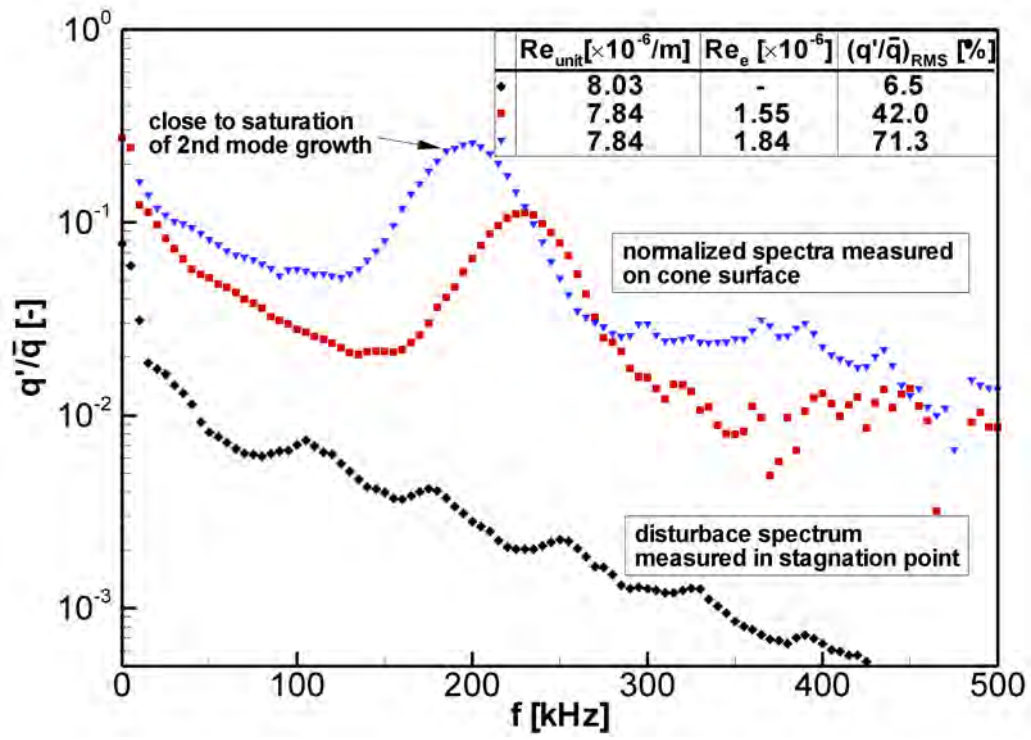

Figure 5.31: Comparison of normalized amplitude spectra on the cone surface and in the stagnation point.

20 - 100 between the normalized fluctuation amplitudes on the surface and in the stagnation point are reached. The RMS values of the fluctuation spectra in Figure 5.31 are given to quantify generally the trend of this value during BL transition. It rises from from 42% to 71% on the cone surface, whereas the RMS value determined by the stagnation-point probe is only 6.5%.

Investigation of the roughness effect created by a flat ALTP sensor module in the cone surface. In order to investigate the possible influence of the roughness created by the flat ALTP sensor module on BL transition, a study by means of artificial roughness placed upstream of the sensor array is carried out. The question that arises for the presented transition study is, whether the surface roughness created by the sensor modules is small enough not to affect transition. A criterion that is proposed to quantify a surface roughness in such a way is the Reynolds number $\mathrm{Re}_k = \rho_k \mathrm{u}_k \mathrm{k}/\mu_k$ based on the maximum roughness height k (see review by Schneider [129] and references therein). Here, boundary-layer computations are carried out to calculate specific Re_k-values. It is stated that in general a roughness with $\mathrm{Re}_k < 10 - 25$ is unlikely to affect transition (unless there is a mechanism for amplifying weak streamwise vorticity). This criterion is used as an indicator in combination with measured amplitude spectra with and without artificial

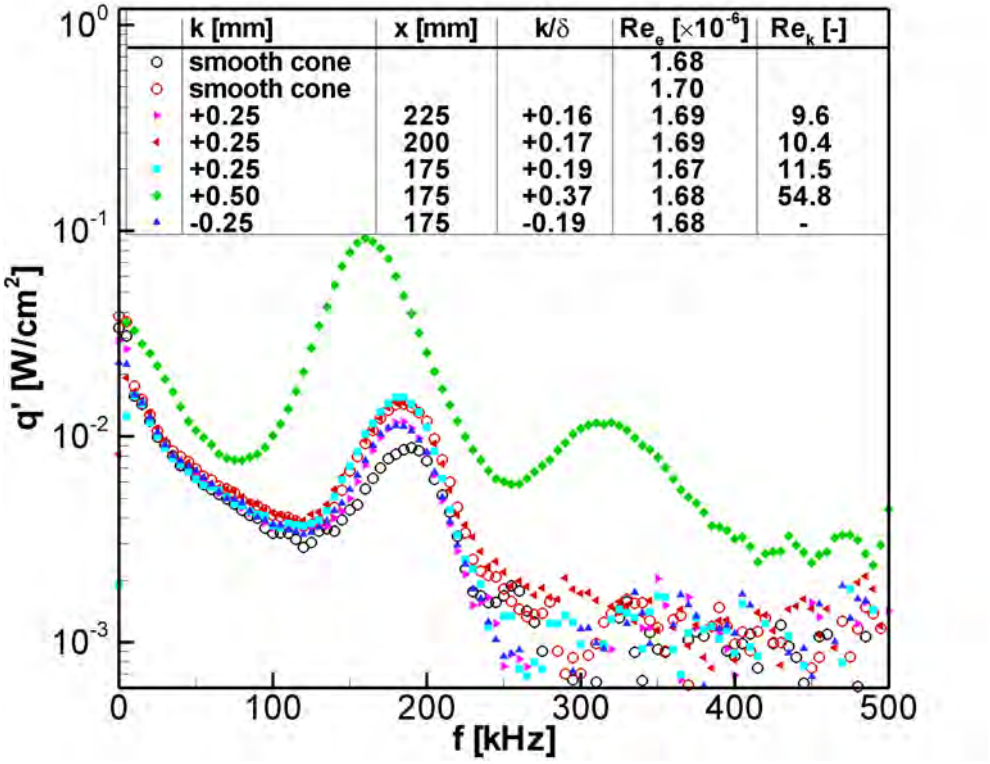

Figure 5.32: Amplitude spectra for a variation of roughness elements placed upstream of an ALTP at x=295 mm in reference to spectra measured on a smooth cone.

roughness element.

Contoured roughness elements with a diameter of 8 mm, simulating the ALTP sensor module, are extended and retracted at several x-location upstream of the ALTP array. In the present experiments, the maximum roughness height created by the most upstream ALTP sensor, when its streamwise diameter is aligned with the cone surface, is k≈0.25 mm. Figure 5.32 shows several amplitude spectra of the most upstream ALTP with the roughness elements in reference to the smooth cone spectra. The elements are extended by k≈0.25 mm for increasing upstream positions (from x=225 to 175 mm) and by k≈0.5 mm at the most downstream position x=175 mm. Thereby the ratio of roughness height k to boundary-layer thickness δ (taken from BL computations) and Re_k is successively increased. In addition, the influence of a cavity of k≈ -0.25 mm is investigated.

The results show that all roughnesses with k ≈ 0.25 mm and the cavity does not have a noticeable effect. The amplitude of the second mode varies within the repeatability of the reference cases for the smooth cone (hollow symbols). Only the roughness of k ≈ 0.5 mm, corresponding to $k/\delta = 0.37$ at the most upstream position shows a noticable influence. The maximum amplitude of the second mode is increased by a factor of 6, a shift of the peak towards lower frequencies is visible and the amplitude of the higher harmonic

strongly increases. For this case, $\mathrm{Re}_k \approx 55$ is beyond the interval that is postulated to have unlikely influence on transition. All other experiments stay below or at the lower limit of this interval ($\mathrm{Re}_k < 10 - 25$), because Re_k was always below 12 in all experiments. Therefore, this criterion seems to apply for the present experiments. The roughness created by the flat ALTP sensor module seems to be marginal and does not affect the transition study on the present smooth cone experiments.

Conclusions. The result of the first experimental study of hypersonic BL transition on a cone using a staggered array of fast-response ALTP and pressure gauges is presented. Spatial amplification rates of the second-mode instability and its first harmonic are calculated from amplitude spectra of measured pressure and heat-flux density fluctuations. The agreement of the amplification rates measured by pressure and ALTP gauges is found to be good in the frequency range of the second-mode instability and its first higher harmonic in the early stage of BL transition. The comparison of the growth rates measured by the ALTP in the HLB and the M6QT confirmed a general comparability of the transition scenario under noisy flow.
Normalized fluctuation amplitudes on the surface of the cone and in the stagnation point exhibit amplification factors ranging from 20 to 100 near the frequency range of the second mode. For low frequencies a factor of 10 is obtained. In addition, the non-intrusive character of the streamwise sensor array is examined and confirmed for the actual experiments.

5.4 Hypersonic Transition on Circular Sharp Cone at M=12 : Experiments at ITAM AT-303

Up to now, experimental stability investigations of a conical boundary at a free stream Mach numbers larger than M=8 are very sparse. The following experiments show spectral wave amplitude distributions at M=12 obtained from a sensor array and the derivation of growth rates in a conical BL for the first time (to the author's best knowledge). With increasing Mach number, higher Mack modes become more and more relevant for the transition process in hypersonic BLs. The use of a staggered array of fast-response pressure and ALTP heat-flux gauges allows the comparison of growth rates detected by heat-flux and pressure fluctuations on the surface.
The unique conditions of the AT-303 hypersonic facility resulting from long run times and high stagnation temperatures make these transition studies of special value. The ALTP and pressure gauges allow highly time-resolved experimental studies where conventional

measurement techniques like hot-wires cannot be used due to their limited durability, limited overheat ratio and temporal resolution. Especially the high ratio of total temperature to wall temperature in the AT-303 improve the signal to noise ratio of the ALTP and reach into the regime relevant for the flow simulations of hypersonic flight vehicles.

5.4.1 Experimental Setup

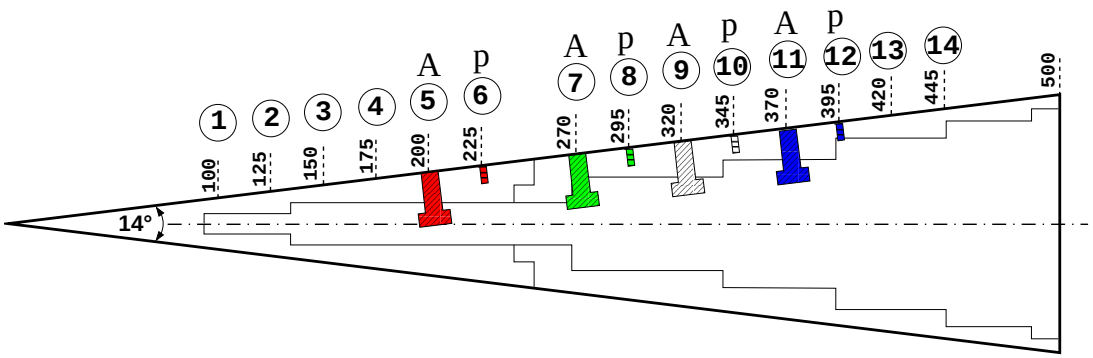

Figure 5.33: Schematic of circular cone model with installed ALTP and pressure gauges.

Position (Number)	arc length x [mm]	Sensor (Serial number)	Sensitivity s [μV/(W/cm^2)]	Sensitivity s [μV/Pa]
5	200	ALTP 941	80.0	
6	225	PCB 1 (4437)		20.3
7	270	ALTP 942	110.1	
8	295	PCB 2 (4342)		22.0
9	320	ALTP 943	101.1	
10	345	PCB 3 (4343)		24.5
11	370	ALTP 1004	117.0	

Table 5.4: Specification of installed ALTPs and PCB pressure gauges.

The experiments are carried out in the AT-303 facility of ITAM. The reader is referred to a section 5.1.1 for a short description of the facility including references. The experimental conditions realized in the measurement campaign are listed in Table 5.5. The first 7 runs are used to identify the transitional regime on the cone and to adjust its angle of attack. The AT-303 is equipped with a mechanical sting-mount alignment system. The cone-model alignment is carried out in successive runs by comparison of the maximum

Run (AT-303)	p_0 [bar]	T_0 [K]	$Re_{unit} \times 10^{-6}$ [1/m]
1 (2352)	258	980	13.68
2 (2353)	523	1068	23.83
3 (2354)	110	905	6.72
4 (2355)	108	897	6.70
5 (2356)	107	896	6.65
6 (2357)	106	894	6.62
7 (2358)	107	895	6.67
8 (2359)	89	1028	4.34
9 (2360)	133	952	7.42
10 (2361)	144	976	7.69
11 (2362)	118	924	6.95
12 (2363)	163	1008	8.22
13 (2364)	197	1064	9.03
14 (2365)	216	1108	9.23
15 (2366)	257	1165	10.06
16 (2367)	198	1066	9.05
17 (2368)	181	1046	8.55
18 (2369)	179	1047	8.44
19 (2370)	133	951	7.44
20 (2371)	119	921	7.05

Table 5.5: Experimental conditions of AT-303 campaign.

frequency of the second-mode instability at rotation angles of 0, 90 and 180 degrees (Runs 3 - 7). The model is adjusted to a frequency shift of $f < 10\,kHz$ between the three angular positions. During the campaign, a unit Reynolds number range of $4.3 \times 10^6/m \leq Re_{unit} \leq 23.8 \times 10^6/m$ is covered.

The cone model used in the experiments is already described in section 5.2. The model is instrumented with a staggered array of ALTP and PCB pressure gauges (see Figure 5.33 and Table 5.4). The instrumentation is very similar to the arrangement used in the HLB experiments described in section 5.3. More details on the specifications of the sensors can be found there.

Data acquisition and processing. Two synchronized 4 channel, 12 bit data acquisition cards are used for capturing of the voltage signals of the ALTPs and pressure gauges. The TiePie 4 card has a maximum sampling rate of 128 KS/s and the L-card was operated

with the maximum rate of 500 KS/s. A time period of up to 300 ms is evaluated for the ALTP spectra depending on the available measuring time of each single run. A period of 65 ms is processed for the pressure gauges limited by the maximum sampling length of the data acquisition card. The calibrated signals are divided into overlapping windows with a constant size of 800 samples with an overlap of 500 samples. Averaging, noise subtraction and AFR correction and the calculation of the spatial amplification rates is carried out as described in section 5.2.1.

5.4.2 Experimental Results

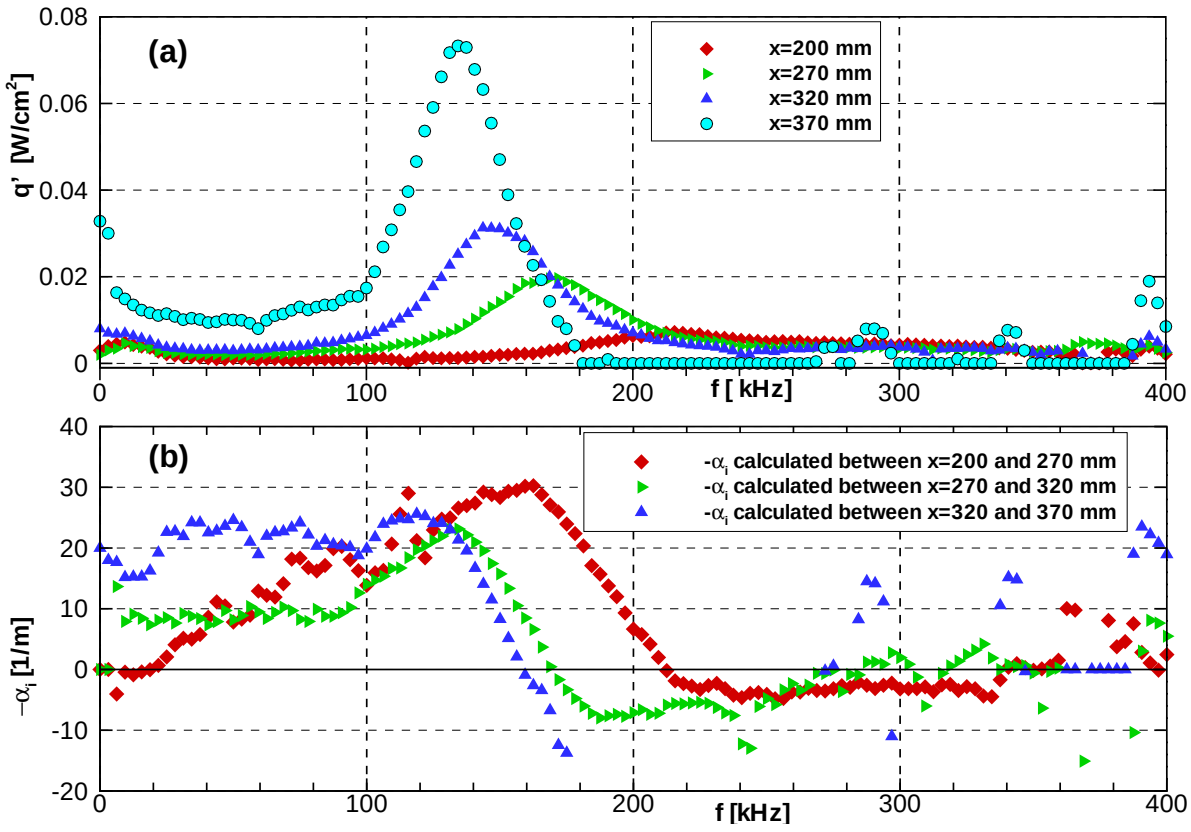

Figure 5.34: (a) Amplitude spectra and (b) amplification rates calculated from ALTP signals (Run7, $\mathrm{Re}_{unit} = 6.67 \times 10^6/\mathrm{m}$).

Spectral data and spatial amplification rates. Figures 5.34(a) and 5.35(a) display typical amplitude spectra simultaneously obtained from the ALTP and pressure gauges in an early stage of BL transition (Re_{unit}=6.67×10^6/m). A characteristic shift of the second-mode frequencies towards lower values with increasing x-location and hence rising BL thickness is clearly visible in both diagrams. The quality of the amplitude spectra of the

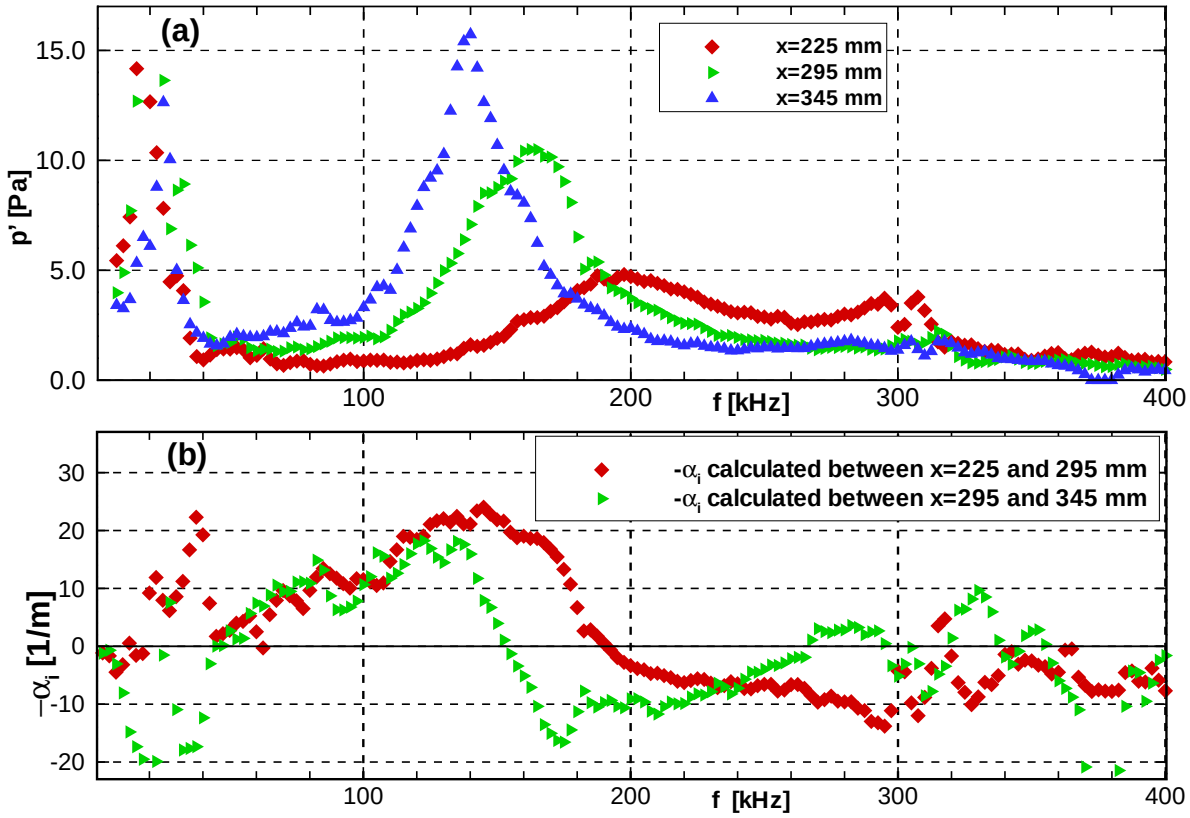

Figure 5.35: (a) Amplitude spectra and (b) amplification rates calculated from pressure signals (Run7, $\mathrm{Re}_{unit} = 6.67 \times 10^6/\mathrm{m}$).

ALTP is better due to the longer time period of 300 ms used for averaging in comparison with the pressure spectra that only use a time signal of 65 ms in length. The ALTP at the most downstream position (x=370 mm) is very sensitive to high electronic noise level and interference during the operation of the facility. Therefore, its spectral data are not considered in the following.

The lower diagrams in Figures 5.34 and 5.35 display the growth rates calculated from the spectra shown above. The maximum amplification rates between the first two ALTPs (x=200 and 270 mm) in Figure 5.34 (b) are higher in comparison with the growth rates between the further downstream positions. This might results from the amplitude of the measuring signal being very close to the background noise, hence producing artificially high maximum growth rates at the left edge of the second-mode bell. The contour in Figure 5.36 (a) displays the compilation of spatial amplification rates for a variation of unit Reynolds number between the two most upstream locations of ALTP sensors. As already mentioned, the maximum of the absolute growth rates are subject to uncertainty, however the contours indicate the very early stages of second-mode growth in a limited frequency band between 100 and 250 kHz and edge Reynolds numbers as low as $\mathrm{Re}_e \approx 2 \times 10^6$.

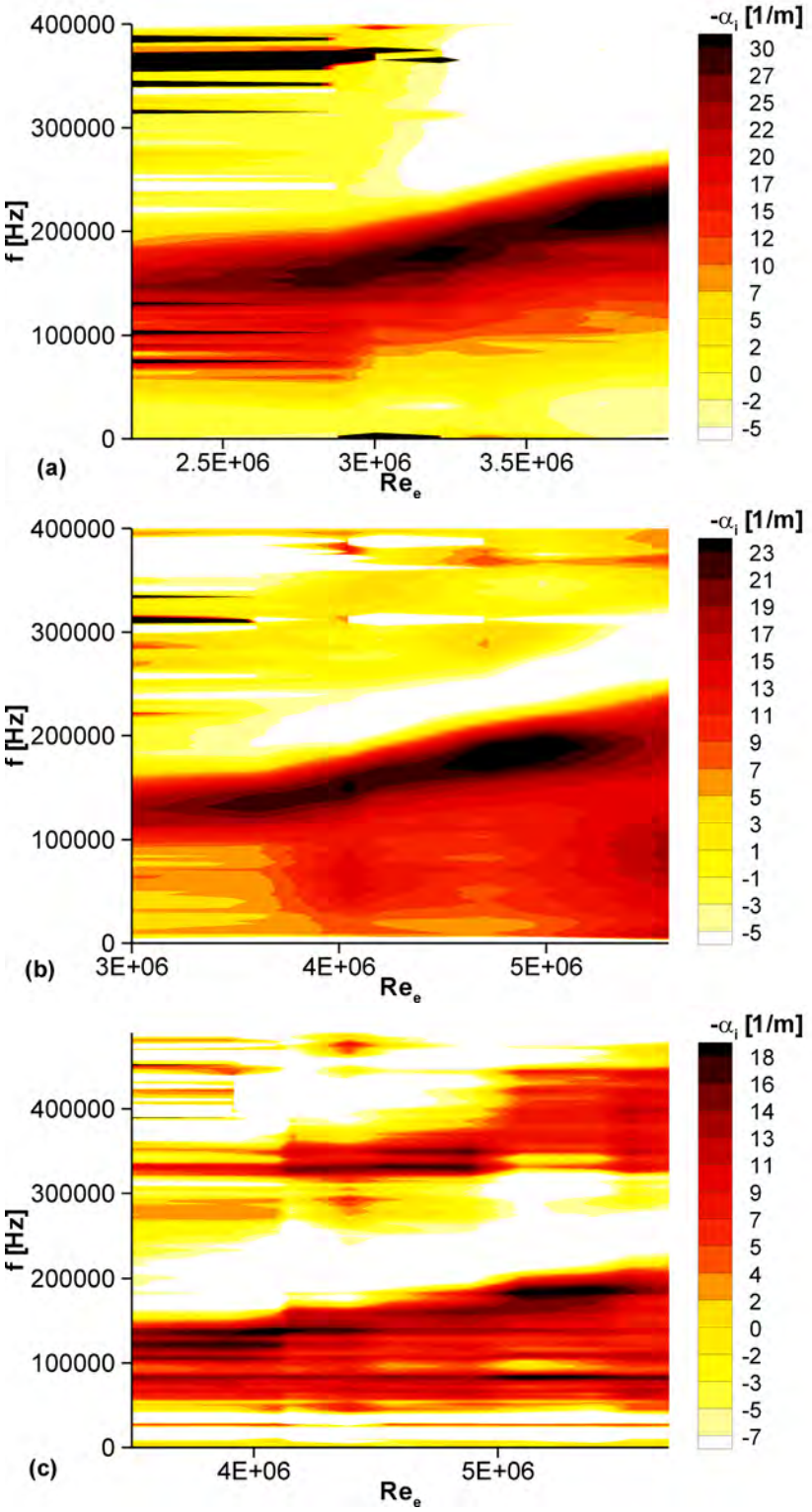

Figure 5.36: Spatial amplification rates calculated from fluctuations of heat-flux spectra between (a) x=200 and x=270, (b) x=270 and x=320 and surface pressure spectra between (c) x=225 and x=295.

Figure 5.36 (b) shows the amplification rates calculated between the next two successive ALTP locations (x=270 and 320 mm). The signal quality results into reliable absolute amplification rates with maximum growth of $-\alpha_i \approx 24/\mathrm{m}$ approached at $\mathrm{Re}_e \approx 4.7 \times 10^6$. It should be noted that the frequency range below and above the second mode is stronger amplified than in Figure 5.36 (a).

Figure 5.36 (c) displays the amplification rates obtained from the amplitude spectra of the pressure sensors located at positions x=200 and 270 mm. Despite of the scattering of the growth rates resulting from the limited averaging of the spectra, the contour clearly reveals the growth of the second mode in a frequency band below 200 kHz. The amplified frequency range extends far into the low frequency range, where also certain dominant

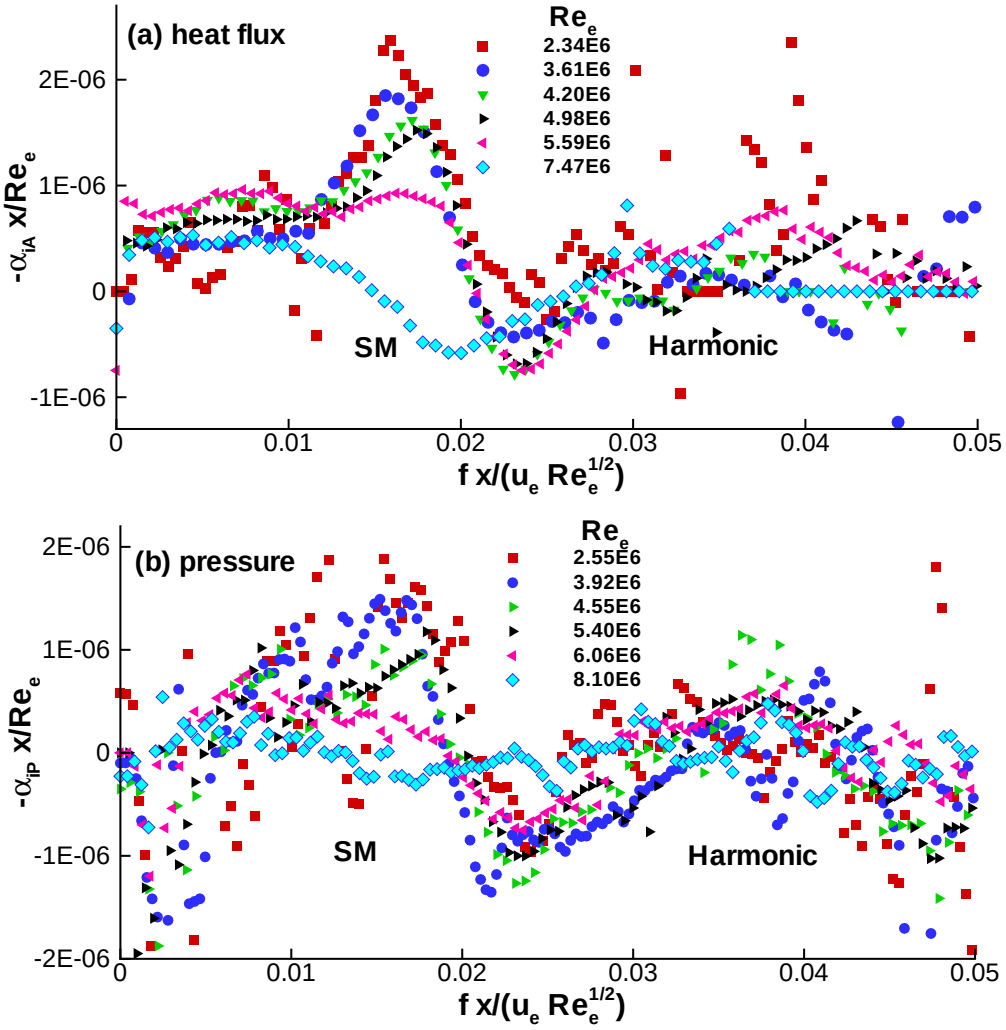

Figure 5.37: Normalized spatial amplification rates calculated from (a) heat-flux spectra (calculated between x=270 and x=320); (b) pressure fluctuation spectra (calculated between x=295 and x=345) simultaneously measured on the surface of the cone.

features are visible that might indicate first-mode growth or amplified disturbances originating from tunnel noise. In contrast to Figures 5.36 (a) and (b), a frequency range between 350 - 450 kHz, typical for the higher harmonic of the second mode, is clearly amplified. The growth of the harmonic appears to be stronger in terms of fluctuations of surface pressure than in wall heat flux detected by the ALTP.

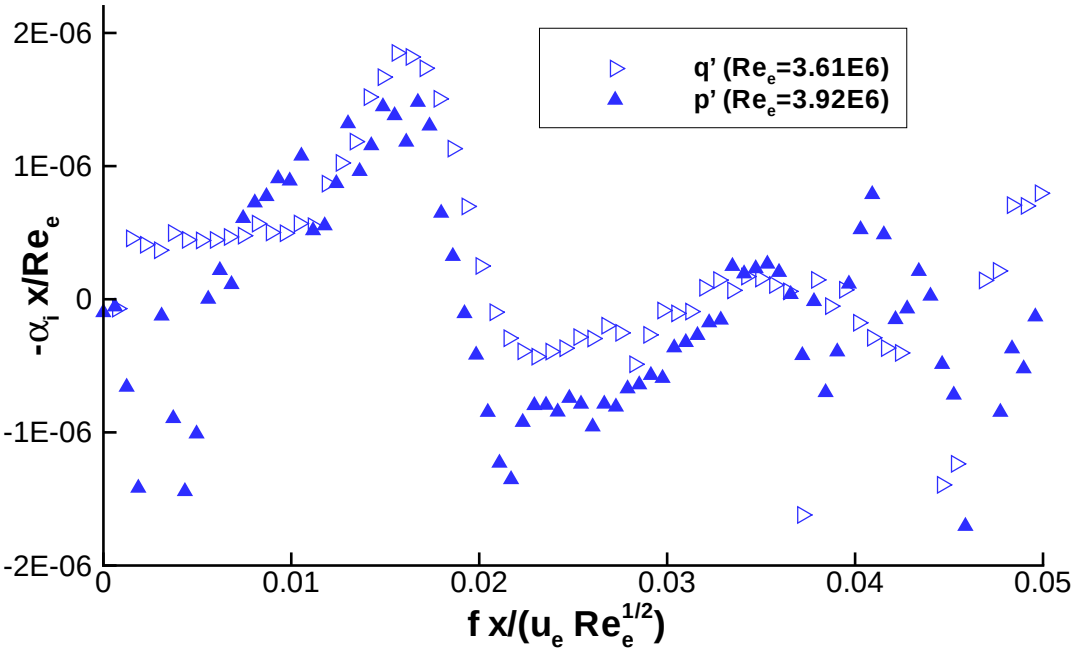

Figure 5.38: Comparison of amplification rates calculated from pressure and heat-flux spectra.

In order to allow better quantitative comparison of growth rates detected by the staggered pressure and heat-flux gauges, the amplification rates are normalized by relevant BL edge condition. Figure 5.37 displays the reduced amplification rates calculated from (a) ALTP heat-flux spectra between x=270 mm and x=320 mm and (b) pressure spectra between x=295 mm and x=345 mm. The variation of edge Reynolds number covers a range from the early stage of BL transition up to the non-linear stage and beginning of turbulent flow. The growth rates of the second mode (SM) collapse for approximately the same reduced frequency in both diagrams. The quantitative comparison of the maximum growth rates in Figure 5.37 (a), (b) and the direct comparison in Figure 5.38 in the early stage of BL transition show that the amplification rates measured by the pressure sensors are systematically slightly lower than the one detected by ALTPs for the same Re_e range. A similar effect is also observed in the cone experiments at M=6 in the HLB (sec. 5.3.2). The peaks in 5.37 (a) detected by the ALTP in a range between $0.025 \leq f\,x/(u_e\sqrt{Re_e}) \leq 0.035$ resembles very likely the growth rates of the first higher harmonic of the second

mode. Its maximum amplification rates are significantly lower than the one of its fundamental. Whereas, the harmonic detected by the pressure gauges in a similar frequency range appears to be stronger amplified (Fig. 5.37(b)). The maximum growth rates are higher and amplification is registered in a broader bandwidth than the one detected by the ALTP.

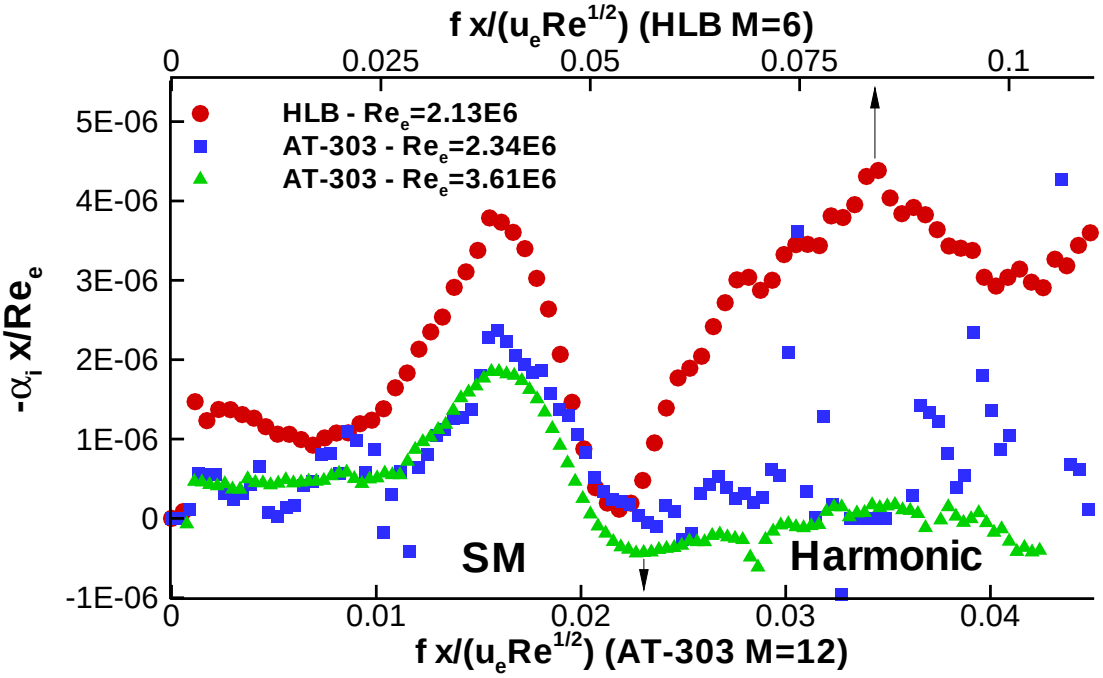

Figure 5.39: Comparison of amplification rates obtained in HLB and AT-303.

Comparison with HLB (M=6) results. The growth of the first higher harmonic seems not only to be different in terms of surface pressure and wall heat-flux fluctuation at M=12, but also differs fundamentally in comparison to the results at M=6 in the HLB and M6QT. Figure 5.39 displays the growth rates in the early stages of BL transition at M=6 (HLB) and M=12 (AT-303). The reduced frequency range was adjusted in such a way that the maximum rates of the second mode collapse on the abscissa. The absolute values are not relevant since the stability diagrams of M=6 and M=12 differ significantly. However, the ratio of the amplification rate of the harmonic and its fundamental show a very different behavior. At M=6 the growth was found to be approximately equal for both pressure and heat-flux fluctuations. At M=12, however, the harmonic shows significantly lower amplification rates which delivers experimental evidence that different mechanisms might be responsible for transition at higher Mach numbers.

Comparison with linear stability theory. The comparisons of the experimentally obtained amplification rates with linear stability theory computation can help to shed some

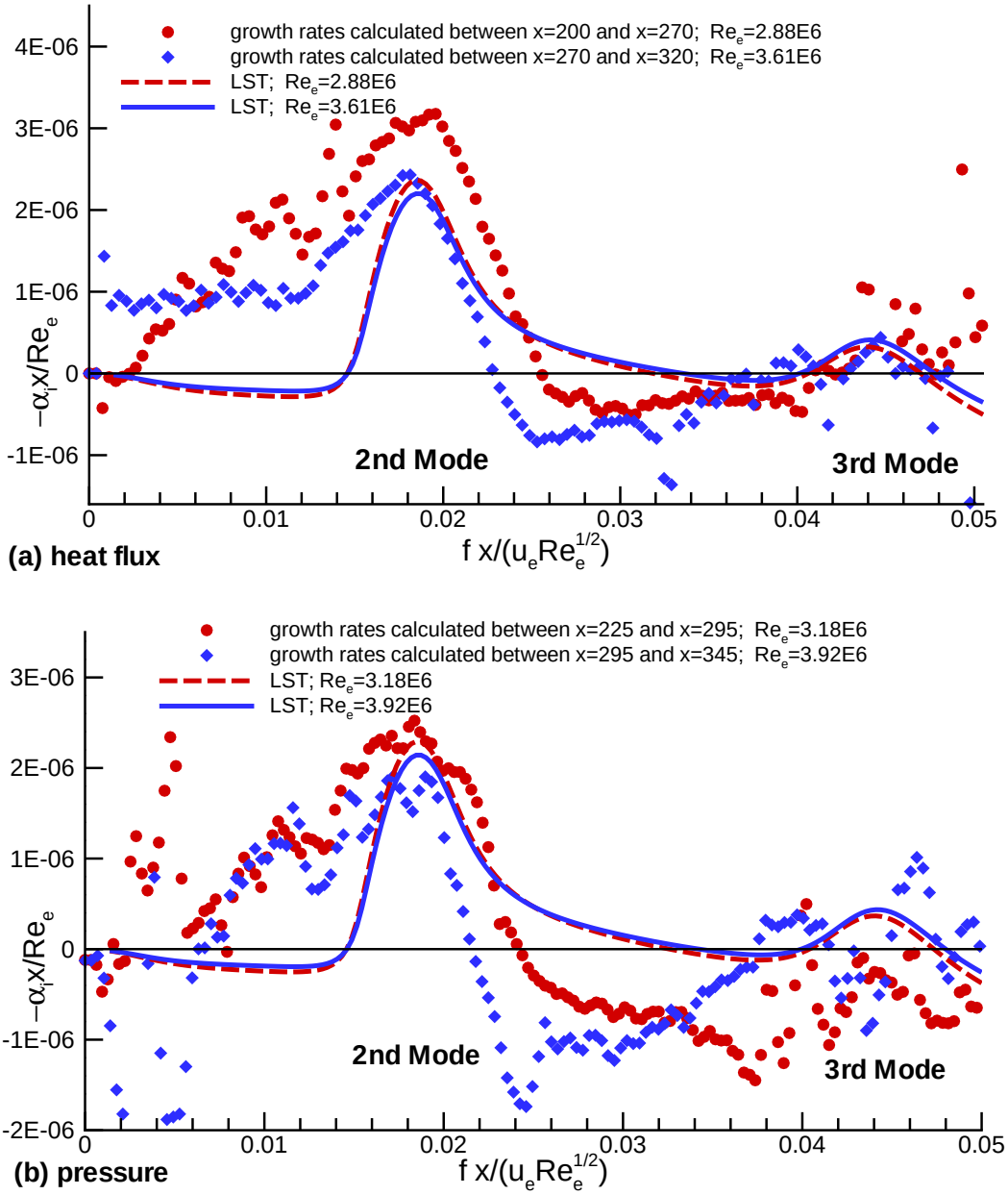

Figure 5.40: Comparison of amplification rates calculated from (a) fluctuations of heat flux, (b) pressure fluctuations with LST results (Run7, $\mathrm{Re}_{unit} = 6.67 \times 10^6/\mathrm{m}$).

light into the transition scenario experienced at M=12. LST compuations were carried out by B. Smorodsky of ITAM as described in section 5.2 for the specific conditions of the experiments. Figures 5.40 and 5.41 compare the amplification rates in a unit Reynolds number range between $6.67 \times 10^6/\mathrm{m} \leq \mathrm{Re}_{unit} \leq 9.23 \times 10^6/\mathrm{m}$. In this range a good agreement between the experimental data and LST is found. Figure 5.40 shows the growth rates of (a) fluctuations of heat flux and (b) pressure fluctuations in reference to growth

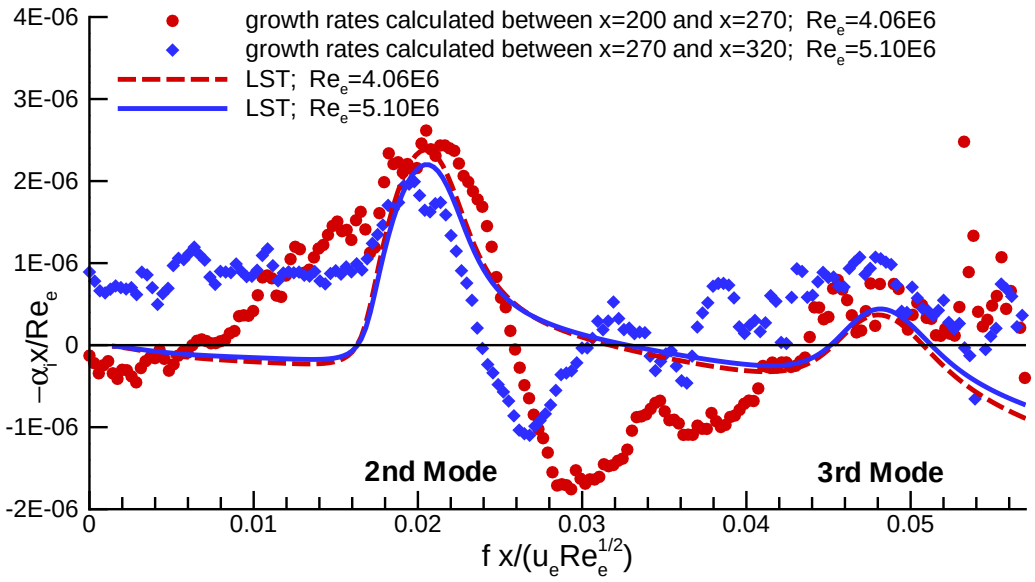

Figure 5.41: Comparison of amplification rates calculated from heat-flux spectra with LST results (Run14, $\mathrm{Re}_{unit} = 9.23 \times 10^6/\mathrm{m}$).

rates predicted by LST for corresponding Reynolds numbers. In Figure 5.40 (a), the experimentally determined amplification rates calculated between x=200 and x=270 mm ($\mathrm{Re}_e = 2.88 \times 10^6$) exhibit larger rates in the range of the second mode than predicted by LST. The discrepancy can be explained by the low signal to noise ratio between the two most upstream ALTP sensor locations that was mentioned earlier. For further downstream positions (x=270 and x=320 mm) and larger edge Reynolds numbers in Figure 5.41, very good agreement of maximum growth rates and amplified frequency range of the second mode is found. The growth rates in Figure 5.40 (b) measured by the pressure sensors are also in good agreement with the LST predictions in the same reduced frequency range as detected by the ALTP.

Amplification of the disturbances in the low-frequency range can be found in all diagrams in contrast to LST predictions. Here, LST assumes only 2-D waves and first-mode is not considered in the computations. The strong amplification in the low-frequency range detected by the pressure gauges in Figure 5.40 (b) indicates some growth at specific frequencies. This might also be due to disturbances that originate from the noise spectrum of the tunnel.

In the higher frequency range of Figure 5.40 (a), LST predicts a noticeable amplification of a third instability mode at M=12 between $0.04 \leq \mathrm{f\,x}/(\mathrm{u}_e \sqrt{Re_e}) \leq 0.05$. The experimental data in this extended frequency range are suspect to higher uncertainties due to limited signal to noise ratio. Yet the growth rates determined by the ALTPs are in

fairly good agreement with LST predictions. The growth rates obtained from the pressure spectra in Figure 5.40 (b) are attributed to even larger scatter in this frequency range, but show also a trend towards amplification. It should be noted that the pressure spectra are not AFR corrected which could have an significant effect on the quantitative value of amplification rates measured in such a high frequency range. In addition, Fig. 5.41 displays growth rates detected by ALTPs at a higher unit Reynolds of $\mathrm{Re}_{unit} = 9.23 \times 10^6/\mathrm{m}$ that also indicate the amplification of a third mode. Thus, the results present evidence for the first experimental detection of a third-mode instability at M=12 to the author's best knowledge

Conclusions. For the first time, simultaneous time-resolved measurements of pressure and heat-flux fluctuation on the surface of a circular cone are carried out at a free-stream Mach number of M=12. The experimentally simulated high stagnation temperatures of 900 - 1200 K and stagnation pressures between 90 - 520 bar approach conditions that can be considered as relevant for the experimental simulation of flight conditions. The quality of the spectral data allow the calculation of amplification rates from surface pressure and amplitude spectra of wall heat flux. The amplification rates are documented from the early stage of BL transition up to the non-linear stage and beginning of turbulent flow. The comparison of the experimental results with LST prediction in the linear stage exhibit good agreement in the reduced frequency range of the dominant second mode. Evidence indicates the experimental detection of a third-mode instability at M=12. Agreement between theory and experiment is found for the amplification rates obtained from ALTP spectra. The growth of disturbances in the range of the harmonic of the second mode is found to be captured differently by the pressure and ALTP sensors, i.e. fluctuations of surface pressure and wall heat flux. Furthermore, the amplification of the harmonic differs also from the scenario that is observed in cone experiments in the lower hypersonic regime of M=6 of the HLB and M6QT (see sec. 5.2 and 5.3).

5.5 Hypersonic Transition on a Flat Plate at M=6

The premise of the experiments described in the following section is to study laminar-turbulent transition of hypersonic BLs on a flat plate. The compressible BL of a sharp flat plate was the basis of many analytical studies and computations in the past. However, experiments that deliver reliable data for comparison of such a planar BL encounter several severe complications. The data can be blemished by 3D effects, since a flat plate model will always have a limited width, leading edge bluntness or inhomogeneity; by uncertainties in the determination of the angle of attack and by the general problem of

acoustic noise radiated from the nozzle boundary layer in different wind tunnels.
The dominance of the second-mode instability was shown in extensive experimental studies for conical BLs and the results agree well with theoretical LST predictions (see previous sections and review by Stetson [140] and references therein). However, experiments studying planar BLs (flat plate: [66], [148], hollow-cylinder: [141]) show that the "second-mode disturbances appear to play only a minor role in the transition process". In contrast, low frequency disturbances seem to dominate the flow. The disturbances grow in a frequency band which is typical for the first mode and even in a range that might be stable in LST. A dominance of the second mode could not be observed. The issue of the planar-versus-conical BL anomaly is extensively discussed by Stetson et al. [141], including comparisons with previous experiments, parameter effects like noise level, unit Reynolds number dependency etc. The instabilities of planar BLs appear to be fundamentally different from the conical case. Several question were raised (e.g. different receptivity to free-stream disturbance, prediction by LST etc.) and many aspects of this phenomenon remain unclear. In the present experiments, instability waves are measured by a staggered array of single-point ALTP and pressure sensors and spatial amplification rates are determined (see also Roediger et al. [117]).

5.5.1 Experimental Setup

The experiments are carried out in the Hypersonic Ludwieg Tube Braunschweig (HLB) described in section 5.3.1. A 630 mm long and 200 mm wide flat plate is installed in the HLB. It does not span the whole tunnel width, hence leaving space between the tunnel side walls and the right and left edges of the plate. The leading edge is sharp and beveled with an angle of 4°. The flat plate is installed ~ 90 mm off the the tunnel axis in order to avoid a conical compression wave that is known to focus on the axis within the test section. The plate had a small negative angle of attack in reference to the geometric axial centerline in order to account for the weak expanding flow in the test section, mentioned in section 5.3.1. Yet the uncertainty of a small angle of attack and non-parallel flow remains. The model used in the HLB experiments is instrumented with a streamwise, staggered array arrangement of fast-response ALTP heat flux and pressure sensors. Figure 5.42 shows their arrangement ("p" denotes pressure sensor, "A" represents an ALTP heat-flux gauge). The gauges are installed in two circular inserts (two out of three) with a diameter of 90 mm and are flush mounted in order to minimize surface roughness. The first sensor of Insert 2 is positioned 192 mm downstream of the leading edge, and the first one of Insert 3 at a distance of 284 mm. Their spacing is 16 mm within each insert. The array is composed of the same sensors that are used in the circular cone experiments in section 5.3. Data analysis is also performed in a similar manner, only the sizes of the extracted

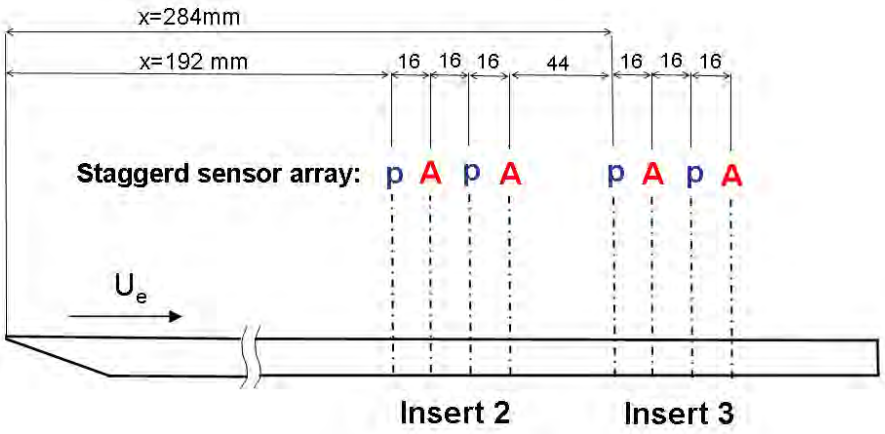

Figure 5.42: Schematic of the flat plate model.

windows is reduced to 800 samples each and an overlap of 500 samples in order to achieve a better spectral resolution of the low-frequency range. More details on the instrumentation and data analysis can be found in section 5.3. Furthermore, the calculation of the spatial amplification rates is discussed in section 5.2.1.

5.5.2 Experimental Results

Figure 5.43 (a) and (b) show time traces of successive pressure and ALTP sensors, respectively. The time signals provide a first insight and give approximations of the frequency ranges of disturbances present in the flat plate BL. The pressure gauges detect a contin-

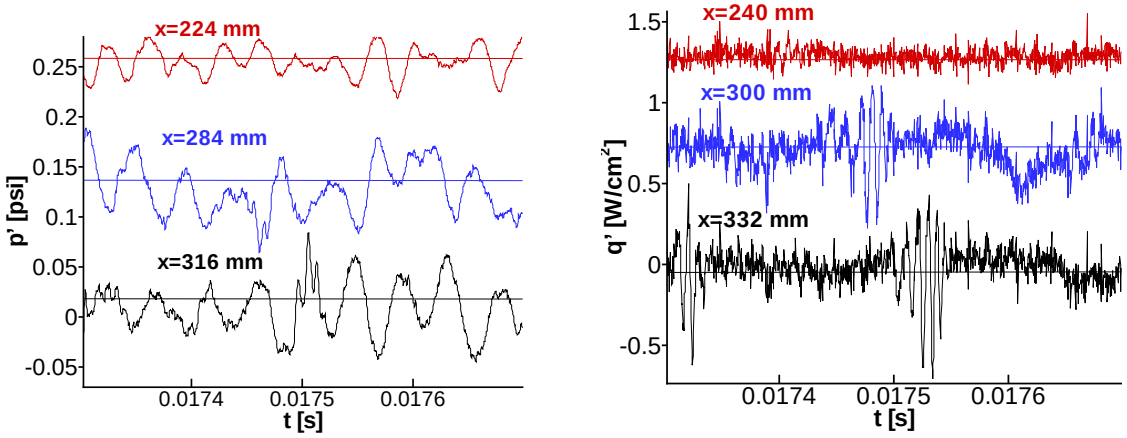

(a) (b)

Figure 5.43: Time trace of (a) pressure sensor, (b) ALTP heat-flux gauge for successive x-locations measured simultaneously (Run 16, $\mathrm{Re}_{unit}=7.1\times10^6$).

uous low-frequency disturbance with a frequency f ≈ 24 kHz. In addition, high-frequency wave packets with f ≈ 130 kHz superimposed on low-frequency disturbances can be found in the trace of the pressure sensors at x = 284 and 316 mm. The ALTP gauges detect similar wave packets with a slightly lower frequency of f ≈ 100 kHz. The calibrated time traces show that the amplitude of the disturbance rises in downstream direction. A phase velocity ∼ 650 m/s can be calculated for the wave packet detected by the ALTP between x=300 and 332 mm resulting into a wavelength $\lambda \approx 6.5$ mm. The average BL thickness (taken from BL computations) between these two location is $\delta \approx 3.34$ mm. Hence, the ratio of $\lambda/\delta = 1.95$ indicates a typical feature of the second-mode instability ($\lambda \approx 2\,\delta$). It must be noted that the time signals are not averaged and the scattering can be large for other windows. The result imply that the second mode has rather a wave packet character than the one of a continuous pulsation.

Figure 5.44 (a) displays surface pressure amplitude spectra for variation of Reynolds number at the fixed location x=284 mm. In the spectral range below 50 kHz, four discrete pressure disturbances are visible. Their magnitude increases with rising (unit) Reynolds number, however their frequency remains constant. The amplitudes and frequencies of the peak between 80 - 150 kHz increase with growing Reynolds number. This feature is characteristic for BL instability modes. The spectral range corresponds well to the amplified frequencies typical for a second-mode instability, predicted by LST calculations. A first higher harmonic of the second mode is also visible at ∼ 180 kHz for a certain Reynolds number range. The peak at ∼ 300 kHz is also observed in other experiments [31] and is thought to be an effect of the sensors (although it is is far below the resonance frequency given by the manufacturer).

Figure 5.44 (b) shows the corresponding amplitude spectra of heat flux (AFR corrected) measured by an ALTP gauge at x=300 mm for a variation of Reynolds number. In the range between 60 - 150 kHz, a behavior similar to the one detected by the pressure sensor is visible. Instead of several discrete peaks, as present in the pressure spectra, the heat-flux spectra in the low-frequency range (<60 kHz) show only one single dominant peak. Its frequency increases with unit Reynolds number and its amplitude grows and decays in a certain Reynolds number range. Disturbances in this low frequency range seem to be amplified at lower unit Reynolds numbers and are strongly damped past a certain Reynolds number ($\mathrm{Re}_e \approx 1.4 \times 10^6$). In the Reynolds number range between $1.4 \times 10^6 \leq \mathrm{Re}_e \leq 1.6 \times 10^6$, these low-frequency disturbances coexist with the higher-frequency disturbances, presumably the second mode.

Figure 5.45 and 5.46 show contours of heat flux and pressure spectra for a variation of Reynolds number at a fixed x-location. All pressure and heat-flux spectra at the same unit Reynolds number are captured simultaneously. These contours are tailored to trail

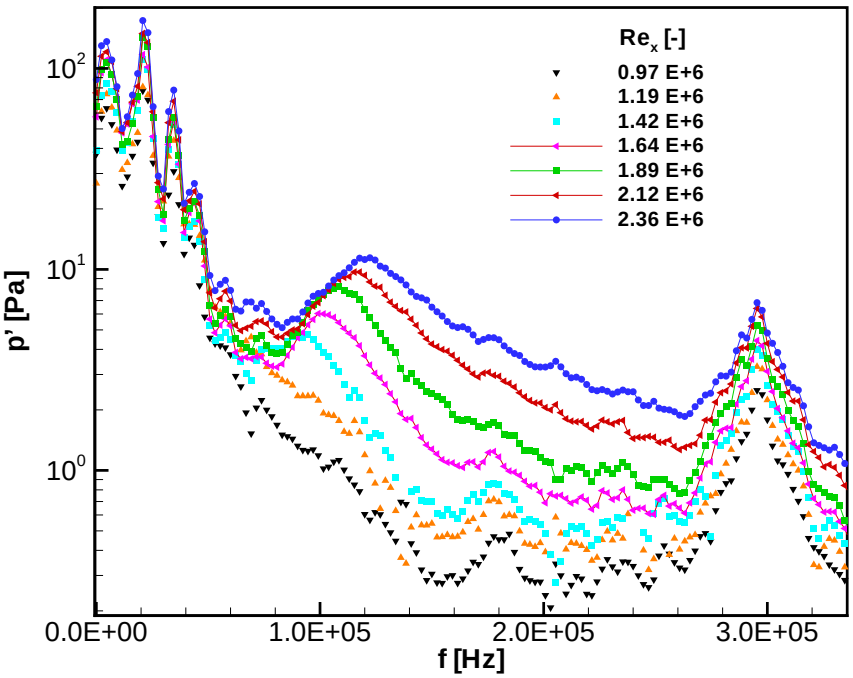

(a)

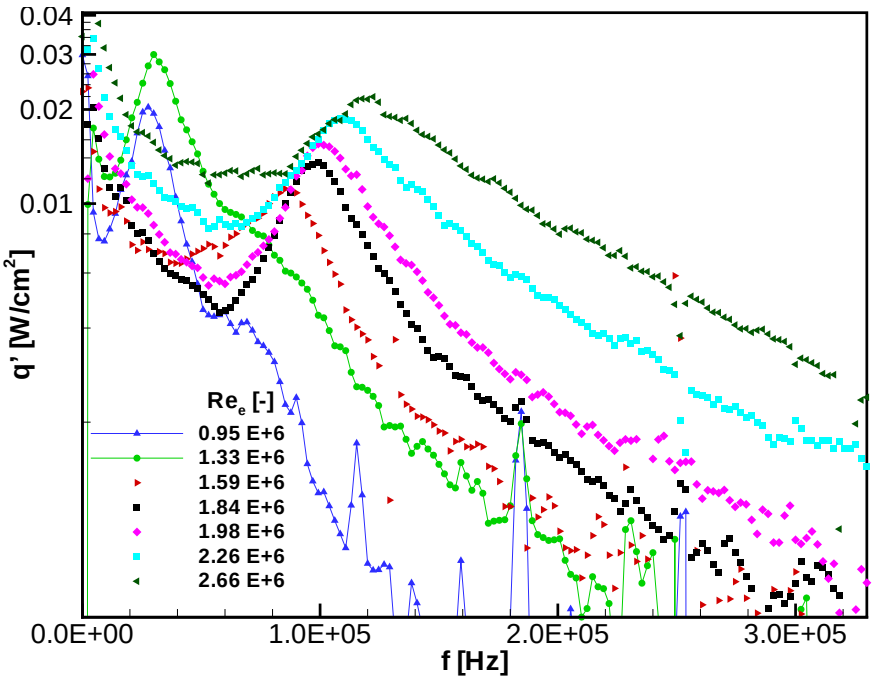

(b)

Figure 5.44: (a) Pressure spectra for varying unit Reynolds number at x=284 mm ; (b) Heat-flux spectra (AFR corrected) for variation of unit Reynolds number at x=300 mm.

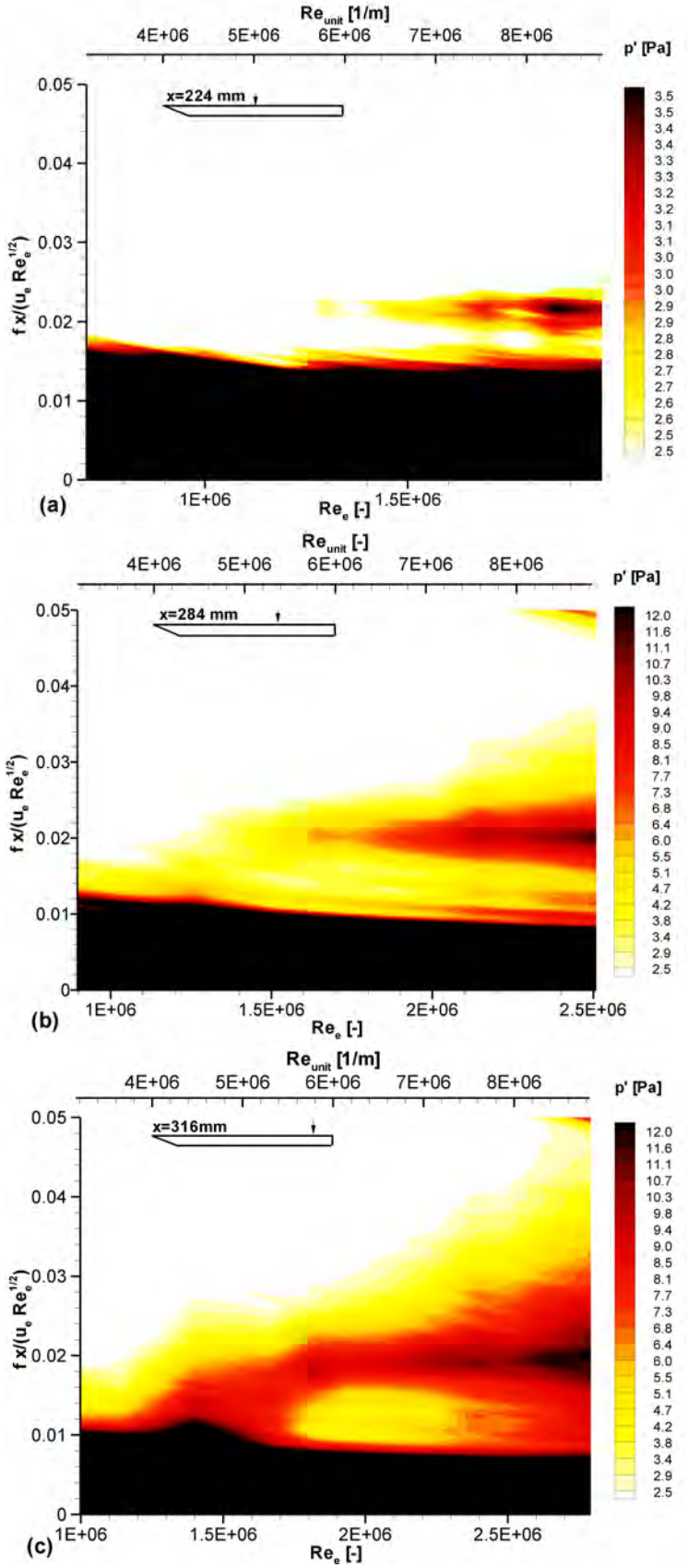

Figure 5.45: Pressure spectra for variation of unit Reynolds number at (a) x=224 mm, (b) x=284 mm, (c) x=316 mm.

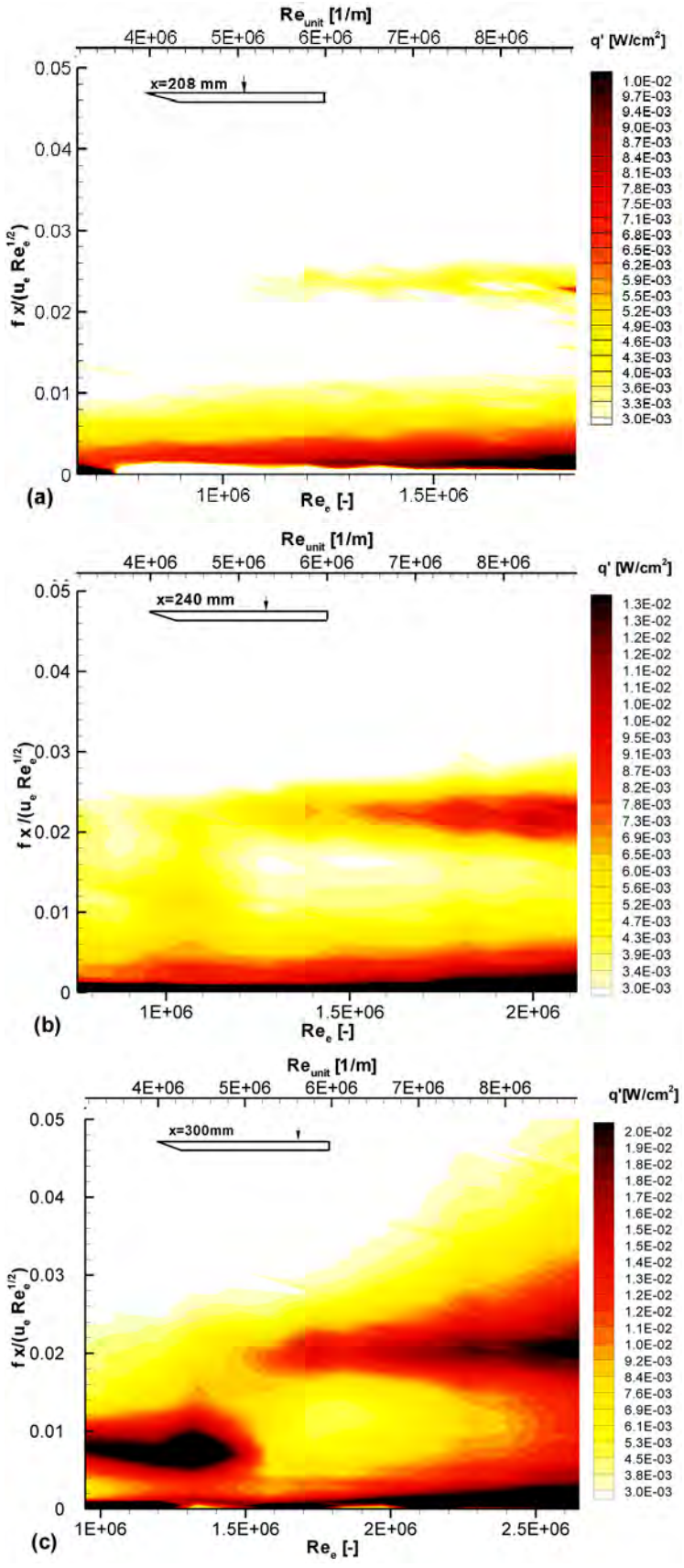

Figure 5.46: Heat-flux spectra for variation of unit Reynolds number at (a) x=208 mm, (b) x=240 mm, (c) x=300 mm.

and identify the evolution of the second mode along the plate. Therefore, the frequency is normalized by boundary layer edge conditions, calculated from measured stagnation conditions. The maximum collapses for all pressure and heat flux contours to a constant value of $\mathrm{f\,x}\,/\,(\mathrm{u}_e\sqrt{Re_e}) \approx 0.020 - 0.022$. In the early stages of the transitions process at the most upstream x-positions (Fig. 5.45 (a) and 5.46 (a)), the second mode is detectable for Reynolds numbers as low as $\sim 1.2 \times 10^6$. At further downstream positions, the superposition of the low-frequency disturbance smears the peak of the second mode. Please note that the contour coloring levels are different for each single plot. The maximum "sensitivity" of the color level is increased in downstream direction. Thereby individual features of each contour are enhanced. For example, the broadening of the second-mode peak with rising Reynolds number is clearly visible. In addition, the superposition of the second-mode with low-frequency disturbances is characterized in more detail. In contrast to the second-mode instability, the low-frequency disturbances seem not to scale with Reynolds number. The amplitude of the peaks grow and broaden centered around a fixed unit Reynolds number of $\sim 4.5 \times 10^6$/m (best visible in Fig. 5.45 / 5.46 (b) + (c)). Beyond a certain unit Reynolds number, the disturbances in the low frequency band are strongly damped which is not typical for a BL instability mode like first mode. The two characteristics mentioned, might indicate that the disturbance is created from acoustic noise or interaction of acoustic disturbances with the flat plate BL. However, this is only speculation and receptivity mechanisms remain unclear, especially because a similar disturbance could not be found in cone experiments in the HLB presented in section 5.3. Other explanations or sources have to be investigated in future experiments like e.g. disturbances traveling from the lower side of the plate [86], leading-edge inhomogeneity or roughness influence.
Moreover, the low-frequency disturbances appear to have a strong influence on the second-mode instability. The modes seem to superimpose and merge in the later stages of BL transition. The quality of the heat-flux and pressure spectra allows the calculation of spatial growth rates. The following comparison with LST computations might give a first indication of the extent of influence of the superposition.

Figure 5.47 shows the amplification rates $-\alpha_i$ versus normalized frequency calculated from (a) pressure spectra between x=284mm and x=316 mm and (b) ALTP heat-flux spectra between x=300 mm and x=332 mm. The rates obtained from pressure and heat flux are qualitatively similar. The maximum growth rate of the fundamental second mode and its first harmonic are about the same in the extended frequency range. However, a quantitative comparison shows that maximum growth rates measured by the pressure sensors are systematically lower than the ones detected by ALTPs for the same Re_e. Similar results are also obtained on the cone in sections 5.3 and 5.4 at M=6 and M=12,

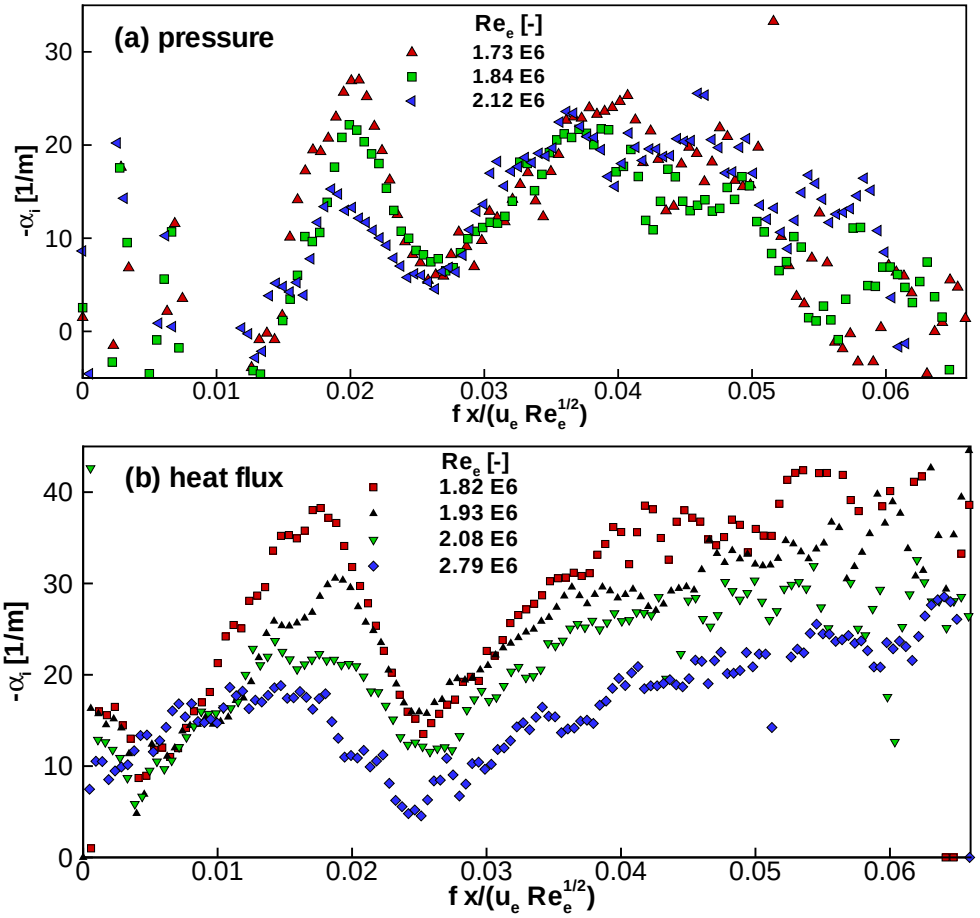

Figure 5.47: Amplification rates $-\alpha_i$ calculated from (a) Pressure spectra between x=284mm and x=316 mm; (b) ALTP heat-flux spectra between x=300 mm and x=332 mm.

respectively. Furthermore, maximum amplification rates of the fundamental disturbance measured by the ALTP appear at slightly lower normalized frequencies. In addition, the range of amplified frequencies measured by the ALTP seems to be somewhat broader than the one detected by the pressure sensors. These two features, could imply that a stronger influence of the superposition with the low-frequency disturbance on the ALTP signal exists, since the decaying rates with increased Reynolds number indicate an already advanced stage of BL transition. However, growth rates for lower Reynolds numbers could be only calculated from ALTP signals. The small amplitudes of pressure fluctuation created by the waves are below the detectable limit of the pressure sensors at further upstream positions (the front pressure sensors is located 16 mm upstream of first ALTP sensor).

Comparison with linear stability theory. Figure 5.48 (a) shows the amplification rates of the ALTP spectra between x=208 and x=240 mm (most upstream, spacing Δx = 32

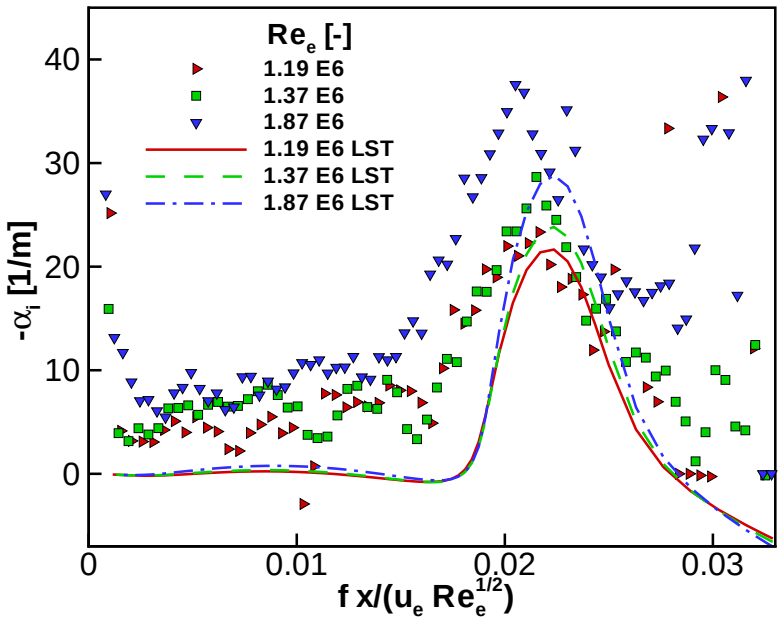

(a)

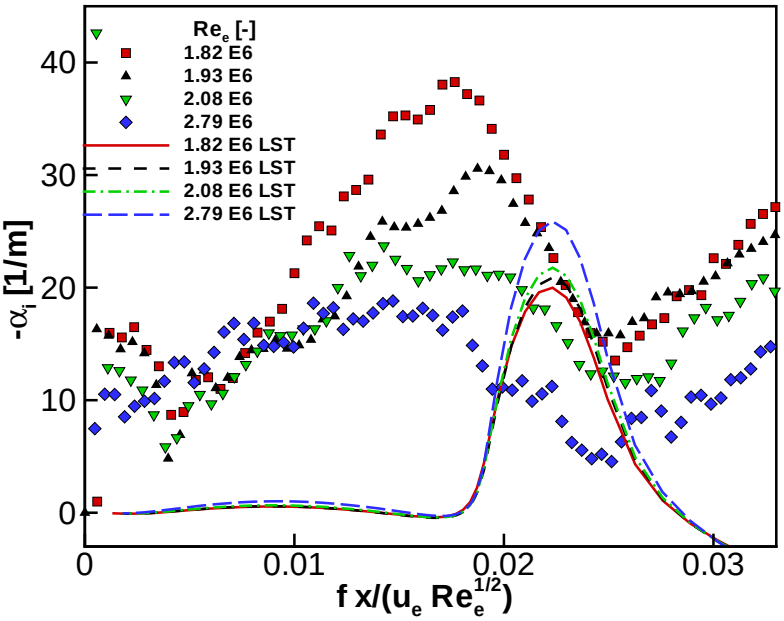

(b)

Figure 5.48: Amplification rates $-\alpha_i$ calculated from ALTP spectra (a) between x=208mm and x=240 mm (most upstream, spacing Δx= 32 mm); (b)between x=300mm and x=332 mm (most downstream, spacing Δx= 32 mm) in comparison with LST.

mm), resulting into $1.19 \times 10^6 \leq \mathrm{Re}_e \leq 1.87 \times 10^6$. Figure 5.48 (b) depicts the later stages of transition in a detailed view (expansion of Fig. 5.47) as comparison with the earlier

stages in Figure 5.48 (a). The bandwidth of amplified frequencies for lower Reynolds numbers is considerably smaller than for later stages of transition. LST calculations are carried out for the entire Reynolds number range and the results are shown in Figure 5.48 (a) and (b). A small frequency shift of the maximum rates predicted by LST and by the experiments in the early stages (Fig. 5.48 (a)) is visible. This could be due to the slightly expanding flow in the test section or small angle of attack that would change the assumed edge Mach number. Relatively good agreement of maximum growth rates is found in the early stages of transition ($\sim 7.5\,\%$ discrepancy for $\mathrm{Re}_e = 1.19 \times 10^6$). With increasing Reynolds number, however, the discrepancy with LST predictions increases. The experiments produce larger growth rates and reach maximum values of $-\alpha_i \approx 40/\mathrm{m}$ for $\mathrm{Re}_e = 1.82\text{-}1.87 \times 10^6$ before the rates decay.

Conclusions. Instability waves in a flat plate hypersonic BL at M=6 are detected by means of several flush mounted pressure and heat-flux sensors of high frequency response. Simultaneous multiple local measurements of pressure and heat-flux fluctuation, although only captured on the surface and not in the BL, allow to detect the evolution of instability waves. Spectral analysis of the pressure and heat-flux sensor signals result in dominant frequencies, which correlate with unit Reynolds number and show unambiguously the existence of the second mode, the dominant instability in this Mach number range. A growth of fluctuation amplitudes could be determined for both kind of sensors and the amplification rates are compared with LST.

Dominant frequencies found in this lower range are not unit Reynolds number dependent and might have their origin in the oncoming free-flow of the test section or most likely in disturbances generated in the flow, passing the support structure on the lower side of the plate model.

An extensive analysis of the spectra, derived from the totality of all pressure and heat-flux measurements, shows that there might be a superposition of low frequency disturbances with the second-mode instability in the state close to transition.

An examination of the low-frequency disturbances and their origin seems recommendable eventually by means of a hot-wire mode analysis of the free-flow in the test section of the Ludwieg tube.

5.6 Investigation of Laser-Generated Flow Perturbations on a Flat Plate at M=6

The following experiments present results that attempt to produce discrete BL layer perturbations by means of optical laser excitation. An array of ALTP sensors is used to capture the progression of the excited perturbations in the hypersonic flat plate BL at M=6. The experimental results have a preliminary character and shall demonstrate the perspective of optical disturbance generation in combination with highly time and spatially resolved arrays of ALTP sensors.
The need for the generation of artificial, controlled disturbances is already mentioned in several previous sections. The propagation and growth of disturbance of known amplitude and frequency is of fundamental importance for stability investigations. Controlled experiments are very difficult to realize at super- and hypersonic speeds due to the high-frequency character (several 10 - 100 kHz) of the natural instability waves. Only one perturbance generator based on a controlled plasma discharge on the surface of a model can be found in literature [87]. Such a perturbator has several drawbacks, its location on the surface can not be changed easily, a surface roughness is created and only point-like disturbances can be created in a three-dimensional BL. In the following experiments, disturbances are created by a pulsed laser beam that can easily be adjusted from the outside of a test section to focus at locations in the BL and in free-stream above or upstream of the model. The preliminary results presented here are obtained in close cooperation with D. Heitmann from ISM in Braunschweig.

5.6.1 Experimental Setup

The experiments are carried out in the Hypersonic Ludwieg Tube Braunschweig (HLB) described in section 5.3.1. The flat plate model is identical to the one described in the previous section 5.5.1. Instead of single point sensors, the ALTP sensor array described in section 2.5 is installed in Insert 3 of the model shown in Figure 5.42. The linear array consists of 12 single ALTP films and is placed parallel to the flow direction at the symmetry line of the flat plate (y=0) resulting into a spatial resolution of 6 mm. The sensor array is located $\sim$282 mm downstream of the leading edge. Perpendicular to the array a single point ALTP sensor is placed at x=315 mm and y=16 mm to investigate wave propagation in spanwise direction.
The perturbation system consists of two Nd:YAG double pulse lasers. The optical system consisting of several lenses and mirrors focuses the laser beams through an optical access window above the flat plate into the test section. For the current investigation, a double

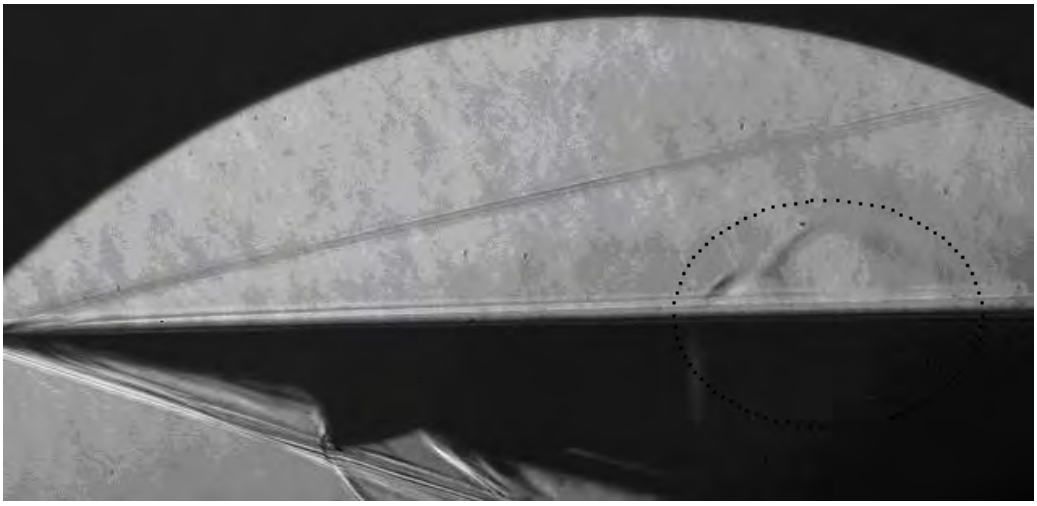

Figure 5.49: Schlieren picture of double pulse disturbance (pulse energy 75mJ/pulse, f=70 kHz); extent marked by dotted line (Heitmann et al. [51]).

pulsed disturbance is generated 40 mm upstream of the first sensor of the ALTP array. For qualitative visualization, Figure 5.49 shows a Schlieren picture of a strong double-pulse perturbation (pulse energy 75 mJ/pulse, f=70 kHz). In the actual experiments, more suitable weaker perturbations with a pulse energy of 8 mJ/pulse focussed on an area with a diameter of 2 mm and a frequency of f $\approx$ 100 KHz are used. For more information on the characteristics of the perturbation system and its specific characteristics, the reader is referred to [51]. More details on the instrumentation and data acquisition can be found in Section 5.3

5.6.2 Experimental Results

Figure 5.50 displays the time signals of three ALTPs with different spatial distance to the focussed double-pulse disturbance. The two pulses create an electric disturbance in the time signal of the ALTP at t=0 and 10 μs. The created perturbation reaches the first sensor several microseconds later at $\Delta x = 40$ mm (Fig. 5.50 (a)). Figure 5.50 (b) displays the evolution of the disturbance detected by the sensors at $\Delta x = 70$ mm and $\Delta x = 76$ mm downstream of the disturbance source. While, the disturbance at $\Delta x = 40$ mm seems to be composed of several wave numbers, a wave packet with a frequency of $\sim$ 100 kHz is formed at positions $\Delta x = 70$ and 76 mm further downstream. The amplitude of the wave packet grows in downstream direction. The time trace of ALTP 941 with a spanwise offset of 16 mm (Fig. 5.50 (c)) does not detect the wave packet. The lateral wave propagation angle of the perturbation is therefore smaller than $\arctan(16/73) \approx 12°$.
The disturbance frequency is selected to be located in the amplified frequency band of the

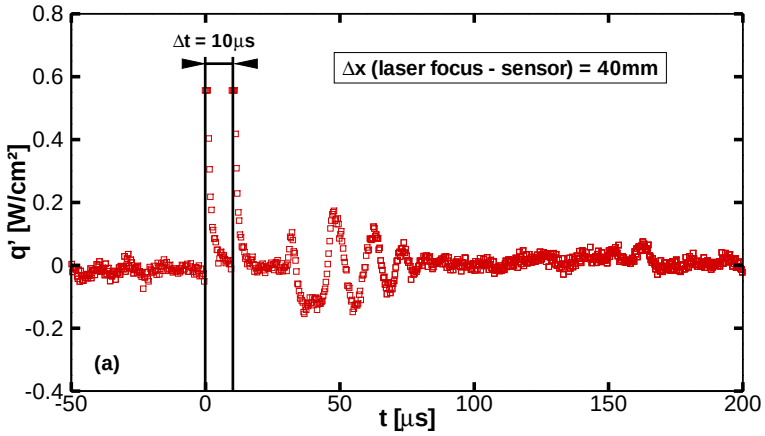

(a)

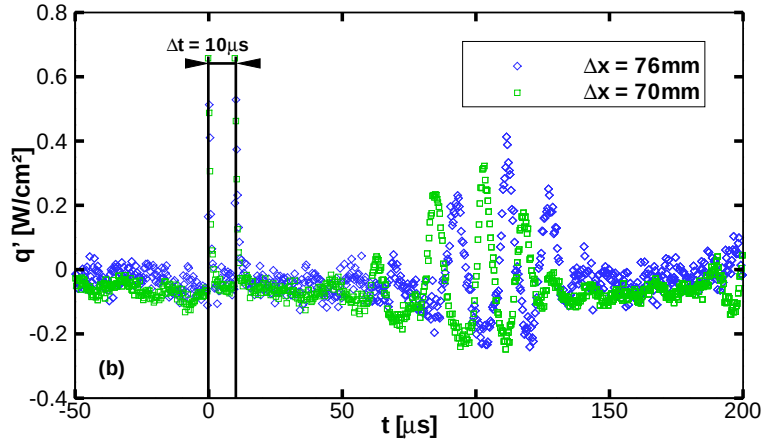

(b)

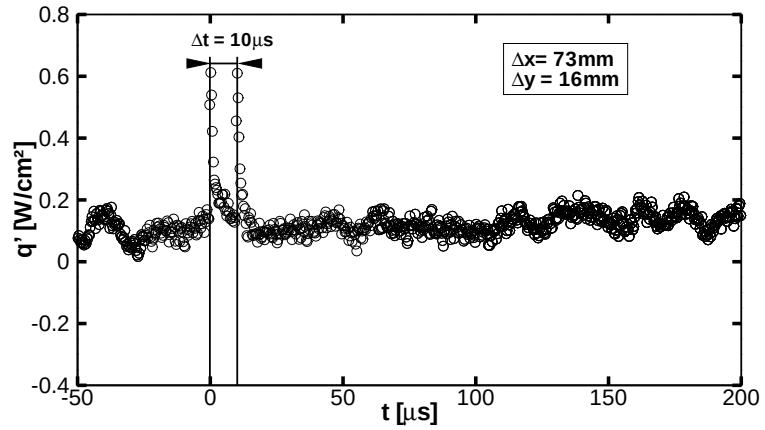

(c)

Figure 5.50: ALTP time signals showing the propagation of a perturbation created by a double pulse disturbance at a distance (laser focus - sensor) of (a) $\Delta x = 40$ mm (x=282 mm); $\Delta y = 0$ mm (b) $\Delta x = 70$ (x=312 mm) and 76 mm (x=318 mm); $\Delta y = 0$ mm and (c) $\Delta x = 73$ (x=315 mm); $\Delta y = 16$ mm.

second-mode instability predicted by LST and of the experiments at natural transition presented in the previous section. A good repeatability of the wave packets and its frequency is found. The results present the first artificially created second-mode wave packet created by means of optical disturbance generation.

6 Summary and Conclusions

The Atomic Layer Thermopile (ALTP) represents a new surface measurement technique that advances studies of heat-transfer processes especially in unsteady and short-duration flow environments. The device was employed over a broad range of flow conditions and its quality as flow diagnostics tool for the optimization of heat transfer problems has been demonstrated. The majority of the selected experiments help to shed light on the nature of physical phenomena in fluid flows and provide an improved insight with respect to important mechanisms present. The time-resolved heat-flux measurements benefit largely from its small time constant of less than $1\,\mu$s and significantly exceed the frequency range accessible by other heat-flux measurement techniques. The working principle of the ALTP is based on the transverse Seebeck effect. Hence, the ALTP belongs to a new class of heat transfer gauges that continues the idea of miniaturization in order to augment their frequency response. Single anisotropic crystals enable the realization of thin-film units with a thickness of some 10 to several 100 nanometers.

A sensor module was designed to incorporate the ALTP film and to provide proper thermal insulation of the substrate. The measurement chain was completed by miniature low-noise amplifiers. The custom-made amplifiers feature signal conditioning for the amplification of the mean value and the fluctuations separately in order to provide optimal signal amplification and quality. Based on the experiences with the single sensor modules, a linear sensor array composed of 12 single film sensors for distributed, highly time and spatially resolved surface heat-flux measurements was designed.

Specific sensor characteristics were studied by means of experimental techniques and theoretical modeling of the ALTP slab. Thermal modeling of the ALTP was carried out in cooperation with Dr. B. Smorodsky of ITAM. Typical thermal characteristics during a stationary and transient heat conduction process inside the sensor are considered. The results provide temperature distributions and allow a thermal analysis of typical time-scales that can lead to an influence on the temperature difference inside the ALTP.

A static calibration procedure based on the exposure of the ALTP to laser light radiation was developed. The laser calibration experiments show that the output signal of the ALTP is directly proportional to heat-flux density and has a linear characteristic from the $\mathrm{mW/cm^2}$ to the $\mathrm{kW/cm^2}$ range. The validity and accuracy of the procedure is confirmed

by comparative measurements with established heat transfer measurement techniques like transient thermal liquid crystals, thermocouples, thin-film and calorimetric gauges. Mainly stagnation-point heat-flux measurements in super- and hypersonic short-duration test facility were used to span the operational envelope of the ALTP. In the experiments, heat loads of more than $200\,\mathrm{W/cm^2}$ could be realized. Furthermore, tests in the plume of an electric thruster by means of a cooled stagnation-point probe show that the ALTP also operates in a partially or fully ionized plasma-flow environment.
A new dynamic calibration method based on radiative excitation by sinusoidally-modulated laser light was developed for ALTP sensors. Besides the amplitude-frequency characteristics, the procedure provides also the phase relation of specific ALTPs. The results show that the dynamic characteristics of the film are closely linked to the film thickness and suggest that a bandwidth extension of the ALTP should be possible by further reducing its thickness. Furthermore, the procedure grants access to the individual amplitude-frequency response characteristics of ALTPs. Hence, it allows the correction of amplitude spectra across the entire frequency range covered by the ALTP.
In addition, the dynamic properties of the ALTP were characterized by studying its response to a passing shock. The passing of a moving shock wave at a shock Mach number of 3.3 is resolved in an interval of $0.35\,\mu\mathrm{s}$. The successive convective heat-flux rise within less than $1\,\mu\mathrm{s}$ demonstrates that the ALTP gauge without protective coating has a frequency response of almost 1 MHz. Uncoated films have a hygroscopic character that leads to a decrease in sensitivity of the ALTP. A protective coating avoids such an effect, however increases the time constant of the ALTP at the same time. A systematic investigation of ALTPs with differently sized protective coatings was carried out. The thickness of the protective coating was optimized by monitoring its response to the passing shock wave. A coating with a thickness of $\sim$ 100 nanometers is found to be an optimal compromise between the two opposing requirements of a stable sensitivity of the ALTP and a high temporal resolution.

A major part of the current work demonstrates the capability of the new measurement technique and contributes to the understanding of several physical phenomena of fluid flows at the same time. A detailed summary of the specific results is found at the end of each experiment. A brief compilation of the major findings is given in the following:

The rotating flow of an internal ribbed channel (representing a cooling passage of a gas turbine blade) that impinges on a tip wall was investigated by point-wise ALTP sensors. The time-resolved heat flux measurements lead to a better understanding of the influence of fluctuations in temperature fields and heat-transfer mechanisms on the ther-

mally stressed wall. The measurements provide time-resolved heat transfer turbulence spectra that were previously not available for such internal cooling channels. In addition, the time-resolved measurements were corroborated with hot-film measurements near the wall to study the influence of unsteadiness in the velocity field at the wall on fluctuations in the heat flux. Turbulence intensities of the velocity and heat flux are both $\sim 20\%$. Length scales are approximated using the time signals of the hot film and the ALTP resulting into a turbulent integral length scale of $\sim 60\%$ of the channel width, while the heat flux integral length scale is found to be $\sim 35\%$ of the channel width. The ratio of integral length scales at the wall may be interpreted as turbulent Prandtl number and a value of $Pr_{turb} = \Lambda_f / \Lambda_q \approx 1.67$ was determined.

In the framework of the DFG Research program SPP 1167, the flow topology of an finite-length circular cylinder with an aspect ratio $\mathrm{H/D} = 2$ is chosen to study turbulent transport phenomena and the interaction of complex three-dimensional structures. Qualitative correlation of such processes with surface properties like distributions of heat-flux and pressure fluctuations were investigated. Static pressure measurements in a Reynolds number range between $\mathrm{Re}_D = 1 \times 10^5$ to 2.3×10^5 are used to identify major flow phenomena. A correlation of the maximum fluctuations with dominating flow features like the transition of the separated shear layer was found. The spectrum of the heat-flux fluctuations shows an increase of the intensity level in a frequency range up to 800 Hz at the transition location.

Highly time-resolved heat transfer measurements in the unsteady boundary layer behind an incident shock wave with a shock Mach number between $\mathrm{M}_s = 1.8$ to 3.3 were carried out by means of the ALTP. The existence of a laminar boundary was demonstrated for the first time in a unit Reynolds number range up to $11 \times 10^6/\mathrm{m}$. The time histories even resolve the progression of the fluctuation level superimposed on the mean heat flux of the laminar boundary layer. The observed transition scenarios seem to differ within the investigated unit Reynolds number regime of $0.5 \times 10^6/\mathrm{m} \leq \mathrm{Re}_{unit} \leq 11 \times 10^6/\mathrm{m}$. The results indicate two different transition mechanisms encountered in the unsteady boundary layer behind a moving shock wave.

Transition experiments on a 7-degree, half-angle, sharp cone were carried out in three different hypersonic facilities, the Mach-6-Quiet Tube (M6QT) of Purdue University (USA), the Hypersonic Ludwieg Tube (HLB) of Technische Universität Braunschweig (Germany) and the AT-303 of the Khristianovich Institute of Theoretical and Applied Mechanics in Novosibirsk (Russia).

The M6QT is currently the only facility worldwide that operates under quiet conditions at Mach number M=6. In the facility, the influence of acoustic noise radiated from turbulent nozzle walls was investigated. In a first step, the consecutive stages of transition under noisy flow were documented as reference. The dominant second mode was detected and its maximum growth rates are in very good agreement with those calculated by linear stability theory. A first harmonic of the second-mode instability was captured and even a weak residual of a second harmonic of the second mode was found. The amplification rates of the first harmonic exhibit similar growth rates like the one of the second mode during the early stages of boundary-layer transition. Under quiet flow, the amplitudes of the second-mode waves are very low. Therefore, the experimentally determined maximum growth rates were lower than the values predicted by linear stability theory. The results represent the first study of instability waves under quiet flow by measuring the fluctuations of wall heat flux on the cone surface.
Transition studies with the same pointed cone model used in the M6QT were carried out in the HLB. The HLB operates only under noisy flow and results allow a statement about the general comparability of transition studies in the two facilities at such conditions. Good agreement of amplification rates of the second mode and also in the range of the first harmonic was found. This indicates a similar transition scenario within the linear stage of boundary-layer transition in both facilities. A staggered array of fast-response ALTP and pressure gauges was used to capture fluctuation data of two different physical quantities. The spatial growth rates calculated from wall heat-flux and surface pressure fluctuation spectra agree well within the frequency range of the second-mode instability and its higher harmonic. A quantitative comparison shows that maximum growth rates measured by the pressure sensors are systematically slightly lower than the one detected by ALTPs.
In the AT-303, transition experiments on a cone were carried out at a free-stream Mach number of M=12. Stagnation temperatures of 900 to 1200 K and stagnation pressures between 90 and 520 bar approach conditions that can be considered as relevant for the experimental simulation of flight conditions of hypersonic vehicles. The comparison of the experimental results with linear stability theory exhibit good agreement in the frequency range of the dominant second mode. A third-mode instability was possibly detected in the current experiments for the first time. Agreement between theory and experiment was found for the amplification rates obtained from ALTP amplitude spectra. Furthermore, the amplification of the higher harmonic differs from the scenario that was observed in cone experiments in the lower hypersonic regime of M=6 of the HLB and M6QT.

Transition studies on a flat plate were carried out at M=6. Signals measured by a

staggered array of pressure and ALTP gauges indicate dominant disturbance in the boundary layer. Amplified waves packets in the frequency range typical for the second mode are detected. The comparison of the second-mode growth with linear stability theory exhibits good agreement at least for the linear stage. With increasing non-linear character, the discrepancy with the theoretical predictions increases and the experiments produce larger growth rates than predicted by linear stability theory. The maximum growth rate of the fundamental and first harmonic are similar. Analog results were observed on the cone at M=6 in the M6QT and HLB detected by both pressure and ALTP sensors. Such a behavior is unexplained and contradicts theoretical predictions of amplification rates of higher harmonics.
The generation of perturbations in the flat plate boundary layer at M=6 by means of optical laser excitation is presented. The experimental results demonstrate the perspective of optical disturbance generation in combination with highly time and spatially resolved arrays of ALTP sensors. Preliminary results show the first artificially created second-mode wave packet generated by means of optical disturbance excitation on the flat plate.

Outlook

The present work covers only a small fraction of heat-transfer phenomena, steady as well as unsteady, that can profit from the excellent characteristics of the ALTP. The current sensor design can easily be applied or adopted to other physical phenomenon of fluid flows that require time and spatially resolved surface information, e.g. study of shock dynamics, investigation of complex transition problems, combustion dynamics etc.
Future work in the context of improvements of the ALTP sensor development clearly lie in the miniaturization of the sensor module. A smaller module offers higher spatial resolution and less geometric and thermal surface distortion. Such a miniature module could even be used like a single stagnation probe and would not be restrained to surface measurements, similar to a pitot probe. Such a design would enable to obtain two-dimensional heat-flux information by traversing of flow field, e.g. in the wake of a turbine blade.
Furthermore, the working principle and characteristics of the ALTP imply a potential use for in-flight measurements to investigate aerothermodynamic phenomena and heat loads on thermal protection systems (Roediger et al. [120]). Several issues, however, have to be considered in the development of a suitable sensor system. Thermal stability is investigated and problems with initial preheating of the sensors are reported in [38], [41]. In short duration facilities, the substrate in combination with the aluminum of the cylinder acts as a perfect heat sink. Longer exposures to high heat loads or uncontrolled preheat-

ing of the sensors leads to unreliable quantitative mean heat-transfer rates. A proper and precise cooling system has to be designed for such purposes.
Within the fluid physical context, the transition studies using optical disturbance generation offer the perspective of controlled boundary-layer experiments at super- and hypersonic flow speeds. Future investigations of three-dimensional disturbance propagation on the flat plate and on a cone can be of great importance for stability investigations of super- and hypersonic boundary layers. Especially the use of three-dimensional sensor arrays can help to solve some questions that are raised in the current work, such as the growth and decay of the higher harmonic of the second-mode instabilities.
In addition, a continuation of the combined use of ALTPs and fast-response pressure sensors in other facilities simulating different noise levels and stagnation conditions in a kind of ring experiments could be very beneficial. Especially the *Stosswindkanal* of the Institute of Aerodynamics and Gas Dynamics can be used for transition studies in the supersonic flow regime. Such experiments could help to build a data base on the general comparability of transition experiments in different ground testing facilities and flight experiments.

Bibliography

[1] J.D. Anderson. *Modern compressible flow.* Mc Graw-Hill, 1990.

[2] R. L. Ash. Response characteristics of thin foil heat flux sensors. *J. Am. Inst. Aeronaut. Astronaut.*, Vol. 7, No. 12, pp. 2332-2335, 1969.

[3] J. R. Ashbridge. An interferometric study of shock tube boundary layers. Lehigh University Institute of Research Technical Report No. 14, 1959.

[4] M. Auweter-Kurtz, T. Gölz, H. Habiger, F. Hammer, H. Kurtz, M. Riehle, and C. Sleziona. High-power hydrogen arcjet thrusters. *Journal of Propulsion and Power*, Vol. 14, No. 5, pp. 764-773, 1998.

[5] D.E. Beasley and R.A. Figliola. Analysis of a local heat transfer probe. *Journal of Heat Transfer*, Vol. 2, pp. 467-472, 1986.

[6] D. Bergmann. *Experimentelle Ermittlung der instationären aerodynamischen Eigenschaften von Brückenprofilen im Wasserkanal.* Dissertation, Universität Stuttgart, Fak. Luft- und Raumfahrttechnik, 2004.

[7] S. V. Bobashev, N. P. Mende, P.A. Popov, B.I. Reznikov, V. A. Sakharov, S.Z. Sapozhnikov, V.Yu. Mityakov, A.V. Mityakov, T. Roediger, H. Knauss, and D. Bountin. Application of anisotropic heat sensors in aerodynamic investigations. *Journal of Thermophysics, St. Petersburg*, 2009. *(accepted, to be published).*

[8] S. V. Bobashev, N. P. Mende, V. A. Sakharov, S.Z. Sapozhnikov, V.Yu. Mityakov, A.V. Mityakov, and D. v. Wie. Application of gradient heat flux sensor in shock tube experiments. AIAA Paper 2005-787, 43rd AIAA Aerospace Sciences Meeting and Exhibit, Reno, 2005.

[9] H. Böhrk and M. Auweter-Kurtz. TIHTUS thrust measurement with a baffle plate. AIAA-2007-5297, 43rd Joint Propulsion Conference and Exhibit, Cincinnati, OH, 2007.

[10] H. Böhrk and M. Auweter-Kurtz. Velocity and total pressure measurement in the two-stage hybrid thruster TIHTUS. Proc. European Conference For Aerospace Sciences, Vol. 22, No. 2, 2007.

[11] H. Böhrk and M. Auweter-Kurtz. Efficiency analysis of the two-stage thruster TIHTUS. *AIAA Journal of Thermophysics and Heat Transfer*, Vol. 22, No. 2, pp. 309-312, 2008.

[12] H. Böhrk, T. Rödiger, and M. Auweter-Kurtz. Heat flux measurement in the two-stage hybrid electric thruster TIHTUS. *AIAA Journal of Thermophysics and Heat Transfer*, Vol. 23, No. 4, pp. 404-407, 2009.

[13] M.I. Boulas and D.C.T. Pei. Dynamics of heat transfear from cylinder in a turbulent air stream. *Int. Journal of Heat Mass Transfer*, Vol. 107, pp. 767-783, 1974.

[14] R. Brun. Comment on "further experiments on shock-tube wall boundary-layer transition". *AIAA J.*, Vol. 23, No. 8, pp. 1297-1299, 1985.

[15] J.A. Campbell and T.J. Hanratty. Mechanism of turbulent mass transfer at a solid boundary layer. *American Institute of Chemical Engineers J.*, Vol. 29, No. 2, pp. 221-229, 1983.

[16] C. Carcasci and F. Facchini. Comparison between two gas turbine solutions to increase combined power plant efficiency. *Journal of Energy Conversion and Management*, Vol. 41, No. 8, pp. 757-773, 2000.

[17] H.S. Carslaw and J.C. Jaeger. *Conduction of Heat in Solids*. Oxford University Press, 2nd edition, 1959.

[18] M. J. Chaney and W. J. Cook. Further experiments on shock tube wall boundary-layer transition. *AIAA J.*, Vol. 21, No. 7, pp. 1046-1048, 1983.

[19] P.R.N. Childs, J.R. Greenwood, and C.A. Long. Heat flux measurement techniques. *Proc. Institution of Mechanical Engineers, Part C: Journal of Mechanical Engineering Science*, Vol. 213, No. 7, pp. 655-677, 1999.

[20] W.J. Cook and F.J. Feldermann. Reduction of data from thin film heat transfer gauges, a concise numerical technique. *AIAA J.*, Vol. 4, No. 3, p. 561, 1996.

[21] W.R Davies and L. Bernstein. Heat transfer and transition to turbulence in the shock-induced boundary layer on a semi-infinite flat plate. *Journal of Fluid Mechanics*, Vol. 36, No. 1, pp. 87-112, 1969.

[22] A. Demetriades. Hypersonic viscous flow over a slender cone, Part III: Laminar instability and transition. AIAA-1974-535, 1974.

[23] T.E. Diller. Advances in heat transfer. *Academic Press, New York*, Vol. 23, pp. 279-353, 1993.

[24] T.E. Diller. Methods of determing heat flux from temperature measurements. *Proc. 42nd International Instrumentation Symposium*, 1996.

[25] T.E. Diller and D.P. Telionis. Time resolved heat transfer and skin friction measurements in unsteady flow. *Advances in Fluid Mechanics Measurements. Lecture Notes in Engineering*, 1989.

[26] R.E. Dillon and H.T. Nagamatsut. Heat transfer and transition mechanism on a shock-tube wall. *AIAA J.*, Vol. 22, No. 11, pp. 1524-1528, 1984.

[27] M.G. Dunn. Convective heat transfer and aerodynamics in axial flow turbines. *ASME Journal of Turbomachinery*, Vol. 123, pp. 637-686, 2001.

[28] E.R.G. Eckert and R. J. Goldstein. Measurement techniques in heat transfer. 1970.

[29] H.U. Eckert. The induction arc: A state-of-the-art review. *Journal of High Temperature Science*, Vol. 6, pp. 99-134., 1973.

[30] A.H. Epstein, G.R. Guenette, R.G. Nortin, and C. Yuzhang. High frequency response heat flux gauges. *Review Scientific Instruments*, Vol. 57, pp. 639-649, 1986.

[31] M. Estorf, S.P. Schneider, H.B. Johnson, and S. Hein. Surface-pressure measurements of second-mode instability in quiet hypersonic flow. AIAA-2008-1153, 46th AIAA Aerospace Sciences Meeting and Exhibit, Reno, 2008.

[32] M. Estorf, T. Wolf, and R. Radespiel. Experimental and numerical investigations on the operation of the Hypersonic Ludwieg Tube Braunschweig. Proc. 5th European Symposium on Aerothermodynamics for Space Vehicles, 2004.

[33] J.A. Fay and F.R. Riddell. Theory of stagnation point heat transfer in dissociated air. *J. Aeronaut. Sci.*, Vol. 25, pp. 73-85, 1958.

[34] T.J. Fitzgerald, N.M. Catipovis, and G.N. Javanovic. Instrumented cylinder for studying heat transfer to immersed tibes in fluidized beds. *Ind. Eng. Chem. Fundamental*, Vol. 20, No. 1, pp. 82-88, 1981.

[35] S.A. Gaponov and A.A. Maslov. Development of disturbances in compressible flows. *Science, Novosibirsk*, 1980. *(in Russian).*

[36] R. Gardon. An instrumentation for the direct measurement of intense thermal radiation. *Review Scientific Instruments*, Vol. 24, pp. 360-370, 1953.

[37] R. Gardon. A transducer for the measurement of heat-flow rate. *Journal of Heat Transfer*, Vol. 82, pp. 396-398, 1960.

[38] S. Geisbauer. Untersuchung der Temperaturabhängigkeit des ALTS-Wärmeflusssensors. *Studienarbeit, Institute of Aerodynamics and Gas Dynamics, Universität Stuttgart*, 2007. *(in German).*

[39] E. J. Gion. Measured velocity profiles in the laminar boundary layer behind a shock. *Physics of Fluids*, Vol. 8, No. 3, pp. 546-547, 1965.

[40] R.J. Goldstein and H.H. Cho. A review of mass transfer measurements using naphtalene sublimation. *Experimental Thermal and Fluid Science*, Vol. 10, No. 4, pp. 416-434, 1995.

[41] F. Grygier. Wärmeübergangsmessungen an Prallstrahlen mit einem ALTP Heat Flux Sensor. *Studienarbeit, Institute of Aerospace Thermodynamics, Universität Stuttgart*, 2009. *(in German).*

[42] J.M. Hager, L.W. Langley, S. Onishi, and T.E. Diller. Microsensors for high heat flux measurements. *AIAA Journal of Thermophysics and Heat Transfer*, Vol. 7, No. 3, pp. 531-534, 1992.

[43] J.M. Hager, S. Onishi, L.W. Langley, and T.E. Diller. Heat flux micro sensors. *ASME Heat Transfer Measurements, Analysis and Flow Visualisation*, 1989.

[44] J.M. Hager, S. Simmons, D. Smith, S. Onishi, L.W. Langley, and T.E. Diller. Experimental performance of a heat flux micro sensor. *Journal of Engineering for Gas Turbines and Power*, Vol. 113, pp. 246-250, 1991.

[45] J.M. Hager, S. Simmons, D. Smith, S. Onishi, L.W. Langley, and T.E. Diller. High temperature heat flux measurements. *AIAA Journal of Thermophysics and Heat Transfer*, Vol. 7, pp. 531-534, 1993.

[46] N.E. Jr. Hager. Thin foil heat meter. *Review Scientific Instruments*, Vol. 36, pp. 1564-1570, 1965.

[47] C.W. Haldeman and M.G. Dunn. Heat-transfer measurements and predictions for the vane and blade of a rotating high-pressure turbine stage. *Journal of Turbomachinery*, Vol. 126, pp. 101-109, 2004.

[48] Millman D.R. Hamilton II, H.H. and R.B. Greendyke. Finite-difference solution for laminar or turbulent boundary layer flow over axisymmetric bodies with ideal gas, CF4, or equilibrium air chemistry. NASA TP-3271, 1992.

[49] R.A. Hartunian, A.L. Russo, and P.V. Marrone. Boundary-layer transition and heat transfer in shock tubes. *Journal of Aeronautical Science*, Vol. 27, pp. 587-594, 1960.

[50] M. Hayashi, A. Sakurai, and S. Aso. Measurement of heat transfer coefficients in shock wave-turbulent boundary layer interaction regions with a multi-layered thin film heat transfer gauge. NASA TM-77958, 1986.

[51] D. Heitmann, C. J. Kähler, and R. Radespiel. Investigation of laser-generated flow perturbations in hypersonic flow over a flat plate. AIAA-2008-3737, Proc. 38th Fluid Dynamics Conference and Exhibit, Seattle, 2008.

[52] D. Heitmann, T. Roediger, C. Kaehler, H. Knauss, R. Radespiel, and E. Kraemer. Disturbance-level and roughness-induced transition measurements in a conical boundary layer at Mach 6. AIAA-2008-3951, 26th AIAA Aerodynamic Measurement Technology and Ground Testing Conference, Seattle, 2008.

[53] K. Hencky. Untersuchungen zur Isolation von Kühlräumen (investigation of insulation in cold-stores). *Zeitschrift für die Gesamte Kälte-Industrie (Journal for the Cold Storage Industry), Munich*, Vol. 22, No. 8, pp. 79-84, 1915.

[54] G. Herdrich. *Aufbau, Qualifikation und Charakterisierung einer induktiv beheizten Plasmawindkanalanlage zur Simulation atmosphärischer Eintrittsmanöver*. Dissertation, Universität Stuttgart, Fak. Luft- und Raumfahrttechnik, 2004.

[55] J.O. Hinze. *Turbulence*. Mc Graw-Hill, 2nd edition, 1976.

[56] D.G. Holmberg and T.E. Diller. High frequency heat flux sensor calibration and modeling. *Journal of Fluids Engineering*, Vol. 117, pp. 661-664, 1995.

[57] D.G. Holmberg and T.E. Diller. Simultaneous heat flux and velocity measurements in transonic turbine cascade. *ASME Journal of Turbomachinery*, Vol. 127, pp. 502-506, 2005.

[58] D.G. Holmberg, Y.S. Mukkamala, and T.E. Diller. Shock tunnel evaluation of heat flux sensors. AIAA-1994-0730, 32nd AIAA Aerospace Sciences Meeting and Exhibit, Reno, NV, 1994.

[59] V. Iliopoulou, R. Denos, N. Billiard, and T. Arts. Time-averaged and time-resolved heat flux measurements on a turbine stator blade using two-layered thin-film gauges. *ASME Journal of Turbomachinery*, Vol. 126, pp. 570-577, 2004.

[60] P. T. Ireland and T. V. Jones. The measurement of local heat transfer coefficients in blade cooling geometrics. *Heat Transfer and Cooling in Gas Turbines, AGARD*, CP390, pp. 28-1-28-8, 1985.

[61] P. T. Ireland and T. V. Jones. Detailed measurements of heat transfer on and around a pedestal in fully developed flow. *Proc. 8th International Heat Transfer Conference*, Vol. 3, pp. 975-980, 1986.

[62] S. Jenkins, T. Roediger, J. v. Wolfersdorf, B. Weigand, H. Knauss, and K. Kraemer. Time-resolved heat transfer measurements on the tip wall of a ribbed channel using a novel heat flux sensor - Part II: heat transfer results. *ASME Journal of Turbomachinery*, Vol. 130, No. 1, pp. 011019/1-9, 2008.

[63] S. Jordan. Experimentelle Untersuchungen zur Charakterisierung des Leistungsverhaltens von Airbag-Gasgeneratoren. *Studienarbeit, Institute of Aerodynamics and Gas Dynamics, Universität Stuttgart*, 2008. *(in German).*

[64] T. Juliano, E. Swanson, and S. P. Schneider. Transition research and improved performance in the Boeing/AFOSR Mach-6 quiet tunnel. *AIAA J.*, Vol. 46, No. 7, pp. 1757-1763, 2008.

[65] W. M. Kays, M. E. Crawford, and B. Weigand. *Convective Heat and Mass Transfer.* Mc Graw-Hill, New York, 4th edition, 2005.

[66] J.M. Kendall. Wind tunnel experiments relating to supersonic and hypersonic boundary-layer transition. *AIAA J.*, Vol. 13, No. 3, pp. 290-299, 1975.

[67] A. Kharitonov, V. Zvegintsev, Chirkashenko V., and L. Vasenev. Commissioning and acceptance testing of the new hypersonic wind tunnel at ITAM RAS. AIAA-2005-3328, AIAA/CIRA 13th International Space Planes and Hypersonics Systems and Technologies Conference, 2005.

[68] C. T. Kidd and C. G. Nelson. How the Schmidt-Boelter gage really works. *Proc. 41st Int. Instrum. Symp.*, pp. 347-368, 1995.

[69] H. Knauss, U. Gaisbauer, S. Wagner, D. Buntin, A. Maslov, B. Smorodsky, and J. Betz. Calibration experiments of a new active fast response heat flux sensor to measure total temperature fluctuations. Part I-III. *Proc. International Conference on Methods of Aerophysical Research*, 2002.

[70] H. Knauss, R. Riedel, and S. Wagner. The Shock Wind Tunnel of Stuttgart University - A facility for testing hypersonic vehicles. AIAA-1999-4959, 9th AIAA International Space Planes and Hypersonic Systems and Technologies Conference, Norfolk, VA, 1999.

[71] H. Knauss, T. Roediger, D.A. Bountin, B.V. Smorodsky, J. Srulijes, F. Seiler, A.A. Maslov, U. Gaisbauer, and E. Kraemer. A novel sensor for fast heat flux measurements. AIAA-2006-3637, 25th AIAA Aerodynamic Measurement Technology and Ground Testing Conference, San Francisco, 2006.

[72] J.S. Kraabel, J.W. Baughn, and A.A. McKillop. An instrumentation for the measurement of the heat flux from a surface with uniformed temperature. *Journal of Heat Transfer*, Vol. 102, pp. 576-578, 1980.

[73] C. H. Kuo and A. K. Kulkarni. Analysis of heat flux measurement by circular foil gages in a mixed convection/radiation environment. *Journal of Heat Transfer*, Vol. 113, pp. 1037-1040, 1991.

[74] A. Kyarad and H. Lengfellner. Thermoelectric and photovoltaic effects in Al-Si multilayers. Proc. 4th European Conference on Thermoelectrics, 2006.

[75] D. Lee, R. Greif, S. J. Lee, and J. H. Lee. Heat transfer from a flat plate to a fully developed axisymmetric impinging jet. *Journal of Heat Transfer*, Vol. 117, pp. 772-775, 1995.

[76] H. Lengfellner, G. Kremb, A. Schnellbögl, J. Betz, K.F. Renk, and W. Prettl. Giant voltages upon surface heating in normal YBCO films suggesting an Atomic Layer Thermopile. *Apl. Phys. Letters*, Vol. 60, No. 4, pp. 501-503, 1992.

[77] H. Lengfellner, S. Zeuner, W. Prettl, and K.F. Renk. Thermoelectric effect in normal-state YBCO films. *Europhys. Letter*, Vol. 25, No. 5, pp. 375-378, 1994.

[78] Trimmer L.L. Study of the blunt-body stagnation point velocity gradient in hypersonic flow. AEDC TR-68-99, 1999.

[79] S. Löhle. *Untersuchung von Wiedereintrittsplasmen mit Hilfe laserinduzierter Fluoreszenzmessungen.* Dissertation, Universität Stuttgart, Fak. Luft- und Raumfahrttechnik, 2006.

[80] J. L. Lumley. Similarity and the turbulent energy spectrum. *Phys. Fluids*, Vol. 10, No. 4, pp. 855-858, 1967.

[81] P.R.A. Lyons and S.L. Gai. A method for the accurate determination of the thermal product ($\rho c_p k$) for thin film heat transfer or surface thermocouple gauges. *Journal of Physical Engineering*, Vol. 21, pp. 445-448, 1988.

[82] L.M. Mack. Boundary-layer linear stability theory. Special course on stability and transition of laminar flow advisory group for aerospace research and development. AGARDograph No. 709, 1984.

[83] H. Mark and Jr. Mirtich, M. J. Transition in shock-tube boundary layers. *Physics of Fluids*, Vol. 5, No. 2, pp. 251-253, 1962.

[84] R. C. Martinelli, E. H. Morrin, and L. M. K. Boelter. An investigation of aircraft heaters, V-theory and use of heat meters for the measurement of rates of heat transfer which are independent of time. *NACA Report*, 1942.

[85] J.G. Marvin and R.B. Pope. Laminar convective heating and ablation in the mars atmosphere. *AIAA J.*, Vol. 5, No. 2, pp. 240-248, 1968.

[86] A. A. Maslov, A. N. Shiplyuk, A. A. Sidorenko, and D. Arnal. Leading-edge receptivity of a hypersonic boundary layer on a flat plate. *Journal of Fluid Mechanics*, Vol. 426, pp. 73-94, 2001.

[87] A.A. Maslov, A.D. Kosinov, and S.G. Shevelkov. Experiments on the stability of supersonic laminar boundary layers. *Journal of Fluid Mechanics*, Vol. 219, pp. 621-633, 1990.

[88] D.J. Mee. Boundary-layer transition measurements in hypervelocity flows in a shock tunnel. *AIAA J.*, Vol. 40, No. 8, pp. 1542-1548, 2002.

[89] D.J. Mee and C.P. Goyne. Turbulent spots in boundary layers in a free piston shock tunnel flow. *Shock Waves*, Vol. 6, No. 6, pp. 337-343, 1996.

[90] H. Mirels. Laminar boundary layer behind shock advancing into stationary fluid. NACA TN-3401, 1955.

[91] H. Mirels. Laminar boundary layer behind a strong shock moving into air. NASA TN-D 291, 1961.

[92] H. Mirels. Shock tube test time limitation due to turbulent-wall boundary layer. *AIAA J.*, Vol. 2, No. 1, pp. 84-93, 1964.

[93] H. Mirels. Turbulent boundary layer behind constant velocity shock including wall blowing effects. *AIAA J.*, Vol. 22, No. 8, pp. 1042-1047, 1983.

[94] A.V. Mityakov, V.Yu. Mityakov, S.Z. Sapozhnikov, and Yu. S. Chumakov. Application of the transverse Seebeck effect to measurement of instantaneous values of a heat flux on a vertical heated surface under condition of free-convection heat transfer. *High Temperature*, Vol. 40, No. 4, pp. 620-625, 2002.

[95] R. J. Moffat, J. K. Eaton, and D. Mukerji. A general method for calculating the heat island correction and uncertainties for button gauges. *Meas. Sci. Technol.*, Vol. 11, pp. 920-932, 1958.

[96] M.V. Morkovin. Fluctuations and hot wire anemometry in compressible flows. AGARDograph No. 24, 1956.

[97] D. Neumann. Aerothermodynamic instrumentation. *AGARD, Special Course on Aerothermodynamics of Hypersonic Vehicles*, 1989.

[98] H. Oertel. *Stossrohre*. Springer, Wien, 1966.

[99] M.L.G. Oldfield, H.J. Bird, and M.G. Doe. Design of wide-bandwith analogue circuits for heat transfer instrumentation in transient tunnels. Heat and Mass Transfer in Rotating Machinery: Proc. 16th Symposium of the International Center for Heat and Mass Transfer, pp. 232-258, 1984.

[100] M.L.G. Oldfield, T.V. Jones, and D.L. Schultz. Online computer for transient turbine cascade instrumentation. *IEEE Trans. Aerospace and Electronic Systems*, Vol. 14, No. 5, pp. 738-749, 1978.

[101] H. Olivier. An improved method to determine free stream conditions in hypersonic facilities. *Shock Waves*, Vol. 3, pp. 129-139, 1993.

[102] H. Olivier. Thin film gauges and coaxial thermocouples for measuring transient temperatures. *Documentation, Shock Wave Laboratory Aachen, Germany*, 2003.

[103] D. J. Ortolano and F. F. Hines. A simplified approach to heat flow measurement. *Advances in Instrumentation, Part II, Research Triangle Park: ISA*, Vol. 38, pp. 1449-1456, 1983.

[104] R.J. Pattenden, S.R. Turnock, and X. Zhang. Measurements of the flow over a low-aspect- ratio cylinder mounted on a ground plane. *Exp. Fluids.*, Vol. 39, pp. 10-21, 2005.

[105] O.M. Philips. Turbulence in supersonic flow. *Journal of Aeronautical Sciences*, Vol. 20, No. 10, pp. 657-682, 1953.

[106] O.M. Philips. On the generation of sound by a supersonic turbulent shear layer. *Journal of Fluid Mechanics*, Vol. 9, pp. 1-28, 1960.

[107] PCB Piezotronics. Pressure and force sensors division, pressure catalog. Avail. at: http://www.pcb.com/Linked Documents/Pressure/PFScat.pdf. Cited Aug. 19, 2007.

[108] Murtfeldt Plastics. MURPEC technical data. Avail. at: http://www.murtfeldt.de/en/werkstoffe/direktwahl/murpec_murpec-sp/technische_daten/. Cited Jan. 20, 2009.

[109] S.B. Pope. *Turbulent Flows*. Cambridge University Press, New York, 2000.

[110] A.R. Porro, T.G. Jr. Keith, and W.R. Hingst. A laser-induced heat flux technique for convective heat transfer measurements in high speed flows. *ICIASF Record, International Congress on Instrumentation in Aerospace Simulation Facilities*, pp. 146-155, 1991.

[111] Praezisions Glas&Optik GmbH. MACOR Machinable Glass Ceramic MGC technical data. Avail. at: http://www.pgo-online.com/intl/katalog/macor_machinable_glass_ceramic.html. Cited Jan. 20, 2009.

[112] S. Raphael-Mabel. Design and calibration of a novel high temperature heat flux sensor. Master thesis, Virginia Polytechnic Institute and State University, 2005.

[113] K.F. Renk, J. Betz, S. Zeuner, H. Lengfellner, and W. Prettl. Thermopile effect due to laser radiation heating in thin films of high-Tc materials. *Physica C*, Vol. 235-240, pp. 37-40, 1994.

[114] W. C. Reynolds, W. M. Kays, and S. J. Kline. Heat transfer in the turbulent incompressible boundary layer.II step wall temperature distribution. NASA TM-12-2-58W, 1958.

[115] A.S. Jr. Roberts, K.R. Ortgies, E. Gartenberg, and D.L. Carraway. Convective response of a wall-mounted hot film sensor in a shock tube. Proc. International Symposium on Non-Steady Fluid Dynamics, 1990.

[116] T. Roediger, S. Jenkins, H. Knauss, J. v. Wolfersdorf, U. Gaisbauer, and E. Kraemer. Time-resolved heat transfer measurements on the tip wall of a ribbed channel using a novel heat flux sensor - Part I: sensor and benchmarks. *Journal of Turbomachinery*, Vol. 130, No. 1, pp. 011018/1-8, 2008.

[117] T. Roediger, H. Knauss, D.A. Bountin, B.V. Smorodsky, A.A. Maslov, R. Heitmann, D. Radespiel, and E. Kraemer. Hypersonic instability waves measured on a flat plate at Mach 6. Proc. International Conference on Methods of Aerophysical Research, Novosibirsk, 2008.

[118] T. Roediger, H. Knauss, M. Estorf, S.P. Schneider, B.V. Smorodsky, and E. Kraemer. Hypersonic instability waves measured using fast-response heat-flux gauges. AIAA Paper 2008-0638, 46th AIAA Aerospace Sciences Meeting and Exhibit, Reno, 2008.

[119] T. Roediger, H. Knauss, U. Gaisbauer, S. Wagner, and E. Kraemer. Pressure and heat flux measurements on the surface of a low-aspect-ratio circular cylinder mounted on a ground plate. *Numerical Fluid Mechanics and Multi Disciplinary Design (NNFM) in the Springer series: New Results in Numerical and Experimental Fluid Mechanics*, Vol. 96, pp. 121-128, 2007.

[120] T. Roediger, H. Knauss, and E. Kraemer. A novel fast-response heat flux sensors for fundamental research in the field of future space transportation systems. IAC-07-E2.2.07, Proc. 58th International Aeronautical Congress, Hyderabad, India, 2007.

[121] T. Roediger, H. Knauss, B.V. Smorodsky, V.F. Chirkashenko, V.I. Zvegintsev, D.A. Bountin, A.A. Maslov, S. Wagner, and E. Kraemer. The Atomic Layer Thermopile - a fast heat flux sensor for measuring high heat loads in short duration hypersonic ground testing facilities. Proc. International Conference on Methods of Aerophysical Research, Novosibirsk, 2007.

[122] T. Roediger, H. Knauss, J. Srulijes, F. Seiler, and E. Kraemer. A novel fast-response heat-flux sensor for measuring transition to turbulence in the boundary layer behind a moving shock wave. Proc. 26th International Symposium on Shock Waves, Göttingen, 2007.

[123] S.C. Roh and S.O. Park. Vortical flow over the free end surface of a finite circular cylinder mounted on a flat plate. *Exp. Fluids.*, Vol. 34, pp. 63-67, 2003.

[124] T. R. Salyer, S. H. Collicott, and S. P. Schneider. Feedback stabilized laser differential interferometry for supersonic blunt body receptivity experiments. AIAA-2000-416, 38th Aerospace Sciences Meeting and Exhibit, Reno, 2000.

[125] S.Z. Sapozhnikov, V.Yu. Mityakov, A.V. Mityakov, R.L. Petrov, V.V. Grigor'ev, S.V. Bobashev, N.P. Mende, and V.A. Sakharov. Heat flux measurements on the inner walls of a shock tube. *Technical Physics Letters*, Vol. 30, No. 1, pp. 76-77, 2004.

[126] H. Schlichting. *Grenzschichttheorie*. Verlag G. Braun, Karlsruhe, 1982.

[127] S. P. Schneider. Hypersonic laminar- turbulent transition on circular cones and scramjet forbodies. *Progress in Aerospace Sciences*, Vol. 40, pp. 1-50, 2004.

[128] S. P. Schneider. The development of hypersonic quiet tunnels. *Journal of Spacecraft and Rockets*, Vol. 45, No. 4, pp. 641-664, 2007.

[129] S. P. Schneider. Effects of roughness on hypersonic boundary-layer transition. *Journal of Spacecraft and Rockets*, Vol. 45, No. 3, pp. 323-333, 2008.

[130] S. P. Schneider. Laminar-turbulent transition. *Lecture notes from A&AE 624/690T*, 2008.

[131] D.L. Schultz and T.V. Jones. Heat transfer measurement in short duration hypersonic facilities. *AGARDograph*, 165, 1973.

[132] E.C. Shewan, K.G.T. Hollands, and G.D. Raithby. The measurement of surface heat flux using the peltier effect. *Journal of Heat Transfer*, Vol. 111, No. 3, pp. 798-803, 1989.

[133] A. Smeets, G.; George. Investigation of shock boundary layers with a laser interferometer. Proc. 9th International Shock Tube Symposium, 1973.

[134] W.E. Smith, H.S. Glick, A. Hertzberg, and W. Squire. Schlieren studies of the flow field behind strong shocks. Meeting of the Division of Fluid Mechanics, American Physical Society, 1954.

[135] B.V. Smorodsky. Theoretical analysis of the heat conduction in the ALTP sensor. *Internal Report, DFG-RFBR Research Corporation Report, Institut of Aeordynamics and Gas Dynamics*, 2005.

[136] D. A. Spence and B. A. Woods. A review of theoretical treatments of shock-tube attenuation. *Journal of Fluid Mechanics*, Vol. 19, pp. 161-174, 1964.

[137] J. Srulijes and F. Seiler. Analytically obtained data compared with shock tunnel heat flux measurements at a conical body at M=6. *Numerical Fluid Mechanics and Multi Disciplinary Design (NNFM) in the Springer series: New Results in Numerical and Experimental Fluid Mechanics*, Vol. 92, pp. 184-191, 2006.

[138] P.C. Stainback and R.D. Wagner. A comparison of disturbance levels measured in hypersonic tunnels using a hot wire anemometer and a pitot pressure probe. AIAA-1972-1003, 7th AIAA Aerodynamic Testing Conference, Palo Alto, 1972.

[139] S. Stefanescu, R. G. DeAnna, and M. Mehregany. Experimental performance of a micromachined heat flux sensor. NASA TM-107517, 1998.

[140] K.E. Stetson and R.L. Kimmel. On hypersonic boundary-layer stability. AIAA-1992-0737, 30th Aerospace Sciences Meeting and Exhibit, Reno, NV, 1992.

[141] K.E. Stetson, R.L. Kimmel, E.R. Thompson, J. C. Donaldson, and L.G. Siler. A comparison of planar and conical boundary layer stability and transition at a Mach number of 8. AIAA-1991-1639, 22nd Fluid Dynamics, Plasma Dynamics and Lasers Conference, Honolulu, HI, 1991.

[142] E. Suarez, R.S. Figliola, and D.R. Pitts. Instantaneous azimuthal heat transfer coefficients from horizontal cylinder to a mixed particle size air-fluidized bed. ASME Paper No. 83-HT-93, 1983.

[143] W. P. Thompson and R. J. Emrich. Turbulent spots and wall roughness effects in shock tube boundary layer transition. *Physics of Fluids*, Vol. 10, No. 1, pp. 17-20, 1967.

[144] United Nations Environment Programme, Division of Environmental Law and Conventions. UNEP handbook for drafting laws on energy efficiency and renewable energy resources. ISBN: 978-92-807-2810-1, 2007. Avail. at: http://www.earthprint.com. Cited Feb. 10, 2009.

[145] D.A. Walker and M.D. Walker. Method for fast sine-wave calibration of hot-wire frequency response. *Review Scientific Instruments*, Vol. 61, No. 3, p. 1131, 1990.

[146] R.C. Weatherstone, A.L. Russo, W.E. Smith, and P.V. Marrone. Gasdynamics of a wave superheater facility for hypersonic research & development. AFOSR TN 59-107, 1959.

[147] J. Weiss, H. Knauss, and S. Wagner. Experimental determination of free stream disturbance field in a short duration supersonic wind tunnel. *Exp. Fluids*, Vol. 35, pp. 291-302, 2003.

[148] V. Wendt, H.P. Kreplin, G. Hoehler, F.R. Grosche, P. Krogmann, and M. Simen. Planar and conical boundary layer stability experiments at Mach 5. AIAA-1993-5112, 5th International Aerospace Planes and Hypersonics Technologies Conference, Munich, 1993.

[149] F.M. White. *Viscous Fluid Flow.* Mc Graw-Hill, 2nd edition, 1991.

[150] A. Wolter, A. Leder, A. Berns, and E. Obermeier. Einsatz mikroelektromechanischer Drucksensoren (MEMS) in Kombination mit laseroptischen Messverfahren in der experimentellen Strömungsmechanik. Proc. Lasermethoden in der Strömungsmesstechnik, GALA e.V. , pp. 30.1-30.8., 2006. *(in German).*

[151] H. Yasuoka, H. Mazaki, T. Terashima, and B. Yoshichika. Optical absorption spectra of single-crystal $YBa_2Cu_3O_y$ films. *Physica C*, Vol. 175, pp. 192-196, 1991.

[152] T.H. Zahner, R. Förg, and H. Lengfellner. Transverse thermoelectric response of a tilted metallic multi layer structure. *Applied Phys. Letters*, Vol. 73, No. 10, pp. 1364-1366, 1998.

[153] S. Zeuner. Atonlagenthermosäulen in Hochtemperatur-Supraleitern als schnelle Strahlungsdetektoren. *Dissertation, Universität Regensburg*, 1994. *(in German).*

[154] S. Zeuner, H. Lengfellner, and W. Prettl. Thermal boundary resistance and diffusility for $YBa_2Cu_3O_{7-\delta}$ films. *Physical Review B*, Vol. 51, No. 17, 1995.

[155] V.N. Zhigulev and A.M. Tumin. The origin of turbulence. *Science, Novosibirsk*, 1987. *(in Russian).*

[156] A. Zibold, K. Widder, H. P. Geserich, T. Scherer, P. Marienhoff, M. Neuhaus, W. Jutzi, A. Erb, and G. Müller-Vogt. Optical anisotropy of $Y\,Ba_2\,Cu_3\,O_{7-\delta}$-films on $Nd\,Ga_3$ (001) substrates: A comparison with single domain crystals. *Appl. Phys. Lett.*, Vol. 61, pp. 345-347, 1992.